Technische Universität München

Fakultät für Physik

Physics of Energy Conversion and Storage

Identification of Active Sites for the Oxygen Reduction and Evolution under Reaction Conditions using Electrochemical Scanning Tunnelling Microscopy

Regina Michaela Kluge

Vollständiger Abdruck der von der Fakultät für Physik der Technischen Universität München zur Erlangung des akademischen Grades eines Doktors der Naturwissenschaften (Dr. rer. nat.) genehmigten Dissertation.

Vorsitzender: Prof. Dr. Martin Zacharias

Prüfer der Dissertation:

1. Prof. Dr. Aliaksandr S. Bandarenka
2. Prof. Dr. Ifan E. L. Stephens

Die Dissertation wurde am 20.07.2021 bei der Technischen Universität München eingereicht und durch die Fakultät für Physik am 14.09.2021 angenommen.

Abstract

Electrochemical energy provision and storage systems can contribute to the development of eco-friendly and worldwide-accessible energy schemes. Still, an efficiency deficit hinders their widespread commercialisation, which is fundamentally caused by the slow kinetics of the oxygen catalytic reactions: the oxygen reduction reaction (ORR) and the oxygen evolution reaction (OER). A crucial factor in advanced catalyst design is the nature of the active sites, which offer optimal binding of the involved reactive species, and are therefore responsible for most of the overall activity. In this thesis, an electrochemical scanning tunnelling microscopy (EC-STM) technique is introduced and applied, which is capable of *in-situ* identifying the active centres. The underlying principle is the analysis of a more pronounced noise level of the EC-STM signal if the scanning tip is positioned in active rather than inactive areas. The reason is the influence of an ongoing reaction on the local composition and structure of the electrolyte, which serves as the tunnelling medium. The electrodes of interest comprised state-of-the-art catalyst materials in acidic electrolytes: iridium oxide (IrO_x) for the OER and platinum (Pt) alloys for the ORR. Results indicate that the OER on amorphous IrO_x is not sensitive to the surface structure, and all surface sites of different geometries (terraces, steps, and concavities) showed similar activity. On the Pt alloys, the terraces were most active for the ORR. In contrast, spots located near the bottom of step edges showed less activity. This trend differs from the observations made on Pt(111). A brief explanation is that the binding conditions for the key reaction intermediates differ between Pt and the Pt alloy surfaces examined in this work. Since the aforementioned materials are scarce, carbon-based catalysts emerge as an abundant replacement. In this sense, a bifunctional carbon-based model system in an alkaline medium was investigated as an outlook. For both the OER and ORR, step sites and defects were most active. In total, this thesis shows the potential of the n-EC-STM technique for the *in-situ* identification of active centres with high resolution.

Zusammenfassung

Elektrochemische Energiebereitstellungs- und Speichersysteme können zur Entwicklung umweltfreundlicher und weltweit zugänglicher Energiesysteme beitragen. Bisher verhindert hauptsächlich die Ineffizienz der beteiligten katalytischen Sauerstoffreaktionen, der Sauerstoffreduktionsreaktion (ORR) und der Sauerstoffentwicklungsreaktion (OER), eine weit verbreitete Kommerzialisierung. Ein entscheidender Faktor der beteiligten Katalysatoren ist die Beschaffenheit ihrer aktiven Zentren. Diese besitzen optimale Bindungsenergien gegenüber der beteiligten reaktiven Spezies und machen daher den Großteil der Gesamtaktivität aus. In dieser Arbeit wird eine elektrochemische Rastertunnelmikroskopie (EC-STM) Technik an Modellsystemen aufgezeigt, die in der Lage ist, aktive Zentren in-situ zu identifizieren. Der Methode liegt eine Analyse des Rauschpegels des EC-STM-Signals zugrunde. Das Rauschen ist stärker ausgeprägt, falls die Abtastspitze über aktiven als über inaktiven Bereichen positioniert ist. Der Grund dafür ist der Einfluss einer elektrochemischen Reaktion auf die lokale Zusammensetzung und Struktur des Elektrolyten, der als Tunnelmedium dient. Die untersuchten Elektroden umfassten modernsten Materialien für saure Medien: Iridiumoxid (IrO_x) für die OER und Platin (Pt)-Legierungen für die ORR. Die Ergebnisse belegen, dass die OER auf amorphem IrO_x keine Sensitivität gegenüber der Oberflächenstruktur zeigt, da Oberflächenstellen unterschiedlicher Geometrien (Terrasse, Stufenkante, Konkavität) eine ähnliche Aktivität aufwiesen. Bezüglich der Pt-Legierungen für die ORR wurden die Terrassen als die aktivsten Stellen identifiziert. Im Gegensatz dazu zeigten Positionen nahe den unteren Stufenkanten tendenziell weniger Aktivität. Dieser Trend unterscheidet sich von den Beobachtungen, die an Pt(111) gemacht wurden. Als knappe Erklärung binden reines Pt und die in dieser Arbeit untersuchten Pt-Legierungen Reaktionsintermediate unterschiedlich stark. Da die untersuchten Materialien selten und damit kostspielig sind, bieten sich kohlenstoffbasierte Katalysatoren als Alternative an. Deshalb wurde als Ausblick ein bifunktionales kohlenstoffbasiertes Modellsystem in alkalischem Medium untersucht. Hierbei waren Stufenkanten und Defekte aktiv für sowohl die OER als auch die ORR. Insgesamt zeigt

diese Arbeit das Potenzial der n-EC-STM-Technik für die in-situ-Identifizierung aktiver Zentren mit hoher Auflösung.

List of Publications

S. Hou,‡ R. M. Kluge,‡ R. W. Haid,‡ E. L. Gubanova, S. A. Watzele, A. S. Bandarenka, B. Garlyyev, A review on experimental identification of active sites in model bifunctional electrocatalytic systems for oxygen reduction and evolution reactions. *ChemElectroChem*, **2021**, *8,* accepted. DOI: 10.1002/celc.202100584.

M. H. Aufa,‡ S. A. Watzele,‡ S. Hou, R.W. Haid, R. M. Kluge, A.S. Bandarenka, B. Garlyyev, Fast and accurate determination of the electroactive surface area of MnO_x. *Electrochim. Acta* **2021**, *382*, 138692.

S. Hou, W. Li, S. Watzele, R. M. Kluge, S. Xue, S. Yin, X. Jiang, A. Welle, B. Garlyyev, P. Müller-Buschbaum, A. S. Bandarenka, R. A. Fischer, Metamorphosis of heterostructured surface-mounted metal-organic frameworks yielding record oxygen evolution mass activities. *Adv. Mat.*, accepted. DOI: 10.1002/adma.202103218.

R. W. Haid,‡ R. M. Kluge,‡ T. O. Schmidt, A. S. Bandarenka, In-situ detection of active sites for carbon-based bifunctional oxygen reduction and evolution catalysis. *Electrochim. Acta* **2021**, *382*, 138285.

R. M. Kluge,‡ R. W. Haid,‡ I. E. L. Stephens, F. Calle-Vallejo, A.S. Bandarenka, Monitoring active sites for hydrogen evolution reaction at model carbon surfaces. *Phys. Chem. Chem. Phys.* **2021**, *23 (16)*, 10051.

R. M. Kluge, R. W. Haid, A.S Bandarenka, Assessment of active areas for the oxygen evolution reaction on an amorphous iridium oxide surface. *J. Catal.* **2021**, *396*, 14.

R.W. Haid,‡ R.M. Kluge,‡ Y. Liang, A.S. Bandarenka, In situ Quantification of the Local Electrocatalytic Activity via Electrochemical Scanning Tunneling Microscopy. *Small Methods* **2020**, *5*, 2000710.

T. Lochner,‡ R. M. Kluge,‡ J. Fichtner,‡ H. A. El-Sayed, B. Garlyyev, A.S. Bandarenka, Temperature Effects in Polymer Electrolyte Membrane Fuel Cells. *ChemElectroChem* **2020**, *7*, 3545.

S. Xue, R. W. Haid, R. M. Kluge, X. Ding, B. Garlyyev, J. Fichtner, S. Watzele, S. Hou, A. S. Bandarenka, Enhancing the Hydrogen Evolution Reaction Activity of Platinum Electrodes in Alkaline Media Using Nickel–Iron Clusters. *Angew. Chem. Int. Ed.* **2020**, *59 (27)*, 10934.

J. Fichtner,‡ S. Watzele,‡ B. Garlyyev, R. M. Kluge, F. Haimerl, H. A. El-Sayed, W. Li, F. M. Maillard, L. Dubau, R. Chattot, J. Michalička, J. M. Macak, W. Wang, D. Wang, T. Gigl, C. Hugenschmidt, A. S. Bandarenka, Tailoring the Oxygen Reduction Activity of Pt Nanoparticles through Surface Defects: A Simple Top-Down Approach. *ACS Catal.* **2020**, *10 (5)*, 3131.

R. M. Kluge, R. W. Haid, A. Riss, Y. Bao, K. Seufert, K. Eberle, J. V. Barth, F. Allegretti, W. Auwärter, F. Calle-Vallejo, A. S. Bandarenka, In-Situ Identification of Active Sites on $Pt_3Ni(111)$ for the Electroreduction of Oxygen, in preparation.

R. M. Kluge,‡ E. Psaltis,‡ R. W. Haid, S. Hou, T. O. Schmidt, O. Schneider, B. Garlyyev, A. S. Bandarenka, Revealing the Nature of Active Sites on Pt-Gd and Pt-Pr Alloys during the Oxygen Reduction Reaction, in preparation.

S. Hou, X. Ding, R. M. Kluge, T. K. Sarpey, R. W. Haid, B. Garlyyev, J. Warnan, W. Li, R. A. Fischer, A. S. Bandarenka, Elucidating cation effects on electrocatalytic oxygen evolution reaction activities of surface-mounted metal-organic framework derivatives, in preparation.

‡ Authors contributed equally to the publication.

Conference Contributions

Oral

R. M. Kluge, R. W. Haid, E. Psaltis, T. O. Schmidt, A. S. Bandarenka, Assessment of Active Centers on Transition Metal Surfaces for the Oxygen Reduction and Evolution Reactions, 72nd Annual ISE Meeting, Jeju Island KR/online, Aug 29-Sep 3, 2021.

R. M. Kluge, R. W. Haid, E. Psaltis, A. S. Bandarenka. *In-situ* Identification of Active Electrocatalytic Sites on Metal-Based Catalysts for Oxygen Reduction and Evolution Reaction, 10th Energy Colloquium of the Munich School of Engineering 1st Virtual Edition, online, Jul 30, 2020.

R. M. Kluge, R. W. Haid, A. S. Bandarenka. Identification of Active Electrocatalytic Sites Using Electrochemical Scanning Tunneling Microscopy, The 5th Edition of the European Graphene Forum 2019 (EGF 2019), Lisbon PT, Oct 23-25, 2019.

R. M. Kluge, Y. Liang, R. W. Haid, A. S. Bandarenka. *In-situ* Identification of Active Electrocatalytic Sites on Electrode Surfaces Using Electrochemical Scanning Tunneling Microscopy, EuropaCat 2019, Aachen DE, Aug 18-23, 2019.

R. M. Kluge, R. W. Haid, Y. Liang, D. McLaughlin, C. Csoklich, J. H. K. Pfisterer, O. Schneider, A. S. Bandarenka. Identification of Active Electrocatalytic Sites Using Electrochemical Scanning Tunneling Microscopy, XXXIX. Modern Electrochemical Methods, Jetrichovice CZ, May 20-24, 2019.

Poster

R. M. Kluge, R. W. Haid, T. O. Schmidt, A. S. Bandarenka, Assessment of Active Centers on Transition Metal Surfaces for the Oxygen Reduction and Evolution Reactions, SUNCAT Summer Institute 2021, online, Aug 16-18, 2021.

R. M. Kluge, R. W. Haid, T. O. Schmidt, A. S. Bandarenka, Assessment of Active Centers on Transition Metal Surfaces for the Oxygen Reduction and Evolution Reactions, 11th Energy Colloquium of the Munich School of Engineering 2st Virtual Edition, online, Jul 28-29, 2021.

R. M. Kluge, R.W. Haid, E. Psaltis, A.S. Bandarenka. In-Situ Identification of Active Electrocatalytic Sites on Metal-Based Catalysts for Oxygen Reduction and Evolution Reaction, 71st Annual ISE Meeting, online, Aug 30-Sep 4, 2020.

R. M. Kluge, R. W. Haid, A. S. Bandarenka, Identification of Active Electrocatalytic Sites Using Electrochemical Scanning Tunneling Microscopy, 708. WE-Heraeus Seminar on Operando Surface Science / Atomistic Insights into Electrified Solid/Liquid Interfaces, Bad Honnef DE, Dec 9-13, 2019.

R. M. Kluge, R. W. Haid, A. S. Bandarenka, Identification of Active Electrocatalytic Sites Using Electrochemical Scanning Tunneling Microscopy, ECS Student Chapter Munich 3rd Symposium, Garching DE, Sep 24, 2019.

R. M. Kluge, R. W. Haid, Y. Liang, A. S. Bandarenka, Identification of Active Electrocatalytic Sites Using Electrochemical Scanning Tunneling Microscopy, 9th Energy Colloquium of the Munich School of Engineering, Garching DE, Aug 01, 2019.

Contents

1 Motivation and Scope

Paris, December 12, 2015: 196 countries adopt a legally binding agreement to keep global warming well below 2 °C compared to pre-industrial levels. Further efforts are to be pursued to limit the temperature increment to 1.5 °C.[1] Projections indicate that reducing global warming to below 1.5 °C requires 80% zero-emission energy by 2030 and 100% by 2050.[2] Otherwise, in a business-as-usual manner, the average global temperature increase leads to rising sea levels, extreme weather and climate conditions, and a negative impact on the biological, social, and economic systems.[3]

To turn the tide, a transition toward a clean, low emission energy system is necessary. However, an additional complication is the growing global energy demand, which is predicted to double by 2050.[4] Meanwhile, the supply of fossil fuels is declining with scarcity in oil and gas, which is anticipated to occur in the near future.[5, 6] While the requirement for energy is rising rapidly around the globe, oil and gas reserves are located in distinct regions, which poses the risk of international conflicts between hydrocarbon exporters and countries that rely on the supply.[7] As an alternative, two particular energy carriers show great promise for the decarbonisation of the energy sector: electricity and hydrogen. Zero-emission electricity can be provided from renewable sources such as wind, water, and sunlight.[2] Hydrogen is the most abundant element in the universe. However, it does not occur as a natural fuel on Earth.[8]

There are three essential aspects connected to hydrogen in the energy transition: production, storage, and use. A possible large-scale scenario for a power system based on H_2 is shown in **Figure 1**.[9] As hydrogen only occurs as an energy carrier in the form of chemical compounds such as hydrocarbons or water, chemical transformation to H_2 is necessary. At present, the largest segment of hydrogen is produced from natural gas by steam reforming, which avoids neither the need for fossil fuels nor CO_2 emission.[8] Instead, in electrolysis, hydrogen can be produced from renewable electricity and water without any emissions. In contrast to fossil fuels, water is abundantly distributed around the world, providing a more uniform access to hydrogen as a fuel.[8] After its production, hydrogen can be stored and transported at high energy density

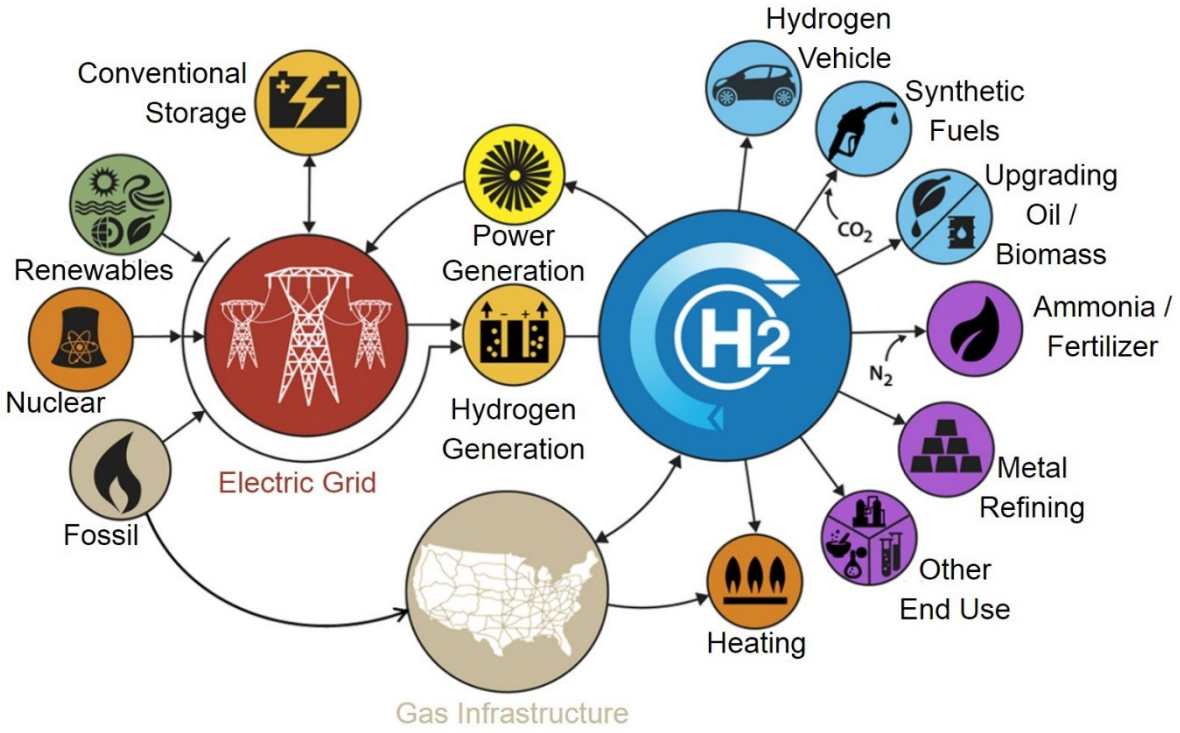

Figure 1 | Sketch of a concept for hydrogen production and usage. In a low-carbon economy, hydrogen can be generated *via* electrolysis from a renewable power source. Up to date, the primary use of hydrogen is in the oil refining and ammonia industries. Other emerging applications include fuel cell vehicles, metal refining, and synthetic natural gas production. Adapted from reference [9].

in liquid or gaseous form. For a secured supply, functioning cross-border hydrogen infrastructures are essential. A major attraction of the hydrogen concept holds its application in the transport sector, for industrial purposes, and heating. Hydrogen can be directly combusted or fed to fuel cells to generate heat and electricity.[8]

Today, a very popular topic is the use of electricity and hydrogen to decarbonise transport. Research and public interest focus on zero-emission technologies such as hydrogen-powered fuel cell electric vehicles (FCEV), battery electric vehicles (BEV), and hybrid approaches. Car companies such as Toyota,[10] Hyundai,[11] Honda,[12] Daimler[13] and BMW[14] have set their minds to the development of FCEVs. From the year 2021, two car models, the Toyota

Mirai[10, 15] and the Hyundai Nexo[11], are commercially available and able to outperform state-of-the-art BEVs (*e.g.* the Tesla Model X[16]) in terms of re-fuelling time and distance. Car companies state that long distances (more than 600 km[10, 11]) can be overcome without the need to re-fuel. In turn, the re-fuelling process itself is relatively fast (3 to 5 min[11]), which is similar to current gasoline or diesel cars. However, a major obstacle is the lack of an H_2 gas station network, which is needed especially for long-distance travel. On the merits, the installation of such a network could adopt and thus benefit from the already existing gasoline infrastructure.[3] Beyond the automotive industry, hydrogen offers undefeatable chances for purposes where direct electrification is not feasible: heavy-duty transport, non-electrified trains, overseas transport, and aviation. Only recenty, in December 2020, a collaboration between the University of Ulm and the German Aerospace Center (DLR) succeeded in the take-off of the world's first four-seater hydrogen fuel cell aircraft.[17] On a larger scale, Airbus conceptualises the world's first zero-emission commercial aircraft by 2035. The hybrid-hydrogen aircraft should be powered by hydrogen combustion through modified gas turbine engines and hydrogen fuel cells.[18]

In summary, a great potential of hydrogen as an energy carrier lies in its production from renewable energies in water electrolysers and its use in zero-emission hydrogen fuel cells. Still, a deficit in efficiency hinders the widespread commercialisation of these technologies. A fuel cell, running with hydrogen produced from electrolysis (*ca.* 60-90% efficiency), reaches an overall efficiency of only 35-40%. This is substantially lower than in the case of Li-ion batteries, which achieve electricity-input to -output efficiencies of up to 80%.[19] A primary limit arises from the losses of the individual reactions of the water cycle, especially from the oxygen reactions. In a proton-exchange membrane fuel cell (PEMFC), besides the issue of the cost and stability of the membrane, the major complication is the large overpotential required for the oxygen reduction reaction (ORR) at the cathode. Similarly, the inverse reaction, the oxygen evolution reaction (OER) at the anode of electrolysers, suffers from slow reaction kinetics. The sluggishness of both ORR and OER arises from complex reaction mechanisms involving multiple electron-proton transfer steps and reaction intermediates. To date, state-of-the-art catalysts are based on ruthenium and iridium oxide for the OER and platinum for the

ORR.[20] These metals are scarce, and thus their use should be optimised to reduce cost. In the presently available commercial PEMFC technology, 800 tonnes of platinum would be necessary for a peak capacity of 1 TW, which would be the prerequisite to playing a role in energy conversion.[21] Thus, the expansion of renewable hydrogen technologies requires interdisciplinary, atomic- or molecular-level insights in oxygen electrocatalysis to design advanced and economically viable electrocatalytic materials.

A strategy for catalyst optimisation is to disperse the often-precious materials into nanoparticles for an optimised surface-to-volume ratio. With modern synthesising techniques it is possible to manufacture nano-single crystals which expose well-defined crystal facets.[22-24] Since both the ORR and OER are sensitive to the nanoscale- and atomic-level structure of the heterogeneous interface at which they take place, the activity can depend on facets, sites and edges.[25, 26] Therefore, the overall performance of such a catalyst can be traced back to so-called active sites, which offer optimal binding conditions to reaction intermediates.[25, 27-30] A rational way of designing catalysts should thus first identify the optimal active sites and then engineer surfaces with a maximum density of such sites.[31] Model single crystal surfaces and ultra-high vacuum (UHV) techniques paved the way for experimental studies on the electronics and structure of catalytic centres. Advances in theoretical chemistry, such as density functional theory (DFT), evolved as a valuable complement to provide insights into heterogeneous catalysis.[32] The nature of the active sites can depend on the material composition, the surface structure, and the electrolyte.[30]

To contribute a piece to solving the puzzle, in this work, an *in-situ* method to identify active sites on model catalyst surfaces is presented. The technique, which is based on electrochemical scanning tunnelling microscopy (EC-STM), can detect local activity levels by spatially confined noise in the EC-STM signal. The electrode surfaces of interest consisted of state-of-the-art materials: iridium oxide for the OER, as well as $Pt_3Ni(111)$ and polycrystalline Pt-lanthanide alloys for the ORR. As those materials are scarce, carbon-based materials appear as an abundant replacement. Therefore, a bifunctional carbon-based model system was investigated as an outlook. In all the studies, noise analysis in EC-STM (n-EC-STM) succeeded

in detecting the geometry of the active sites, and the findings were supported by calculations and/or literature reports. These insights are vital in rational catalyst design, and there is a need for suitable surface-sensitive techniques providing access to the active sites.

2 Introduction to Electrocatalysis

A catalyst is a substance capable of improving reaction kinetics without appearing in the product and can thus act repeatedly. In heterogeneous catalysis, the catalyst is in a different phase than the reactants. As an example, a reaction between two fluid species (*i.e.* both either in the liquid or gaseous phase), *A* and *B*, in the presence of a solid catalyst is considered. Its characteristics, without and with the catalyst, are sketched in the potential energy diagram provided in **Figure 2**.[20] Even if the overall reaction from reactants to product is exothermic, an activation barrier of $\Delta G^{\ddagger}$ has to be overcome. By contrast, the use of a catalyst reduces the activation energy. Additionally, the reaction pathway can alter, and the formation of "new" intermediates yields additional minima in the potential energy diagram. **Figure 2** presents an example in which the reaction proceeds as follows: In the first step, species *A* adsorbs on the solid catalyst surface (first intermediate). In the second step, the reaction partner *B* reacts with the adsorbed species *A* (second intermediate). In the last step, the product *A–B* desorbs from the surface.[20, 33, 34] Note that the energy levels of the reactants and the product remain unaltered by the catalyst. In other words, a catalyst influences the reaction kinetics without affecting the thermodynamics.[33, 35, 36] Ideally, a catalyst should not rearrange its structure and composition comparing the state before and after the reaction. In reality, however, catalysts can change their shapes or agglomerate during the reaction, which can diminish their catalytic abilities. Therefore, a catalyst needs to possess adequate stability aside from activity and selectivity.[37]

Fundamental concepts of electrocatalysis, which fall within the scope of this thesis, are recapitulated in the following sections. Electrocatalysts are heterogeneous catalysts, which accelerate the rate of electrochemical processes. Electrochemistry, in turn, is concerned with the interconversion of electrical and chemical energy. Hereby, charge transfer is promoted across an electrified solid-liquid interface.[38]

The first part (Chapter 2.1) covers electrochemical reactions and all aspects, which play a role in their application. In the first paragraph (Chapter 2.1.1), devices capable of converting

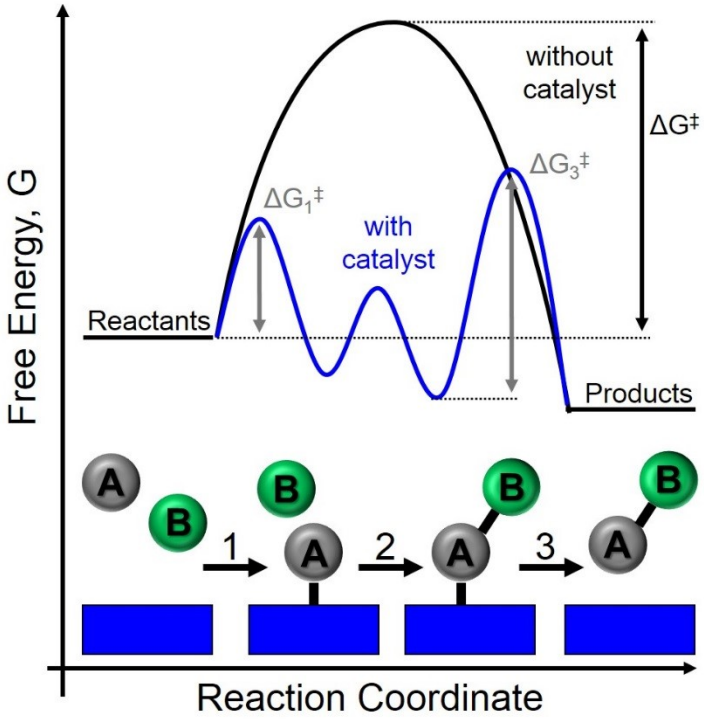

Figure 2 | The potential energy diagram of a reaction between two species *A* and *B*. If no catalyst is used (black curve), a higher energy barrier has to be overcome to drive the reaction. A catalyst (blue line) lowers not only the activation energy but can also change the reaction pathway. In this example, two reaction intermediates are involved and are associated with the minima in the curve. Below, a possible reaction pathway is given. The reaction can take place upon adsorption of one of the reactants (*e.g.* of species *A*). The second reactant (species *B*) reacts with the adsorbed species and forms an adsorbed product (second intermediate). In the last step, the product desorbs from the catalyst surface. Image is adapted from reference [20] with permission from The Royal Society of Chemistry.

electrical into chemical energy and back are introduced as well as losses in the process. Subsequently, Chapter 2.1.2 deals with the electrified solid-liquid interface. A set-up consisting of three electrodes immersed in an electrolyte can assess changes at said interface experimentally (Chapter 2.1.3). Finally, Chapter 2.1.4 is dedicated to the quantification of the

electrocatalytic performance of catalyst materials. The second part (Chapter 2.2) clarifies that the reaction does not necessarily take place uniformly across the surface but at a higher rate at active sites, which offer optimal binding conditions. Chapter 2.2.1 addresses types of adsorption for reactants on the catalyst surface. For surface-sensitive reactions, as discussed in Chapter 2.2.2, adsorption energies vary with the location at the surface. The knowledge of the nature of active centres is inevitable to engineer materials with a maximal active site density, which is referred to in Chapter 2.2.3.

2.1 Electrochemical Reactions at an Electrified Solid-Liquid Interface

Electrochemical conversion and storage devices can assist in environmentally friendly energy provision schemes. If using hydrogen as fuel, PEMFCs and proton-exchange membrane (PEM) water electrolysers are of particular interest. In such a type of electrochemical cell, two spatially separated redox reactions occur. The electrons transferred during the reactions flow through an outer circuit, which enables the conversion of chemical into electrical energy or *vice versa*. Losses in the process decrease the maximum electrical energy (voltage) that can be obtained or needs to be applied in such a device. The efficiency of the device and the voltage are thus related. The current is a measure of the reaction rate, since electrons, generated or consumed during the reactions, move through the outer circuit. Hence, voltage and current are of utmost importance.[39]

In the following, the first subchapter is dedicated to the fundamentals of hydrogen fuel cells and water electrolysers and their efficiency. Since it is more convenient to examine only one electrode material at a time, it is common to investigate only one half-cell reaction taking place at the interface between an electrode and the electrolyte. To access the electrode potential, a set-up consisting of three electrodes is necessary. Finally, the last subchapter deals with measures to quantify the catalytic performance.

2.1.1 Cell Potential and Overpotentials

Hydrogen fuel cells and water electrolysers are capable of transforming chemical into electrical energy and *vice versa*. In such a device, two redox (half) reactions are separated spatially. The overall reaction balances stoichiometrically, which means the same number of electrons n is exchanged during each of the two half-reactions. Electrons flow through an outer circuit, whereas a membrane conducts the ions. In PEMFCs or electrolysers, the latter are protons or, more precisely, in the form of H_3O^+ in a humidified system.

At first, the case of the fuel cell is considered. Here, the Gibbs free energy of the reaction converts into the electric work. If losses are at first neglected, a fundamental relationship between the molar free energy of reaction $\Delta_r G$ and the potential difference between the electrodes at open circuit E_0 states:

$$\Delta_r G = - nFE_0 \qquad \textbf{Eq. 1}$$

where n is the number of electrons exchanged in a single event of the half-reactions and F is the Faraday constant. E_0 corresponds to the maximum cell voltage of the overall cell reaction without accounting for losses. The zero indicates an equilibrium potential, which in general depends on the concentration of species involved in the reaction, the temperature and the standard electrode potential, and is described by the Nernst equation.[40]

The overall fuel cell voltage is determined by the potentials of the anode and cathode reactions[41]

$$E_{cell} = E_{cathode} - E_{anode}. \qquad \textbf{Eq. 2}$$

In the thermodynamic equilibrium, **Eq. 1** holds for both half-reactions. However, in practice, the power output is lower due to losses. The potential difference between the thermodynamic E_0 and the actual output voltage E is termed overpotential η.

$$\eta = E_0 - E. \qquad \textbf{Eq. 3}$$

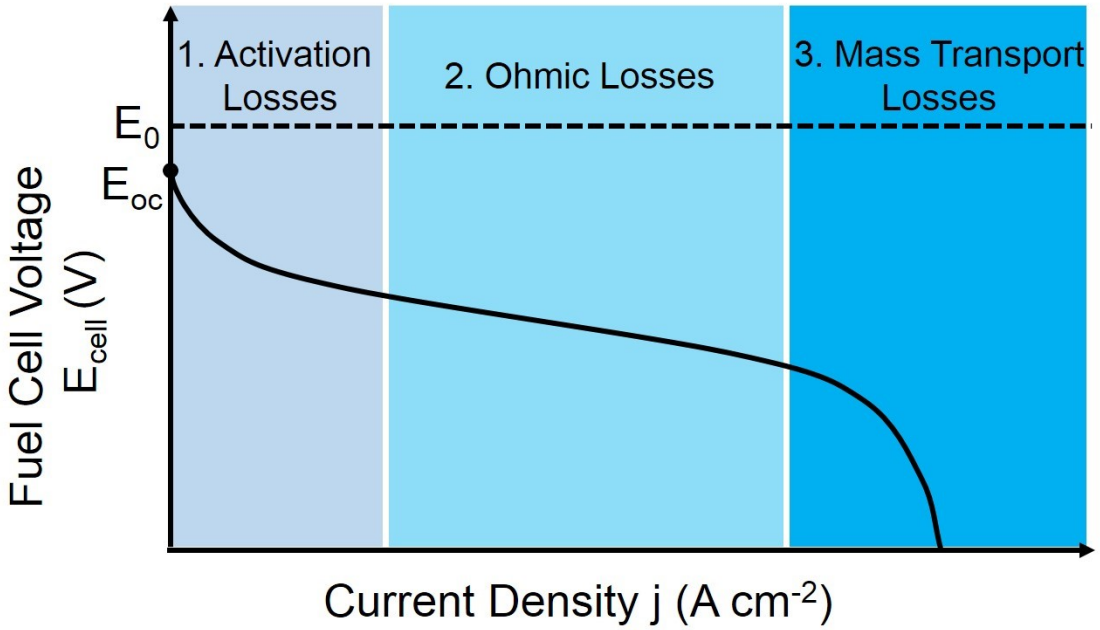

Figure 3 | A schematic of a fuel cell polarization curve. In contrast to the ideal thermodynamically predicted voltage of a fuel cell (E_0), the voltage of a "real" fuel cell is lower (solid line). The losses are assigned to the current region in which they are the most dominant. The open circuit voltage (E_{oc}) at zero current may be diminished compared to the thermodynamic optimum due to fuel crossover and internal electric currents. 1. Activation losses occur due to sluggish kinetics of the involved electrochemical reactions. 2. Non-ideal transport of ions dominates Ohmic losses between the electrodes through the electrolyte. 3. A finite supply of reactants governs mass transport losses at both electrodes.

Figure 3 gives a typical current-voltage curve of a fuel cell. With increasing current drawn from the fuel cell, the voltage drops. At zero current, the open circuit voltage (E_{oc}) can be lower than the thermodynamically reversible one because of fuel crossover and internal electronic currents. Fuel crossover denotes the passage of fuel through the membrane and subsequent undesired parasitic reactions. In addition, electron conduction through the membrane would lead to a reduced open circuit voltage. These losses become less prominent at non-zero current densities. At higher current densities, additional factors are dominating and are listed in the following.[39, 42]

1. **Activation losses**. At both electrodes, electrochemical reactions convert chemical into electrical energy. Sluggish reactions possess low rates and thus lead to small currents. Therefore, catalysts improve the reaction kinetics and minimise activation losses. Catalytic activity is discussed in more detail in Chapter 2.1.4.

2. **Ohmic losses**. Each half-reaction involves the transfer of electrons and ions. The number of electrons and ions consumed at one electrode are to be produced at the opposed electrode. Thus, the transport of ions in the electrolyte and electrons in the external circuit is to be established. Electronic transport can be maintained by an electrical connection such as a wire between both electrodes, and the corresponding losses are commonly negligible. By contrast, ion conduction typically proceeds *via* a hopping mechanism, which is less efficient than the transport of electrons driven by an electric field. To reduce Ohmic losses, electrolytes of high ionic conductivity are required. Moreover, Ohmic losses can be mitigated by a decreased membrane thickness, which, however, eases fuel crossover. In PEMFCs, a state-of-the-art material is the sulfonated tetrafluoroethylene-based fluoropolymer-copolymer Nafion®.

3. **Mass transport losses**. Continual reactions require the supply of reactants to the electrode surfaces and the removal of the products to prevent blocking of the electrode surface. This becomes more challenging at increasing current densities, which are equivalent to higher reaction rates. In practice, flow field plates combined with porous electrode structures account for these issues.

All considerations hold analogously for electrolysers, except for the signs of each equation. E_0 is the minimum potential required to run the electrolyser, and thus the sign in **Eq. 1** is positive. The overall cell voltage E_{el} still depends on the half-cell potentials according to

$$E_{el} = E_{anode} - E_{cathode}. \qquad \textbf{Eq. 4}$$

Losses, which can be of the same origins as in fuel cells, increase the overall potential needed to drive the water-splitting reactions.[43]

2.1.2 The Electrified Solid-Liquid Interface

For research purposes, it is more convenient to examine an individual catalytic material instead of the whole electrochemical cell. Therefore, consider the interface between a single electrode and a liquid electrolyte. In general, the potentials of the bulk electrode and the bulk solution are different. The electrode of interest, termed working electrode (WE), can be charged due to an ongoing reaction if being immersed into the solution and/or under an external potential.[40]

Without loss of generality, assume a negatively charged metal electrode surface. By electrostatic interaction, solvated cations accumulate at the metal surface. The centres of these ions constitute the outer Helmholtz plane (OHP). This type of double layer can be modelled as a plate capacitor, with one plate being the electrode surface, the other one the OHP. Since the distance between the plates is the radius of the solvation shell, the capacitance is large, which is harvested in supercapacitors.[44] Due to thermal motion, the solvated cations are less ordered toward the bulk of the electrolyte. Still, an excess of ions with an opposite charge to the electrode is present in the so-called diffusion layer. A more sophisticated model of the double layer considers that ions can also adsorb on the electrode surface. Because of the characteristics of their van der Waals interactions, anions tend to undergo specific adsorption, irrespective of the charge of the electrode. These adsorbed ions establish a second layer, the inner Helmholtz plane (IHP). The final picture of the electrified double layer is given in **Figure 4**a.[40]

2.1.3 Three-Electrode Configuration

Direct measurement of the Galvani potential difference between electrode and electrolyte is not feasible.[40] Instead, a common way to access the processes taking place at the electrode-electrolyte interface experimentally is the use of a three-electrode set-up.

In general, the potential of the WE can only be given with respect to a reference electrode (RE). The Galvani potential of such an RE is defined as zero. As an example, the standard hydrogen electrode (SHE) is a platinum (Pt) sheet immersed in an aqueous solution containing H^+ ions of unit activity and is exposed to hydrogen (H_2) gas under standard conditions, T = 298.15 K,

pH = 0, $p_{H2(g)}$ = 1 atm. The equilibrium potential of the reaction in **Eq. 5** defines a potential of zero, *i.e.*, $E_0 \equiv 0\ V_{SHE}$.[40, 45]

$$2\ H^+(aq) + 2\ e^- \rightleftharpoons H_2 \qquad \textbf{Eq. 5}$$

In this thesis, the index in the unit indicates the type of RE to which the potential value is referred.

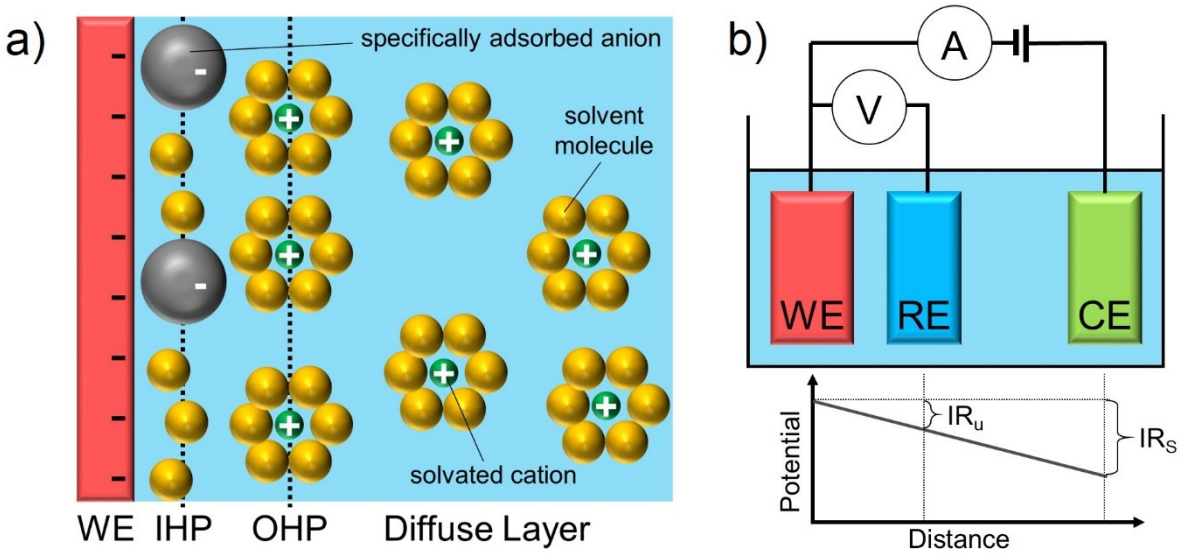

Figure 4 | a) A sketch of the electric double layer at a negatively charged electrode. Solvated cations accumulate at the electrode surface and build up the OHP. In addition, ions can adsorb on the electrode surface and thereby form the IHP. Further to the bulk electrolyte, less-ordered solvated cations constitute a diffuse layer due to thermal motion. b) The three-electrode configuration. The potential of the WE is measured with respect to the RE. Current flows between WE and CE, whereas no current runs through the RE. Below, the potential drop because of the electrolyte resistance (R_S) is sketched. If passing a current I between WE and CE, the resistance of the electrolyte changes the potential measured at a certain position. This effect can be diminished by placing the RE close to the WE. However, an uncompensated resistance (R_U) is unavoidable.

During an electrochemical experiment, current passes through the system. A two-electrode system, comprised of WE and RE, only provides reliable results if the current does not alter the potential of the RE. Therefore, the RE needs to be non-polarisable, of large area and possess high activities of the redox forms. Otherwise, an additional overpotential at the RE is required and leads to a change in applied potential.[46] To circumvent the demanding requirements of a two-electrode cell, a three-electrode set-up is conventionally used. As shown in **Figure 4**b, besides the WE and RE, a third electrode is implemented, which is termed counter electrode (CE). The current is then passed between WE and CE, whereas no current flows through the RE. The WE potential is referred to the RE. The CE can be any conductive, chemically inert material.

Still, one has to account for the finite resistance (R_S) of the electrolyte. If passing a current I, the potential deviates by IR_S. To reduce that potential change, the three electrodes are arranged as depicted in **Figure 4**b; the RE is located in close vicinity to the WE, whereas the CE is positioned on the same side of the WE but further apart. As sketched in the potential curve below, this reduces the influence of the solution resistance on the potential at the position of the RE compared to the CE. The closer the RE is to the WE, the smaller the voltage drop will be. Fine tips called Luggin capillaries are designed to place the RE close to the WE.[45, 47, 48] Nonetheless, some fraction of IR_S is unavoidably included, which is denoted as uncompensated resistance (R_U). The uncompensated resistance can be corrected by an additional measurement such as impedance spectroscopy.[49]

2.1.4 Assessment of the Catalytic Performance

In describing the kinetics of electrochemical reactions, it is crucial to relate current density to potential changes and *vice versa*. For the following mathematical treatment of that problem, a one-step, one-electron transfer is assumed. Moreover, mass transport is neglected, which signifies that the reactant concentration near the electrode surface does not differ from the bulk solution. The resistance of the electrolyte is also not taken into account. In such a case, the net current density j produced in a reaction driven by an activation overpotential η_{act} is given as

$$j = j_0 \left(\exp\left(\frac{\alpha F \eta_{act}}{RT} \right) - \exp\left(-\frac{(1-\alpha) F \eta_{act}}{RT} \right) \right) \qquad \textbf{Eq. 6}$$

where R and F are the universal gas constant and the Faraday constant, T is the temperature, j_0 is the exchange current density and α is the transfer coefficient.[48] **Eq. 6** is known as the Butler-Volmer equation. For the derivation, please see references [39, 40, 45, 48]. The following paragraph is instead dedicated to explaining the different constituents.

Importantly, j is a net current density. If addressing the rate of a reaction, both forward and backward reactions occur at the same time. The currents of the forward (FW) and backward (BW) reactions thus give rise to the net current density:

$$j = j_{FW} - j_{BW}. \qquad \textbf{Eq. 7}$$

In equilibrium ($\eta_{act} = 0$), the forward and backward reactions are balanced, and therefore the respective current densities are equal to the so-called exchange current density j_0:

$$j_0 \equiv j_{FW} = j_{BW}. \qquad \textbf{Eq. 8}$$

The exchange current density depends on the activation barrier of the forward reaction E_a and the concentration of the reactants c^* in an Arrhenius trend, *i.e.*, $j_0 \propto c^* \exp\left(-\frac{E_a}{RT}\right)$. It can serve as a measure for catalytic activity. The larger j_0, the more current can be drawn out of a reaction at a certain potential, and in turn, the faster the reaction kinetics.[45]

Applying an overpotential allows to bias the system such that either the forward or backward reaction is favoured, which is described by the transfer coefficient α. The change in the energy barrier of the forward reaction is proportional to α, whereas the energy barrier change of the backward reaction scales with $(1 - \alpha)$. In an ideal symmetric case, $\alpha = 0.5$. For most electrochemical reactions, α takes a value between 0.3 and 0.7.[48]

The overpotential required for a particular current density value can describe the catalytic performance. As introduced in Chapter 2.2.1, in general, the overpotential is the potential difference between the experimentally applied potential and the thermodynamic potential, and

thus relates to losses. The activation overpotential must be de-coupled from Ohmic and mass transport losses in order to link the overpotential to the catalytic activity. The former can be done by IR_U compensation (see Chapter 2.1.3), the latter by evaluating the catalyst performance at low reaction rates. As an example, hydrogen evolution reaction (HER) and OER catalysts are typically compared at a current density of 10 mA cm^{-2}.[50] For the ORR, the activity is commonly measured at a potential of 0.9 V_{RHE} (RHE stands for reversible hydrogen electrode).[51] In addition, the WE can be rotated to enable a steady flow of reactants to the electrode, allowing for a well-defined mass transport (*cf.* Chapter 4.1).[52]

Consider the overpotential to be large; or more fundamental if $j \gg j_0$. Large overpotential often means η_{act} larger than 50-100 mV at room temperature. In this case, the second term in the Butler-Volmer equation can be neglected. This implies the first term, the forward reaction, dominates, and the overall reaction can be seen as irreversible. The overpotential can be written in the form of

$$\eta_{act} = a + b \log j. \qquad \textbf{Eq. 9}$$

This equation is known as the Tafel equation, and *b* is referred to as the Tafel slope. It can be used as a descriptor of the catalytic activity and can also assist in predicting the reaction mechanism.[39]

Besides current density, exchange current density, overpotential and Tafel slope, another measure for catalytic activity is the turnover frequency (TOF). It is defined as the number of reaction events per active site and per time unit for a fixed set of reaction conditions (temperature, pressure, reactant concentration).[53]

$$\mathrm{TOF} = \frac{dN_e}{dt} \cdot \frac{1}{N_a} \qquad \textbf{Eq. 10}$$

In **Eq. 10**, N_e denotes the number of reaction events, N_a is the number of active sites, and *t* is time.

During a single reaction event, a fixed number of electrons *n* is transferred. Since the sample current *I* measures charge *Q* per time, it accounts for the number of reaction events per time. Dividing the current by the number of electron transfers per event and the elementary charge *e* is equal to the number of reaction events per time.

$$|\,I\,| = \frac{dQ}{dt} = \frac{dN_e}{dt} \cdot e \cdot n \qquad \textbf{Eq. 11}$$

Combination of **Eq. 10** and **Eq. 11** yields[54]

$$TOF = \frac{|\,I\,|}{ne\,N_a}. \qquad \textbf{Eq. 12}$$

For a monometallic surface in a well-defined atomic arrangement, one can equate the number of active sites on the surface with the total number of atoms on the surface. In the case of a crystal surface in a face-centred cubic (*fcc*)-(111) orientation, the number of surface atoms can be expressed as the fraction of sample surface area A_S and the area of the unit cell, according to

$$N_a = \frac{A_S}{d^2 \sin\alpha} \qquad \textbf{Eq. 13}$$

where *d* is the shortest atom-to-atom distance and the angle $\alpha = 60°$ for an *fcc* arrangement. Inserting this expression in **Eq. 12** yields

$$TOF = \frac{|\,j\,|\,d^2 \sin\alpha}{ne} \qquad \textbf{Eq. 14}$$

with the geometric current density *j*.

2.2 Structural Effects in Electrocatalysis

The electrocatalytic reactions introduced in the last chapter do not necessarily take place uniformly across the catalyst surface. Noteworthy, for structure-sensitive reactions, dissimilar surface sites show different reaction kinetics. These local differences in the activity stem from diverging adsorption properties of the structural motifs with respect to the reaction intermediates. To achieve the maximum activity, the binding needs to be balanced. While a too weak binding is insufficient for activation, a too strong binding poses the danger of catalyst poisoning.[55] Therefore, sites of ideal binding govern the overall activity. These active centres can arise, for example, from the geometric arrangement of the surface atoms or the composition of the catalyst.[56] The knowledge of their nature is vital for rational catalyst design, as a maximal number of active sites exposed on the surface is required for optimal performance.

This chapter highlights the origin of structure-sensitive reactions. Section 2.2.1 gives principles of reactant adsorption on the catalyst surface. Section 2.2.2 explains the meaning of optimal binding, formulated as the Sabatier principle, and its role in predicting catalytic performances. Section 2.2.3 elucidates the importance of active sites, their properties, and a means for their identification.

2.2.1 Physisorption, Chemisorption, and Dissociation

A heterogeneous reaction between two reactants can proceed in two different pathways. In the first way, each of the reactants adsorbs on the surface. In the next step, they migrate towards each other and react to form the product, which subsequently desorbs (Langmuir-Hinshelwood mechanism). In the second way, only one of the reactants adsorbs on the surface. Afterwards, the reaction partner from the fluid (gas or liquid) phase reacts directly with the adsorbed species (Eley-Rideal mechanism). Finally, the product desorbs from the surface.[33] Both mechanisms are possible and discussed in Chapter 3 for the reactions of interest in this thesis.

The surface interactions between adsorbate and catalyst surface hold the key to catalyst activity, selectivity, and stability.[37] If a reactant comes close to the catalyst surface, it interacts with the

potential energy built up by the constituent metal atoms. At medium distances of a few angstroms, the reactant can induce dipole-dipole interactions (van der Waals forces) with the surface, which can lead to physisorption. If approaching the surface further, chemical bonds can be established between the reactant and the catalyst (chemisorption). Thereby, molecules can be chemisorbed as a whole. Stronger interactions with the surface eventually lead to the dissociation of molecules and subsequent adsorption of single atoms. The latter is subject to the following paragraph.[34]

In the following, the changes in the electronic properties of a diatomic molecule approaching the surface of a transition metal are considered to understand qualitatively why transition metals are an attractive class of catalysts. For more details and a quantum-mechanical view of molecular orbitals and band structure, see references [57, 58].

At first, the focus is set on the electronic structure of a diatomic molecule such as *e.g.* hydrogen. If two atoms approach each other, the two corresponding electronic wave functions start to overlap. Thus, the molecule possesses two "new" electronic wave functions obtained from linear combinations of the two atomic orbitals. The energies of the molecule split into a bonding and an antibonding level. This is sketched on the right side of **Figure 5**, where exemplarily two atomic s-orbitals split into a bonding (σ) and antibonding (σ*) molecular orbital. The higher the overlap between the two atoms, the greater is the energy difference of the molecular orbitals. The stability of the bond can be estimated *via* the occupancy of the energy levels. If only the bonding level is filled with electrons, the molecule is stable. If both bonding and antibonding levels are filled, the bond between the atoms is weak, and the dissociation of the molecule is easy.

Second, the band structure of a solid, comprised of one type of atom, is considered. Analogue to the diatomic molecule, the atomic orbitals of adjacent atoms overlap. The electron wave functions of the crystal are combinations of the wave functions of the constituent atoms. Since the number of atoms in a solid is much higher than in a single molecule, the energy levels of the crystal lie close to each other in terms of energy. Therefore, they can be considered as energy bands, and their width is given by the extent of the overlap between neighbouring atomic

orbitals. The shapes of the energy bands in the solid depend on the properties of the single atomic orbitals. If the atomic orbital possesses a pronounced shape and orientation, the overlap to a neighbouring orbital of the same type is small. In a crystal, this results in the formation of a narrow band. Here, many states are located in a small energy interval, which is equivalent to

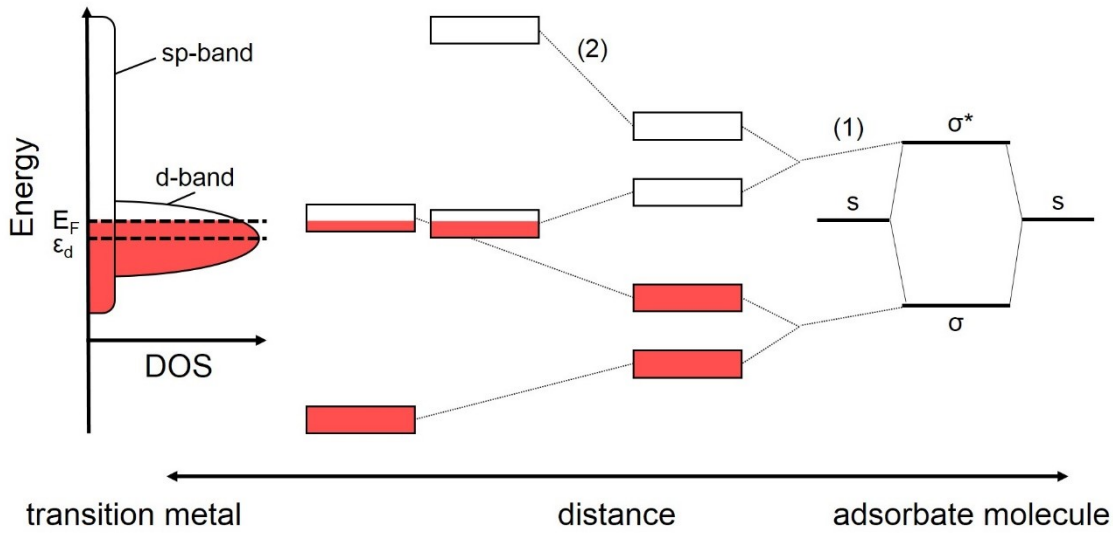

Figure 5 | A schematic of the interaction between a diatomic molecule (right) and a transition metal surface (left). Occupied states are coloured in red, unoccupied in white. The states of the transition metal are filled up to the Fermi level (E_F). (1) The energy levels of the adsorbate are modified upon the interaction with both the sp- and d-bands of the transition metal. The former leads to a broadening of the molecular orbitals (σ, σ*) and a downshift in energy, which implies a stabilisation of the adsorbate on the metal surface. In addition, the strong interplay with the transition metal d-band induces a splitting of the molecular orbitals. (2) At closer distances, both effects combine and result in a partial filling of the former antibonding molecular orbital. In consequence, the bond between adsorbate and surface strengthens, whereas the intramolecular bond of the adsorbed molecule destabilises. Therefore, a transition metal surface can dissociate a diatomic molecule, such as H_2 or O_2. Reproduced with permission from reference [34].

a high density of states (DOS). *Vice versa*, a significant overlap between atomic orbitals results in a wide band and a small DOS. In transition metals, both types of orbitals exist. Tightly bound d-electrons overlap little with the d-orbitals of adjacent atoms and yield narrow d-bands. The outer s- or p-electrons experience less interaction with the atomic core, which allows large overlap. Therefore, a wide sp-band establishes. On the left side of **Figure 5**, the corresponding DOS of a transition metal is sketched. Herein, the bands are filled with valence electrons up to the Fermi level (E_F).

After the discussion of the energetic properties of a crystal and a diatomic molecule, the focus is now on the diatomic molecule approaching the surface of a transition metal. In such a situation, the two molecular orbitals (σ and σ*) interact with the broad sp-band and the narrow d-band of the transition metal. The first yields broader molecular orbitals, which are downshifted in energy. Thereupon, the adsorbate stabilises on the metal surface. The second interaction type with the d-bands is stronger and able to split the adsorbate levels into pairs of bonding and antibonding orbitals. At closer distances between adsorbate and metal, the combination of both effects eventually results in a partial filling of the former antibonding molecular orbital, as illustrated in **Figure 5**. Consequently, the bond between adsorbate and surface is strengthened, whereas the intramolecular bond of the adsorbed molecule is destabilised. This is the key to understand the reason for molecular dissociation at a transition metal surface.[34]

2.2.2 Sabatier Principle and Volcano Plot

The previous discussion about interaction types between adsorbates and the catalyst surface sets the stage for understanding catalyst optimisation. To improve reaction kinetics, the binding strength between adsorbate and catalyst should balance. Sufficiently strong adsorption is necessary to dissociate bonds and form reaction intermediates. By contrast, if the adsorption is too strong, the reaction intermediates cannot leave the surface, which leads to a blocking of the catalyst surface.[34, 35] This rule was first stated by Sabatier in 1911 as a purely qualitative trend.[55, 59, 60] An empirical concept closely related to the Sabatier principle is the volcano curve, which is obtained from plotting the activity of a catalyst *versus* the catalyst's ability to

form chemical bonds to reactants, reaction intermediates, or products.[35, 60] In accordance with the Sabatier principle, a catalyst with an optimal binding shows the highest activity in **Figure 6**a. Stronger or weaker binding leads to diminished activity towards the left or right of the volcano top, respectively. Such volcano plots constitute valuable guidelines for identifying active catalyst materials. However, its accuracy depends on the fundamental parameter on its x-axis, also named "descriptor", which is connected to the catalytic activity on the y-axis.

A Descriptor of Bond Strength. In a volcano plot, the catalytic activity (see Chapter 2.1.4) is plotted *versus* a suitable "descriptor". The latter provides a link to the fundamental properties of the catalyst surface or the electrochemical interface.[61] Ideally, the descriptor should be an integral part of the rate law.[62] Therefore, the adsorption energies of intermediates are commonly employed descriptors.[60] The strength of the adsorbate-surface bond can be experimentally accessed *via* the heat of formation.[61] However, only modern computational approaches allowed for a theoretical determination of descriptors, such as adsorbate binding energies.[60, 63]

The d-Band Model. A theoretical model used to predict activity trends is the d-band model. The electronic properties of transition metals, which are widely used catalysts, are governed by the structure and occupancy of their sp- and d-band states. A short introduction to the DOS of a transition metal is given in Chapter 2.2.1. Among different transition metals, the s- and p-bands behave similarly. Therefore, the bond between a specific transition metal surface and an adsorbate is determined by the interaction between the d-band states of the metal and the adsorbate orbitals. Only a single adsorbate orbital is considered for simplicity, as would be in the case for an atomic adsorbate. As discussed in Chapter 2.2.1, upon interaction with a transition metal, the adsorbate orbital will broaden in energy (sp-band interaction) and split into a bonding and antibonding state (d-band interaction, see **Figure 5**). A strong bond between adsorbate and catalyst is established if the occupancy of the antibonding states is low and *vice versa*. In turn, the occupancy of the antibonding orbital is set by the d-band centre (ε_d) in terms of energy relative to the Fermi level E_F. The higher the d-band centre, the higher is the position of the antibonding states (d-σ)*, the lower its occupancy, and thus the stronger the bond between

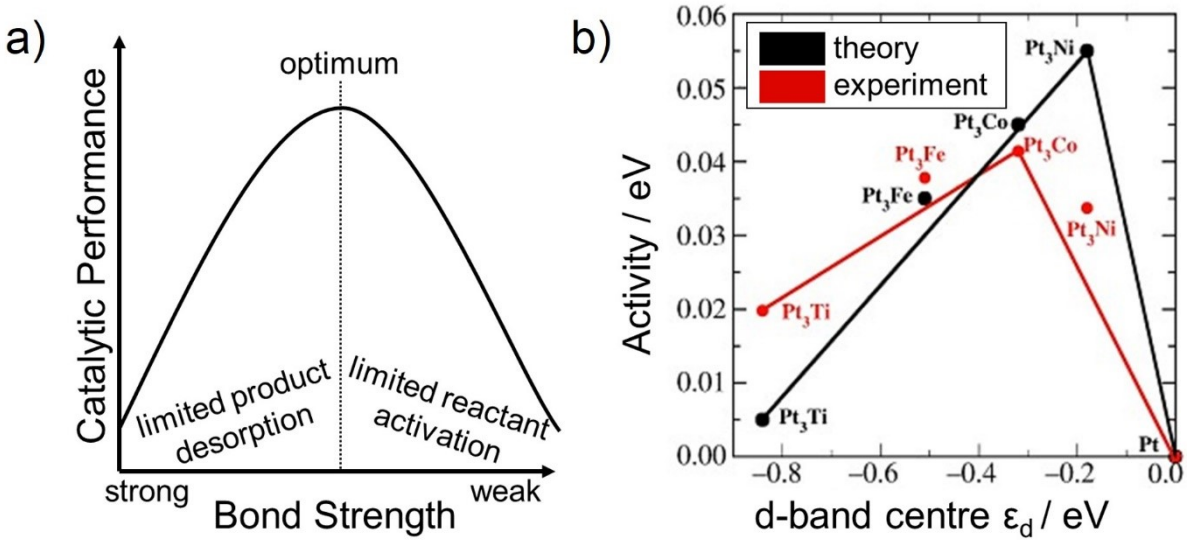

Figure 6 | a) Schematic of a volcano plot as quantification of the Sabatier principle. A descriptor for electrocatalytic activity is plotted against a descriptor for "bond strength" (*e.g.* heat of adsorption). According to the Sabatier principle, too strong binding leads to the inability of product desorption, whereas too weak binding may fail in reactant activation. Thus, intermediate binding yields optimal catalytic performance. Image adapted with permission from [60]. Copyright © 2015 Elsevier Inc. b) ORR activity against the d-band centre of the catalyst. Herein, ε_d was experimentally determined and is given relative to Pt. A higher d-band centre (as for pure platinum) translates to stronger binding of reaction intermediates. Therefore, alloying can lower the d-band centre and thus optimize binding. Reprinted with permission from reference [65]. Copyright ©2006 WILEY-VCH Verlag GmbH & Co. KGaA.

catalyst and adsorbate.[64] The relation between the d-band centre and the bonding strength between catalyst and adsorbate turns the former into a valuable descriptor. **Figure 6**b gives an example for a volcano plot depending on the d-band centre.[65] Herein, the experimentally obtained activity (red) is compared to the activity predicted by DFT calculations (black). Within

the d-band model, the catalyst surface is assumed to consist of equal surface sites, which is insufficient to describe a real catalyst surface.

Scaling Relations. So far, a single adsorbate was accounted for. Nonetheless, there is not only a single type of adsorbate in many reactions, but various adsorbates and intermediates are important. In principle, a suitable descriptor comprises the interactions between the catalyst surface and all the intermediates. The binding energies of adsorbates often scale linearly with each other.[66, 67] If so, it is possible to use the adsorption properties of a single intermediate as the descriptor. The simplified explanation for the correlation between the adsorption energies of different intermediates is that they adsorb through the same atom type. As an example, *O,*OH and *OOH adsorb by an oxygen-metal bond on the surface. Scaling relations can provide restrictions in catalyst design. Consider a reaction, which first involves the dissociation of a molecule (*e.g.* O_2), and last the desorption of the product, which is bound to the surface through the same kind of atom (*e.g.* *O). For the first step, a strong interaction between the surface and adsorbate is desirable for dissociation (see Chapter 2.2.1). However, at the same time, a weak interaction between the adsorbate and the surface is beneficial for product desorption. Thus, efforts have been made to break the scaling relations by adding foreign substances or creating three-dimensional structures.[68-70] A catalyst with changing geometry during the reaction would be capable of breaking the scaling relations as well. In nature, enzymes can do so.[71]

In summary, the Sabatier principle coupled with theoretical predictions serves as a valuable tool in material selection and catalyst design.

2.2.3 Active Sites and Structure Sensitivity

The Sabatier principle and the considerations stated in Chapter 2.2.2 assist in finding well-performing catalyst materials. However, they do not discern where on the surface the reaction takes place. A catalyst surface is not an ensemble of identical surface sites but can rather be seen as a "checkerboard".[72] In other words, the adsorption energy towards intermediates can differ from site to site because of dissimilarities in electronic and/or geometric structure.

Therefore, the surface does not necessarily contribute uniformly to the overall activity, but only certain "active sites".[27] Such active sites provide optimal binding towards reaction intermediates. An active site can be a single atom or an arrangement of atoms. Reactions that only take place at a specific surface site are termed "structure sensitive".[73, 74]

The nature of active sites depends on structural and electronic factors. Geometric factors may come into play, such as the coordination of surface sites. As an example, for the ORR active sites on Pt(111), sites of higher coordination than the "regular" terrace sites bind weaker. Such features can be found near the bottom of step edges or at concavities. *Vice versa*, spots of lower coordination, such as at the top of step edges or on convex nanoparticles, bind stronger.[31, 75, 76] Another structure-related factor is the occurrence of strain on the catalyst surface. Dissimilar atoms in the subsurface can influence the lattice spacing on the surface and induce strain. Again referring to the example of ORR intermediates on Pt surfaces, compressive strain leads to weakening the binding interactions. Conversely, tensile strain results in the opposite.[34, 77] Since only the ORR is considered here, it is important to point out that even if the surface geometry affects the binding conditions, the type of adsorbate is crucial as well. As a side note, certain surface motives, *e.g.* steps and terraces of a specific orientation, can bind different kinds of adsorbates, such as *OH, *OO,*CH, *CO, *etc.*, to a different extent. This subject is discussed in references [56, 73]. The electronic structure of a catalyst can be tuned by dissimilar atoms on the surface or subsurface (ligand effect).[78] An ensemble effect may arise if the active site constitutes dissimilar atoms.[79] For nanoparticulate catalysts, additionally, the size and shape of the particle and its interactions with the support come into play.[25, 78, 80] Besides, the properties of the electrochemical interface and the electrolyte composition should not be neglected.[78, 81]

The knowledge of the active sites for a specific reaction and catalyst material is essential since the performance can be optimised by maximising the number of exposed active sites on the surface. Computational and experimental procedures have been established to assess the nature of active centres. Since the adsorption properties depend on the spatial distribution of the electron density, binding energies can be modelled with DFT and used as suitable activity

descriptors. In an ideal experiment, it would be possible to resolve both the surface morphology and the chemical composition of the surface *in situ*.

For obtaining vital information, it is important to choose suitable model systems. A particular class of such surfaces are extended single crystal surfaces and thin films. Since they have a limited number of different structural motifs, the overall behaviour, *e.g.* the activity of the whole surface, can be assigned to said feature. Consequently, different single crystal surfaces with distinct properties can directly be compared to each other. An example of such a motif is the crystal orientation of the surface. Cutting a crystalline lattice in certain principal axis results in

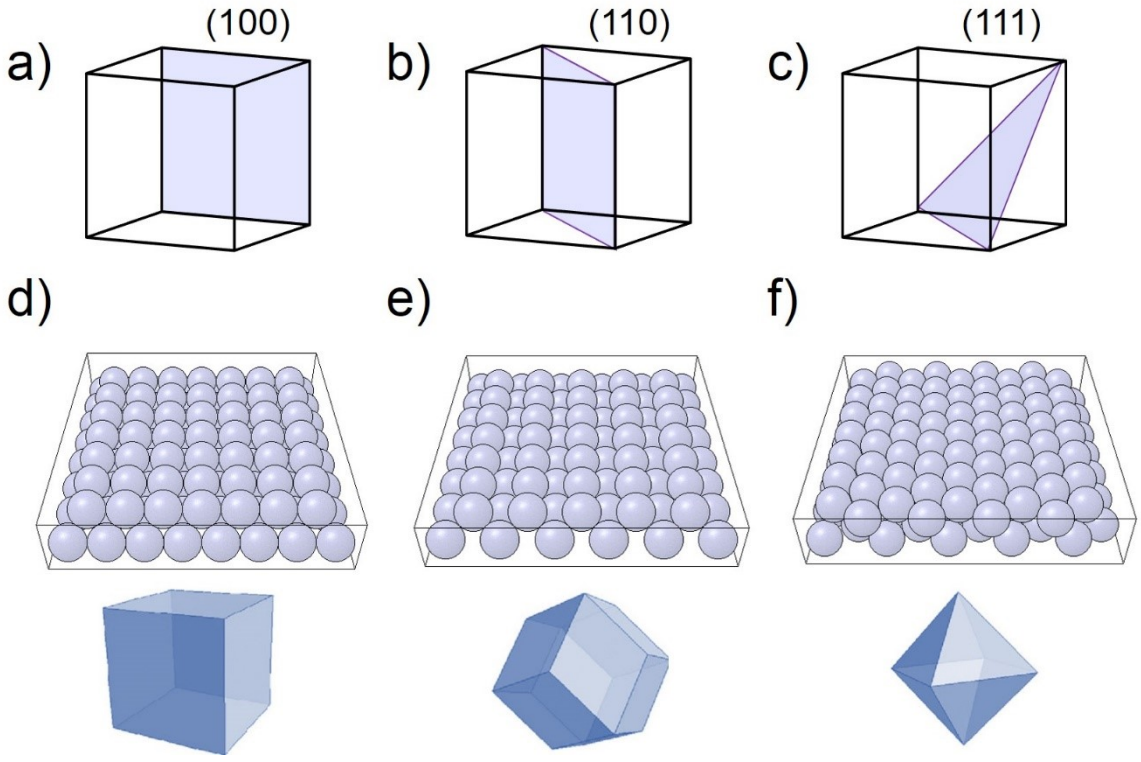

Figure 7 | Crystal planes in a cubic unit cell: a) (100), b) (110) and c) (111). Schematics of a d) (100), e) (110) and f) (111) surface and the shape of nanoparticles comprising the respective crystal facets: d) cubic, e) rhombic dodecahedron and f) octahedron. The images in d-f were created with the help of references [82] and [84].

a well-defined surface, as exemplarily shown in **Figure 7**.[82, 83] Since nanoparticles of particular shapes demonstrate well-defined crystal facets[84], studies on model extended surfaces can yield insights for real-world catalysts. Examples of such particles are given in **Figure 7** next to the respective extended surfaces. Cubic nanoparticles are comprised solely of (100) planes, rhombic dodecahedra of (110) planes and octahedra of (111) planes. However, as size effects and the interaction with the support may additionally influence the nature of active sites, transferring findings from extended model surfaces to nanoparticles requires precaution. Nonetheless, such model surfaces yield valuable insights. Due to their periodicity, they can also be modelled more easily, which can elucidate the binding properties of the surfaces.

In the next chapter, reactions related to electrolysis and fuel cell applications are discussed in detail. Findings on the actives sites on model systems are given for each respective reaction.

3 Catalytic Reactions on Model Surfaces in Fuel Cells and Electrolysers

In the centre of interest are the electrochemical reactions involved in PEMFCs and water electrolysers, which are sketched in **Figure 8** for the case of an acidic electrolyte. In such electrochemical devices, the redox reactions are spatially separated to take place at the two interfaces. While the electrons flow through the outer circuit, the membrane establishes ion conduction and prevents an electric shortcut. This thesis widely employs acidic media, where protons (H^+) are exchanged between the electrodes. Therefore, in the following, all reactions are given for acidic media.

In an electrolyser, an external potential is applied to drive the water-splitting reactions, *i.e.*, the HER and the OER.

anode (HER)	$4\ H^+ + 4\ e^-$	$\rightarrow$	$2\ H_2$	**Eq. 15**
cathode (OER)	$2\ H_2O$	$\rightarrow$	$O_2 + 4\ H^+ + 4\ e^-$	**Eq. 16**
overall reaction	$2\ H_2O$	$\rightarrow$	$2\ H_2 + O_2$	**Eq. 17**

A fuel cell harvests the free energy of water formation from hydrogen and oxygen in the form of electricity. In reality, this process is accompanied by losses, which lead to the release of waste heat.[85, 86] The reactions are termed hydrogen oxidation reaction (HOR) and ORR.

anode (HOR)	$2\ H_2$	$\rightarrow$	$4\ H^+ + 4\ e^-$	**Eq. 18**
cathode (ORR)	$O_2 + 4\ H^+ + 4\ e^-$	$\rightarrow$	$2\ H_2O$	**Eq. 19**
overall reaction	$2\ H_2 + O_2$	$\rightarrow$	$2\ H_2O$	**Eq. 20**

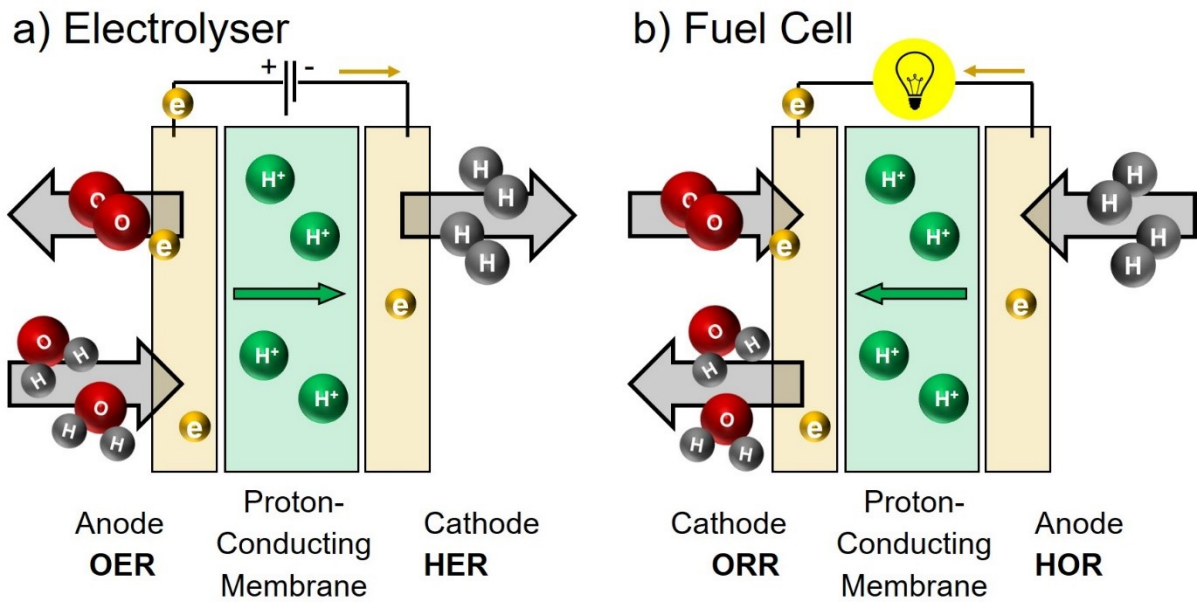

Figure 8 | A sketch of a PEM electrolyser and a fuel cell in an acidic medium. In each device, two separated redox reactions occur at each electrode-electrolyte interface. The devices convert chemical into electrical energy or *vice versa*. a) In an electrolyser, water splits into hydrogen (grey) at the cathode and oxygen (red) at the anode driven by an electric potential. b) In a fuel cell, hydrogen and oxygen are fed to the electrodes and are converted into water and electricity. Each of the reactions involves the transfer of electrons (yellow) through the outer circuit and protons (green) through the membrane.

For completeness, it is mentioned that water electrolysers and fuel cells can also operate in alkaline media. In alkaline electrolysers, hydrogen evolves from water, whereas oxygen is produced from hydroxyl anions (OH^-), which are exchanged between the electrodes. The respective reverse reactions occur in the alkaline fuel cell. Because of the less demanding conditions, less noble and thus less costly catalysts could be employed. However, liquid alkaline systems pose a lack of safety and reliability due to caustic soda circulating in the cell. The use of an alkaline polymer electrolyte membrane would overcome these issues. However, their performance is, to date, still lower than their pendant in acidic media.[19, 87]

In the next chapters, all four reactions are discussed in more detail for acidic media with a focus on the ORR and OER. More information on the materials investigated in this thesis is given in the respective chapters, which are iridium oxide (IrO_x) for the OER and platinum (Pt) and Pt alloys for the ORR.

3.1 Hydrogen Evolution Reaction

The overall reaction of the HER is given in **Eq. 15**. A schematic of the HER reaction mechanism in an acidic medium is shown in **Figure 9**a,b. It is widely accepted that the HER occurs in two consecutive steps.[48, 88, 89] The first step involves the adsorption of a hydrogen atom (Volmer step, **Eq. 21**). Here, a proton (H^+) adsorbs on a free catalytic site (denoted as "*" in the following). Upon a subsequent electron transfer from the catalyst, the proton is reduced to adsorbed atomic hydrogen (*H). After this so-called Volmer step, the HER can occur *via* two different pathways. The first possibility is the Tafel mechanism (**Eq. 22**). In this case, a second atomic hydrogen atom is adsorbed on the surface analogously to the Volmer step. In the end, both adsorbed hydrogen atoms migrate to each other on the surface, react and form molecular hydrogen (H_2), which subsequently desorbs. The alternative is the Heyrovsky mechanism (**Eq. 23**). Thereby, the second proton-electron charge transfer mechanism takes place directly at the first adsorbed atomic hydrogen. In the last step, molecular hydrogen (H_2) desorbs from the surface.

Volmer	$H^+ + e^-$	$\rightarrow$	*H	**Eq. 21**
Tafel	*H + *H	$\rightarrow$	H_2	**Eq. 22**
Heyrovsky	*H + $H^+ + e^-$	$\rightarrow$	H_2	**Eq. 23**

For each system, the HER mechanism depends on the properties of the electrified solid-liquid interface. The Tafel slope (see **Eq. 9** in Chapter 2.1.4) can serve as an indication for the rate-determining step.[45, 48, 90]. For Pt, it has been stated that at low overpotential, the recombination step determines the rate, whereas the initial discharge step is fast. As the overpotential increases, the coverage of adsorbed hydrogen increases. Therefore, atom-atom recombination is fast, and accordingly, the initial discharge step determines the rate.[45]

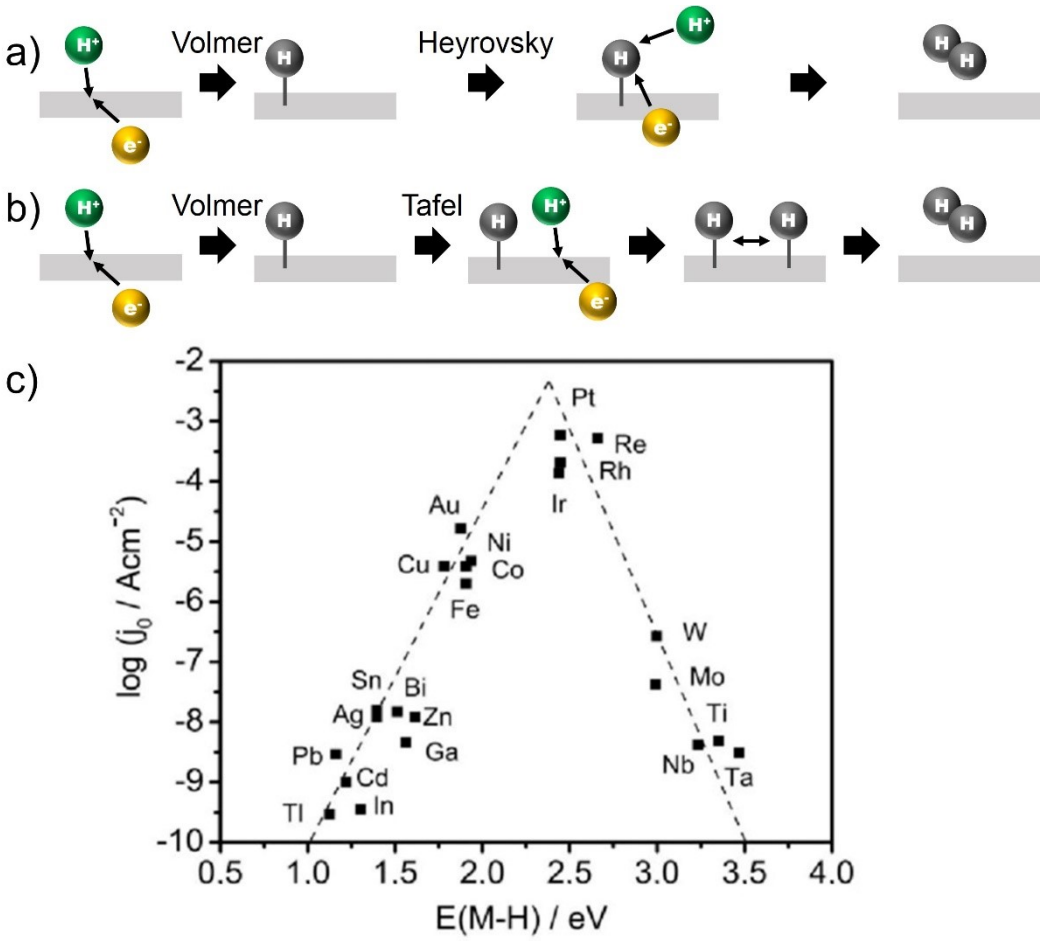

Figure 9 | HER mechanism in acidic media. In the first step, the adsorption of a proton (green) on an empty active site of the catalyst surface couples to an electron (yellow) transfer, which leads to an adsorbed hydrogen atom (grey). Hydrogen formation may then occur *via* two different pathways. a) In the Heyrovsky mechanism, the second proton and electron react directly with the adsorbed hydrogen atom and release a hydrogen molecule. b) Alternatively, in the Tafel step, the second proton adsorption-electron transfer leads to a second adsorbed hydrogen atom. In the last step, the reaction of both adsorbed hydrogen atoms produces molecular hydrogen. c) HER volcano plot as predicted by Trasatti *et al.* in 1972.[91] The descriptor is the bond strength between atomic hydrogen and the metal catalyst surface *E(M-H)*. Reprinted with permission from [62]. Copyright © 2016 Wiley-VCH Verlag GmbH & Co. KGaA.

Hence, the initial discharge step (**Eq. 21**) and the subsequent recombination step (**Eq. 22** or **Eq. 23**) can both limit the rate. These steps involve the ad- and desorption of hydrogen, respectively. According to the Sabatier principle (Chapter 2.2.2), an ideal catalyst should be able to balance the hydrogen binding strength, *E(M–H)*. The latter can be a suitable descriptor for the HER, as shown in the volcano plot in **Figure 9**c.[91] Herein, noble metals (*e.g.*, Pt) are located close to the top of the volcano, showing hydrogen bond strengths slightly larger than optimal. On the right branch are the early transition metals, which bond even stronger. *Vice versa*, the sp-metals with weak hydrogen bonding are placed on the left side of the volcano.[62]

First reports describing the promising electrocatalytic properties of Pt toward the HER already date back to the beginning of the 19th century.[92, 93] However, due to its limited availability and high costs, promising alternatives have been investigated. Among them are Pt group metal-alloys, transition metal-chalcogenides (*e.g.*, MoS_2), transition metal-carbides (*e.g.*, tungsten and molybdenum carbides) and metal-free materials.[50, 94, 95]

3.2 Hydrogen Oxidation Reaction

The overall HOR is given in **Eq. 18**. It proceeds *via* the same consecutive steps as the HER described before. HER and HOR can be considered as symmetric forward and backward reactions, *i.e.*, the transfer coefficient of the Butler-Volmer equation (**Eq. 6** in Chapter 2.1.4) can be set to $\alpha = 0.5$.[96] Therefore, the same descriptors and trends for the HER also apply to the HOR. Accordingly, a suitable descriptor for the HOR is the binding interaction between adsorbed hydrogen and the catalyst surface.[97-99]

The state-of-the-art catalyst for the anode reaction of a PEMFC is Pt. Even though Pt is a precious material, the catalyst loading required in fuel cell application is low. In numbers, 0.05 $mg_{Pt}\,cm^{-2}_{geo}$ is sufficient to catalyse the HOR without efficiency losses, *i.e.*, at overpotentials smaller than 5 mV.[39, 100, 101] Besides pure Pt, alloys of Pt such as Pt-Ru are promising HOR catalysts. However, rather because of their increased CO tolerance than performance gains.[102] In the search for less noble HOR catalysts, transition metal carbides and oxides play an important role. Still, they cannot compete with Pt yet.[103] In total, due to the

high mass activity of Pt towards the HOR, the current research focus in fuel cell applications is mostly set to the cathode reaction and the development of the membrane materials.[39]

3.3 Oxygen Evolution Reaction

The sustainable production of fuels like hydrogen from water or hydrocarbons from CO_2 requires a counterbalancing electron-donating reaction. Currently, the most sustainable and available candidate is the OER. However, the OER is a complex multistage reaction, which includes four proton-electron transfer steps. Therefore, even if using benchmark catalysts, a considerably large overpotential is required.[87]

Hence, it is essential to understand the fundamentals of the OER to design well-performing catalyst materials. In the past, different hypotheses on the OER mechanism have been proposed. Involved in the reaction are key intermediates such as *O, *OH and *OOH. For illustration, two exemplary OER pathways are presented here. In the first step of the OER, water is oxidised on the catalyst surface, which yields adsorbed hydroxyl species (*OH) as given in **Eq. 24**. Subsequently, *OH undergoes deprotonation and becomes *O (**Eq. 25**). Lastly, the catalyst liberates oxygen gas, *cf.* **Eq. 26**.[104] An alternative pathway was proposed by DFT calculations[67, 105, 106] and was experimentally confirmed[107]. Here, *via* an associative mechanism, the oxidation of a second water molecule forms *OOH on the surface (**Eq. 27**). At last, deprotonation leads to the release of oxygen (**Eq. 28**).

I	$H_2O + *$	$\rightarrow$	$*OH + H^+ + e^-$	**Eq. 24**
II	$*OH$	$\rightarrow$	$*O + H^+ + e^-$	**Eq. 25**
III a	$2\ *O$	$\rightarrow$	$2\ * + O_2$	**Eq. 26**
		or		
III b	$*O + H_2O$	$\rightarrow$	$*OOH + H^+ + e^-$	**Eq. 27**
IV b	$*OOH$	$\rightarrow$	$* + O_2 + H^+ + e^-$	**Eq. 28**

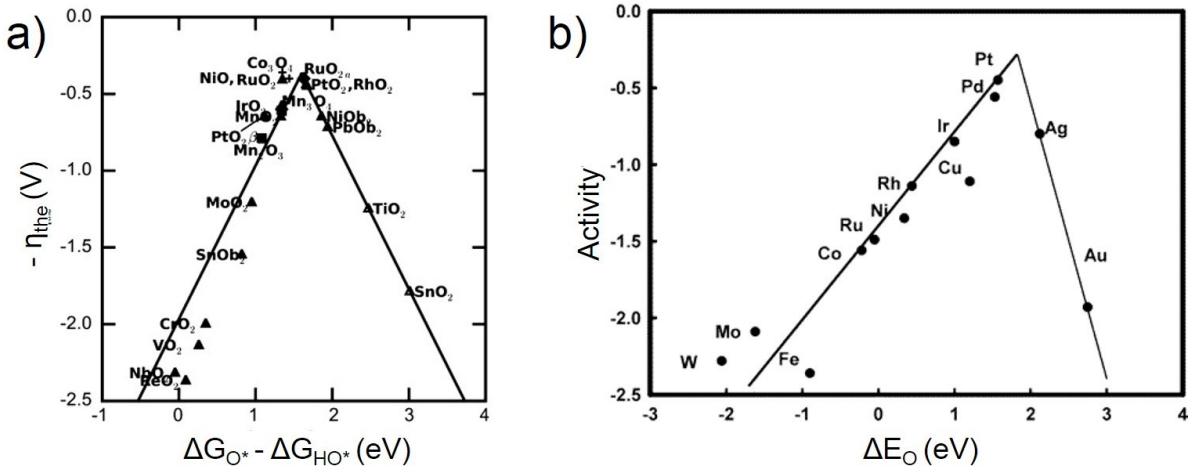

Figure 10 | a) OER volcano plot predicted by DFT calculations. Reprinted with permission from [105]. Copyright © 2011 WILEY-VCH Verlag GmbH & Co. KGaA. b) ORR volcano plot for single metal catalysts. Reprinted with permission from [132]. Copyright © 2004, American Chemical Society.

As for the HER and HOR, the binding energies of intermediates can be employed as descriptors to predict activity trends. For the OER, three descriptors play an important role involving the OER key intermediates: ΔG_{*O}, ΔG_{*OH} and ΔG_{*OOH}. However, these binding energies are not independent of each other but interrelated *via* scaling relations (see Chapter 2.2.2). The following relation has been stated to hold irrespectively of the catalyst surface: $\Delta G_{*OOH} - \Delta G_{*OH} = 3.2$ eV.[67, 73] The existence of a constant value for different materials implies that *OH and *OOH adsorb preferentially at the same type of binding sites. It can thus be concluded that only two binding energies suffice to describe activity trends in the OER, such as *e.g.* the difference of the two binding energies $\Delta G_{*O} - \Delta G_{*OH}$. An example of a volcano plot using $\Delta G_{*O} - \Delta G_{*OH}$ as the descriptor is given in **Figure 10**a.[105] The theoretical overpotential η_{the} was used as the activity descriptor. It was determined by the difference between the reaction free energy of the rate-determining step and the thermodynamic equilibrium, *i.e.* 1.23 eV for the OER. Towards the left of the volcano, the materials bind oxygen species too strongly, and therefore the third step (*OOH formation, **Eq. 27**) is the potential limiting one. *Vice versa*, on the right of the volcano, the catalyst surfaces bind too weakly, and hence the second step, the

deprotonation of *OH species, is the limiting one (**Eq. 25**). Close to the optimum, ruthenium oxide (RuO_2) is located.[105, 108]

OER Mechanism on Iridium Oxide Surfaces

Besides catalytic activity, stability is one of the key properties of a catalyst. Even though possessing lower intrinsic OER activities, the stability of Ir oxide catalysts outperforms their Ru-based counterparts.[109-111] This paragraph is therefore dedicated to Ir oxide (IrO_x) catalysts. Compared to rutile Ir oxide, it has been shown that the amorphous and hydrated character of IrO_x, which is formed during electrochemical cycling, is beneficial for OER activity.[112-117] It was stated that an increase in crystallinity is equivalent to a decrease in OER activity.[112, 113] The oxidation states of the active Ir atoms and the OER mechanism itself have been subject to many studies. Still, ongoing controversies on these themes can be observed in the scientific community.

Generally, the proposed OER mechanisms on the Ir oxide surface can be divided into the two pathways introduced above: a) a coupling mechanism (**Eq. 24**–**Eq. 26**) and b) an acid-base mechanism (**Eq. 24**, **Eq. 25**, **Eq. 27**, **Eq. 28**). In the coupling pathway, the formation of the O-O bond takes place *via* two *O on adjacent adsorption sites. During this step (**Eq. 26**), no electrons are transferred. A possible pathway is a transition between $Ir^{IV}O_2$, $Ir^{V}O_2OH$ and $HIr^{III}O_2$.[118] At high potentials (>1.6 V_{RHE}), even Ir^{V} to Ir^{VI} transitions were predicted.[118] Many efforts have been made to identify Ir^{V} species either *ex situ* or under potential control.[119-121] Even though Ir^{V} and Ir^{VI} species could be isolated from the crystalline bulk[122], it remains unclear if such species can as well build up on the surface of IrO_2. In the case of an acid-base mechanism, an interesting model has been proposed by Schlögl *et al.* for the OER on amorphous Ir oxide.[123-125] Herein, the presence of Ir-vacancies contributed to the formation of active "O^{I-} species". Such electrophilic oxygen species are prone to nucleophilic attack. This implies that the OER is taking place *via* the adsorption of an *OOH group after the oxidation of the "first" water molecule.

To date, none of the above-mentioned mechanisms was confirmed or dismissed. Nonetheless, it can be mentioned that the Ir species located at a binding energy of 62.5 eV in X-ray Photoelectron Spectroscopy (XPS) measurements were assigned as active.[123-126] Even though their oxidation state remains under debate, their ratio has even been proposed as a suitable OER descriptor.[127] In contrast to the oxidation state, little is reported on the coordination or surface structure of the OER active sites on IrO_x. To fill this void, IrO_x is subject to the studies reported in this thesis (Chapter 6).

3.4 Oxygen Reduction Reaction

Similar to the OER (Chapter 3.3), the ORR can also be considered a complex multistage reaction. It includes the transfer of four electrons, the cleavage of the O-O bond and the consecutive protonation *via* several steps and intermediates. A controversy exists over the exact reaction mechanism. Two conceivable pathways are introduced and illustrated in **Figure 11**a. In the first, oxygen (O_2) is directly reduced to water *via* a four-electron transfer (**Eq. 19**, step (1) in **Figure 11**a). Alternatively, the ORR proceeds in two successive two-electron transfer steps involving hydrogen peroxide (H_2O_2) as an intermediate or side product (**Eq. 29**-**Eq. 30**, step (2-3) in the sketch). Therefore, the indirect pathway includes the competing side-reaction of the H_2O_2 formation (step (4) in **Figure 11**a).[128]

$$O_2 + 2\,H^+ + 2\,e^- \rightarrow H_2O_2 \qquad \textbf{Eq. 29}$$

$$H_2O_2 + 2\,H^+ + 2\,e^- \rightarrow 2\,H_2O \qquad \textbf{Eq. 30}$$

The ORR activity and pathway both strongly depend on the cleavage of the O-O bond.[129] Experiments suggest that within the series pathway, it takes place in the second step (**Eq. 30** and step (3) in **Figure 11**a).[130, 131] In general, the O-O bond can be broken *via* an associative mechanism, where *OOH is formed before the O-O bond cleavage or *via* a dissociation mechanism, in which the O-O bond is cleaved before *OH is formed.[132] The process of the ORR is primarily governed by the surface properties of the catalyst material in question. Despite intensive research, the reaction mechanism is challenging to access because experimental

techniques cannot capture all intermediates involved in such a complex process. Moreover, electron transfer can only be studied in the activation region, which is limited to a small potential range near the onset of the reaction.[133] Independent of the exact pathway, the key intermediates of the ORR include oxygen (*O), hydroxyl (*OH) and superhydroxyl (*OOH) species. As for the OER, the binding strength of these intermediates to the catalyst surface can be suitable descriptors for activity trends.[66, 132, 134] In addition, scaling relations are to be considered (see Chapter 2.2.2). **Figure 10**b shows such a volcano plot using the oxygen binding energy (here denoted as ΔE_O) as the descriptor.[132]

Today, Pt-based catalysts achieve the highest ORR performances. However, as shown in **Figure 10**b, Pt binds stronger than optimal. A promising route to reduce the binding strength of Pt and to lower the Pt content is to alloy Pt with, *e.g.*, transition metals. The following chapters review the use of Pt and its alloys for ORR electocatalysis.

3.4.1 Platinum

The ORR on Pt surfaces is structure-sensitive, so the activity depends on the geometric and electronic properties of its surface.[135] Activity measurements can determine the geometry of active sites on model surfaces with well-defined crystal planes.[56, 132, 133, 136] In the following, the outcomes of these studies are summarised. Here, the focus lies on the reaction taking place in an acidic electrolyte. Importantly, the nature of active sites also depends on the used electrolyte.[81, 135, 137]

In weakly-adsorbed electrolytes such as perchloric acid ($HClO_4$), the following activity trend was stated for low-index surfaces: Pt(100) < Pt(111) < Pt(110).[138] To access high-index planes, systematic studies on stepped single crystals were carried out.[139-142] They revealed that the ORR activity is highly dependent on the orientation of the steps and terraces on the surface. As an example, the ORR activity trends on Pt[n(111)x(hkl)] have been measured for (hkl) = (111) and (100).[139, 141, 142] In this way of notation, *n* denotes the terrace width of orientation (111), and (hkl) defines the facet of the monoatomic steps. The outcome of the report is

summarised in **Figure 12**a.[143] From these observations, the ORR activity is increasing with increasing step density.[142]

An elegant complement to understand the experimental trends reported for stepped single crystals is to relate the geometry of a certain surface site to its activity. Thereby, "coordination-activity" plots can be obtained.[31, 76] In this approach, the generalised coordination number $\overline{CN}$ can function as a descriptor for the binding strength of adsorbates.[75] The generalised coordination number of a site i with n_i nearest neighbours can then be calculated using **Eq. 31**.[31, 75, 76]

$$\overline{\mathrm{CN}}(\mathrm{i}) = \sum_{\mathrm{j}=1}^{\mathrm{n_i}} \frac{\mathrm{cn(j)}}{\mathrm{cn_{max}}} \qquad \textbf{Eq. 31}$$

$\overline{CN}$ is defined as the sum over the number of nearest neighbours, where each neighbour j is weighted by its coordination number $cn(j)$. The sum is then normalised to the maximum number of nearest neighbours in the bulk cn_{max} to ensure that the generalised coordination numbers lie between zero and cn_{max}. The conventional coordination number cn is the sum of the nearest neighbours of a certain site. In a bulk *fcc* single crystal such as Pt, $\mathrm{cn_{max}} = 12$. Coordination numbers below 12 are typical for surface sites. As an example, a terrace site (t) of the (111) surface possesses six nearest neighbours on the surface (cn = 9) and three in the bulk (cn = 12). This leads to a generalised coordination number of $\overline{\mathrm{CN}}_\mathrm{t} = (6\times9 + 3\times12)/12 = 7.5$.

In general, surface atoms have a higher tendency to form bonds to compensate for the lack of coordination. It turned out that the adsorption energy on Pt surfaces towards *O, *O_2, *OH, *OOH, *H_2O, and *H_2O_2 increases linearly with $\overline{CN}$. The lower the coordination of a surface site, the stronger the binding towards intermediates, and *vice versa*.[75]

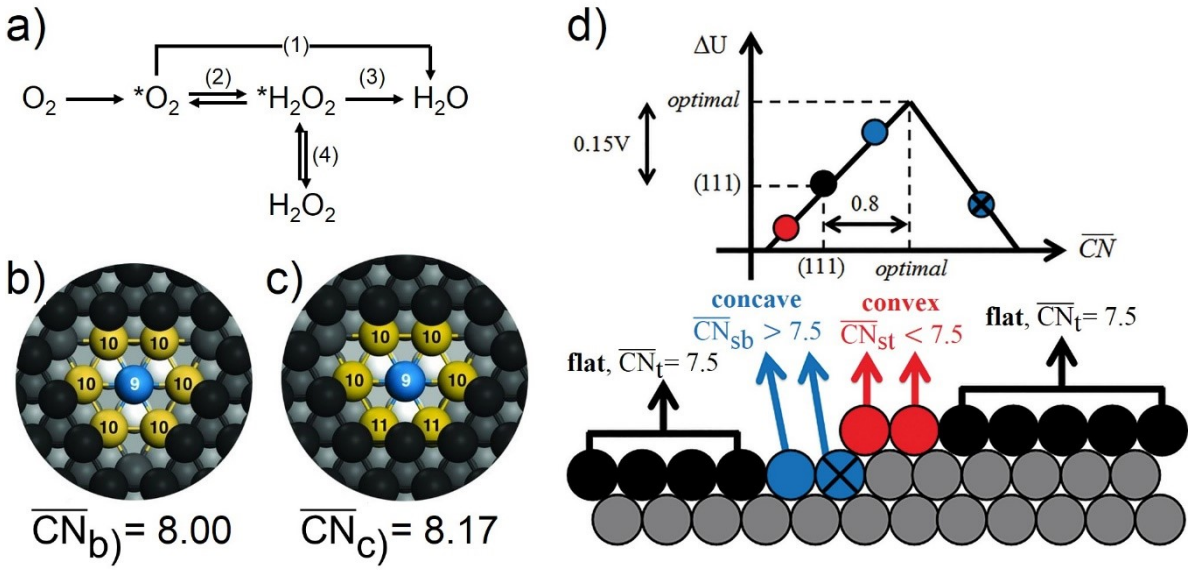

Figure 11 | a) ORR pathways as introduced by Wroblowa *et al.*[128] Oxygen can either (1) be directly reduced to water or (2-3) in a series of two successive two-electron transfers, which involves hydrogen peroxide as an intermediate. The latter pathway competes with (4) the side reaction of the hydrogen peroxide evolution. b,c) Generalized coordination numbers can be geometric descriptors for bond strength and are defined in **Eq. 31**. For the ORR on Pt(111), $\overline{CN}$ ≈ 8.3 was predicted as optimum. Two examples of one-layer-deep concavities with $\overline{CN}$ close to that value are given here. Image reprinted with permission from [31]. Copyright © 2015, American Association for the Advancement of Science. d) Surface sites of different coordination as they appear near a monoatomic step on a Pt(111) surface. Flat terrace sites (black) bind ORR intermediates stronger than optimal. Sites of lower coordination near the top of the step edge (red) bind even stronger and thus lead to even lower activity as shown in the volcano plot. *Vice versa*, sites of higher coordination near the bottom of the step (blue) bind weaker and thus are postulated to be more active. The bottom of the step (blue cross) is unlikely to contribute to the reaction due to steric hindrance. Image reprinted with permission from [76]. Published by The Royal Society of Chemistry.

The principle of generalised coordination numbers has subsequently been employed to predict the geometry of active bindings sites for the ORR on Pt(111) surfaces. DFT calculations showed that Pt sites with $\overline{CN} \approx 8.3$ yield optimal reaction energies. This implies that ideal binding sites should possess more nearest neighbours than (111) terrace sites. However, sites with a higher number of first-order nearest neighbours acquire generalised coordination numbers between 8.75 and 9.5. Therefore, they are located on the weaker binding side of the volcano and are problematic due to steric hindrances. Instead, superior binding sites have the same amount of first-order nearest neighbours as (111) terraces but more second-order nearest neighbours. Promising sites approaching the ideal generalised coordination number are one-layer-deep cavities. Examples are given in **Figure 11**b and c. In **Figure 11**b, the site highlighted in blue possesses six nearest neighbours with cn = 10 on the surface (yellow) and three with cn = 12 in the bulk (white). Therefore, $\overline{CN_{b)}} = (6\times10 + 3\times12)/12 = 8.00$. In **Figure 11**d, the concavity (blue) possesses four nearest neighbours with cn = 10 and two with cn = 11 on the surface (yellow), and three in the bulk (white). Thus, $\overline{CN_{c)}} = (4\times10 + 2\times11 + 3\times12)/12 = 8.17$.[31] Engineering particles or extended surfaces with such types of concave defects has led to significant activity improvements.[22, 31, 144-150] Noteworthy, it is not the undercoordinated sites that improve the ORR activity of Pt surfaces but the highly coordinated sites in their vicinity.[76] This explains why stepped single crystals show superior ORR activities.[139-142] In agreement with these findings, using n-EC-STM, the ORR active sites on Pt(111) were monitored near step edges.[54, 151]

The relation between the geometry of surface sites and their ORR activity is summarised in **Figure 11**d for Pt(111). In line with previous reports[65, 132, 152], terrace sites, coloured in black, bind stronger than optimal. Sites of higher coordination bind weaker and *vice versa*. Therefore, sites near the top of a step edge (st, red) bind stronger than terrace sites, whereas sites near the bottom of the step (sb, blue) bind weaker. The sites marked by the blue cross are unlikely to contribute to the reaction due to steric hindrance.[76]

For completeness, trends obtained *via* activity measurements on stepped single crystals in alkaline media are mentioned as well. In 0.1 M NaOH, Pt(111) showed the highest ORR

activity compared to Pt(100) and Pt(110). Here, the activity decreased with increasing step density.[153] In line with these findings, n-EC-STM identified terrace sites as active in an alkaline medium.[154]

3.4.2 Platinum Alloys

Even though Pt is the best-performing single-metal ORR catalyst, it does not offer optimal binding conditions from experimental measurements and a theoretical point of view. Instead, *O and *OH, which both play an important role in the ORR rate-determining steps, should be bound to Pt(111) by *ca.* 0.2 eV and *ca.* 0.1 eV weaker, respectively.[65, 132, 152] A promising approach that lowers the intermediate binding energy is the alloying with early (*e.g.* Sc, Y) or late (*e.g.* Fe, Co, Ni) transition metals (M).[152, 155-157] Among them, a record-high ORR activity has been reported for the extended $Pt_3Ni(111)$ surface in an acidic medium, which was almost ten times higher than on Pt(111). The surface of this alloy binds *OH *ca.* 0.13 eV weaker than Pt(111) which is close to the predicted optimum.[148] Inspired by these findings, many researchers have synthesised Pt_xNi nanoparticles with high performance.[147, 158-160] Furthermore, lanthanides have been considered as alloying elements, which, due to their negative heat of formation, tend to be more stable in an acidic environment.[158, 161, 162] Type and amount of the alloying material have a considerable impact on the ORR (detailed summary in reference [163]).

The better performance of Pt alloy catalysts compared to pure Pt can be related to the so-called ligand and strain effects. Ligand effects arise from the combination of Pt with dissimilar neighbouring atoms, which influence their electronic structure and adsorption behaviour.[164] Strain effects originate from a mismatch in lattice parameters between the surface and the bulk.[165-167] A pure Pt layer forms on the surface of a PtM bulk by electrochemical cycling in an acidic medium. The compressive strain introduced in the Pt surface leads to a downshift of the d-band centre[148], weaker binding of the ORR intermediates[77, 168, 169] and, in turn, to a higher ORR performance. Moreover, the dissolution of the transition metal atom ("de-alloying") during electrochemical cycling can induce significant changes in activity due

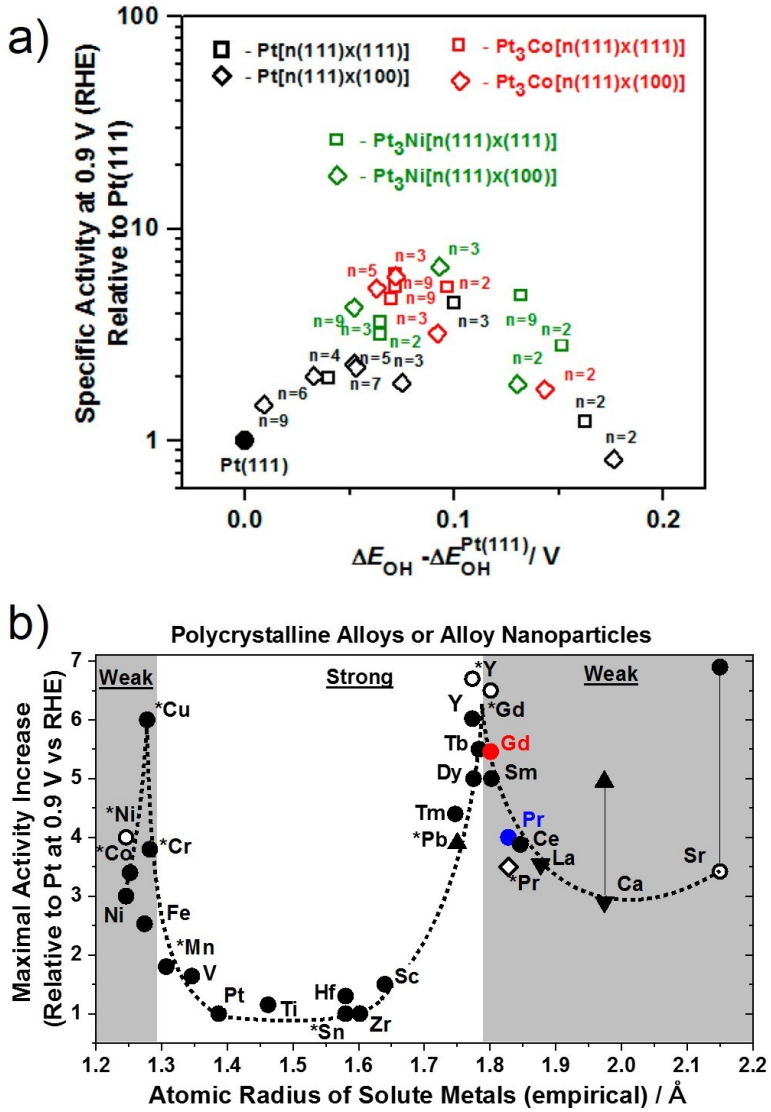

Figure 12 | ORR activity trends on Pt alloy surfaces. a) Summary of studies on stepped single crystal surfaces with (111) orientation of the terraces. The volcano plot can assist in accessing the geometry of the active sites, be they related to terrace or step sites. Image reprinted with permission from reference [128]. Copyright © 2016, American Chemical Society. b) Maximal reported relative activities of Pt alloy catalysts toward the ORR, at 0.9 V_{RHE}, in comparison to the corresponding Pt catalyst, plotted versus the empirical radius of the solute metal. Open symbols and asterisks denote spherical nanoparticles, bold symbols extended surfaces. Image reprinted with permission from references [128] and [243]. Copyright © 2016, American Chemical Society and © 2018 Elsevier B.V. The data point for the concave Pt_5Pr nanoparticle (diamond symbol) stems from reference [111].

to the formation of a strained Pt overlayer.[170]

Even if it is widely accepted that ligand and stain effects play a key role in the ORR performance of Pt alloys, the geometry of active sites remains inaccessible. Inspired by its outstanding performance, the focus of this discussion lies on Pt_3Ni single crystal surfaces. For comparing low-index $Pt_3Ni(hkl)$ surfaces, the order of activity was determined to be $Pt_3Ni(100) < Pt_3Ni(110) \ll Pt_3Ni(111)$.[148] The high activity of $Pt_3Ni(111)$ surfaces also holds for nanoparticles. Here, it was reported that Pt_3Ni particles of octahedral shape exposing (111) facets are superior to cubic shapes exposing (100) facets.[171] While there are indications of the high activity of (111) terrace sites, the role of the step sites in the catalytic process is more difficult to extract. In this regard, studies on model single crystal surfaces were undertaken[171, 172] and are summarised for Pt_3Ni and Pt_3Co in **Figure 12**a.[143] For Pt_3Ni stepped single crystals, Hoshi *et al.*[172] state that the occurrence of (111) step sites on a (111) surface is detrimental to the ORR activity. On the other hand, the series $Pt_3Ni[n(111)–(100)]$ showed a theoretical optimum for n = 4. The corresponding crystal, however, seemed too unstable to be synthesised. From their experiments, they concluded that (100) step sites are more active than (111) step sites. Still, from **Figure 12**a, it is difficult to establish a clear connection between step density and activity. The determination of the active sites would be helpful for understanding but remains still under debate for this system. Therefore, n-EC-STM was applied to $Pt_3Ni(111)$ and is reported in Chapter 8.

Besides single-crystalline alloys, polycrystalline alloys have been subject to several research studies in the past. As mentioned previously, the operation under ORR conditions in an acidic medium drives the less noble metal (M) to dissolve from the surface of the alloy. Since this so-called “de-alloying” process takes place predominantly at defect sites, polycrystalline surfaces are more prone to de-alloying.[173, 174] Following this process, the electrode surface is thus stabilised by the formation of an overlayer consisting solely of Pt.[161] The thickness of the Pt overlayer was determined to multiple atomic layers.[158, 175] Since ligand effects were shown to be negligible after only three atomic layers[176, 177], it can be deduced that strain is the dominant factor in the ORR activity of polycrystalline alloys[143]. Since the strain is introduced by the

lattice mismatch of the Pt overlayer and the alloyed core, a simple approach is to use the atomic radius of the alloying partner as a descriptor. This is shown in **Figure 12**b for multiple extended and nanoscale polycrystalline Pt alloy surfaces. The activity enhancement factor is given with respect to the pure Pt reference sample. All values were recorded in 0.1 M $HClO_4$, and the nanoparticles showed a "classical round" shape. A clear relation between the solute element radius and the activity can be seen, which manifests itself as a "double volcano". Starting from Pt and moving to the left, solute atoms with small radii introduce compressive strain, which lowers the binding energy toward adsorbates. At a certain point (close to Cu), the binding is optimal, and the activity is maximal. Further introduction of strain lowers the binding energy too much and is detrimental to the activity (the grey area on the left). Similar trends occur for alloying Pt with metals of large radii. Moving from Pt to larger radii, the activity reaches a maximum (near yttrium). It decreases for elements with larger radii since the introduction of too much compressive strain leads to a too weak binding (the grey area on the right).[155] The fact that atoms with a larger radius than Pt introduce compressive stain may seem counter-intuitive at first. The reason for this behaviour is that the Pt overlayer is not epitaxial to the core, but the shell rather forms a distinct structure which leads to the Pt shell atoms to lie closer to each other compared to the unstrained Pt *fcc* surface.[178] However, the exact mechanism of the surface relaxation remains unclear. In summary, using structural descriptors to explain the ORR activity of Pt and its alloys is a valuable approach. Direct assessment of the geometry of active sites would be beneficial to understand the behaviour of these model systems. Motivated by the literature report, n-EC-STM was applied to polycrystalline Pt_5Pr and Pt_5Gd surfaces, which is given in Chapter 7.

4 Experimental Techniques and Instrumentation

The scope of this thesis is to identify active sites using EC-STM. As this technique cannot distinguish the elementary composition or the crystalline orientation of the surface, complementary procedures are necessary. In this chapter, an introduction to the working principles of each method is provided alongside the instrumentation and the materials used in this work.

4.1 Cyclic Voltammetry and Rotating Disc Electrode Experiments

Cyclic voltammetry (CV) can access processes at the electrified solid-liquid interface. It is carried out using a three-electrode configuration (Chapter 2.1.3). Hereby, a potential is applied to the WE in a triangular waveform. That means that the potential is linearly ramped up and down at a fixed scan speed between a lower and higher potential limit. Simultaneously, the current is recorded and typically plotted *versus* the potential.[40]

An example of a CV of Pt(111) in 0.1 M $HClO_4$ is given in **Figure 13**a.[31] In such a CV, several ad- and desorption processes can be identified. The shape and position of the corresponding peaks are characteristic of a certain material and the orientation of the surface. Close to 0 V_{RHE}, the onset of the HER can be seen. As in **Figure 13**a, the subsequent plateau between 0.07 and 0.35 V_{RHE} is caused by the ad- and desorption of hydrogen (grey area). If applicable, additional peaks in this plateau would be explained by additional contributions of facets other than (111) on the surface.[25] Between 0.35 and 0.6 V_{RHE}, the electrified solid-liquid interface behaves like a capacitor. This region is called the double layer region. At *ca.* 0.8 V_{RHE}, a pair of sharp peaks can be found, which are denoted as "butterfly" peaks (green area). This feature can be assigned to a disorder-order transition[179] and reflects the generation of PtOH likely to occur in two steps. Eventually, at potentials between 1.0 and 1.15 V_{RHE}, a well-defined peak grows until an

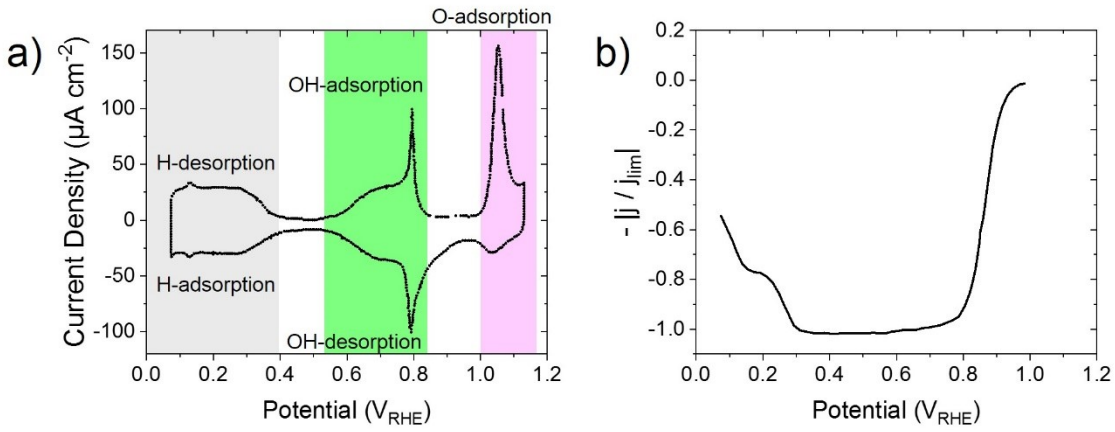

Figure 13 | a) CV of Pt(111) recorded in Ar-saturated 0.1 M $HClO_4$ at 50 mV s^{-1} scan rate. b) Polarization curve of Pt(111) in O_2-saturated 0.1 M $HClO_4$, performed at 50 mV s^{-1} scan rate and 1600 rpm rotational speed. Data reprinted from references [31] and [180].

organised PtO layer is acquired (red area). The application of higher potentials (not shown in the CV in **Figure 13**a) drives the OER.[133]

Besides CV measurements to understand the electrochemical properties, rotating disc electrode (RDE) experiments can assess the activity. In an RDE set-up, the WE rotates with constant speed, which enables steady-state mass transport investigations. The sides of the sample are covered with an inert material such as polytetrafluoroethylene (PTFE) to establish a well-defined surface area, which is in contact with the electrolyte. Due to forced convection, a constant flow of electrolyte to and from the surface is ensured.[40] An example of a polarisation curve carried out on a Pt(111) surface in O_2-saturated 0.1 M $HClO_4$ at a rotational speed of 1600 rpm is shown in **Figure 13**b.[180]

In general, since the reactant is consumed at the WE surface, the surface concentration is lower than in the bulk of the electrolyte. The current decreases, if the reactant concentration on the electrode surface is low (mass transfer limitation). Thus, the limiting current density j_{lim} is the maximal current density, which can be obtained in an RDE experiment. It depends on the angular velocity of the WE ω and the bulk reactant concentration c_0 according to[40]

$$j_{lim} \propto \omega^{1/2} c_0. \qquad \textbf{Eq. 32}$$

The absolute value of the limiting current j_{lim} can assess the intrinsic activity of a catalyst and eliminate mass transfer effects. The so-called kinetic current j_{kin} is connected to the measured current density j and the limiting current *via*[181, 182]

$$\frac{1}{j} = \frac{1}{j_{kin}} + \frac{1}{j_{lim}}. \qquad \textbf{Eq. 33}$$

It is common to give the ORR activity as the kinetic current density in the anodic scan of the polarisation curve at a potential of 0.9 V_{RHE}, where the kinetic information is available[183], and to rotate at a speed of 1600 rpm.[181, 182]

In this thesis, CV measurements were conducted in Ar-saturated electrolytes (Argon 5.0, Westfalen). The RDE (Pine Instrument Company) experiments were performed in O_2-saturated electrolytes (Oxygen 4.5, Linde). Results were 85 % iR-corrected for the electrolyte resistance obtained from electrochemical impedance spectroscopy. Potential control was given by a BioLogic VSP-300 potentiostat (BioLogic, France) with the corresponding EC-Lab® software (V11.30). Potentials were recorded either against a mercury-mercurous sulphate (MMS, Schott, Germany) or against a reversible hydrogen electrode (RHE, HydroFlex®, gaskatel). A Pt wire CE (99.9 %, Goodfellow, Germany) completed the electrochemical set-up. The cell was regularly cleaned with "Caro's acid", a solution of 3:1 ratio of H_2SO_4 (96 %, Roth) and H_2O_2 (30 %, Roth), and subsequently rinsed with boiling ultrapure water multiple times. The acidic electrolyte was prepared by diluting perchloric acid, $HClO_4$ (Merck Suprapur®, 70%), with ultrapure water. For the alkaline medium, potassium hydroxide pellets, KOH (99.99%, Sigma Aldrich) were dissolved in ultrapure water (18.2 MΩ) from an Evoqua Ultra Clear 10TWF 30 UV (Evoqua, Germany) water purification system.

4.2 Scanning Tunnelling and Atomic Force Microscopy

As a complement to the electrochemical techniques discussed before, scanning probe techniques were used in this work to access the surface morphology.

Scanning tunnelling microscopy (STM) can map the electronic topology of the sample. The STM is the ancestor of all scanning probe microscopes. It was introduced in the early 1980s as the first technique capable of achieving atomic resolution of a surface in real space.[184, 185] For its invention, Gerd Binnig and Heinrich Rohrer were awarded the Nobel Prize in Physics in 1986.[186] A sketch of the set-up is given in **Figure 14**a. An ideally atomically sharp tip is brought close to a (semi-) conductive surface. Typical tip-sample distances are 1 nm or less. At such distances, the electron wave functions of the tip and sample atoms overlap. A bias (V_{tun}) can then be applied between tip and sample to induce a tunnelling current (I_{tun}). The electrons can tunnel from the last atom on the apex of the tip to individual atoms on the sample surface. Therefore, STM can inherently provide atomic resolution of the surface.[187]

In a standard STM set-up, as shown in **Figure 14**a, the movement of the tip is controlled in three dimensions by the use of piezoelectric elements. An electronic controller in a feedback loop provides adjustment of the tip-sample distance to the tunnelling current. A low noise current-to-voltage converter with high amplification is required to record the tunnelling current, which usually lies in the range of nA. For precise measurements, the set-up must be shielded from mechanical vibrations.[187]

With such a set-up, two types of operation modes are possible. In constant current mode, the tunnelling current is maintained constant while the tip scans across the surface. Dependent on the electronic structure of the surface, the tip-sample distance is continuously adjusted to maintain a constant tunnelling current. The corresponding movement of the tip (or, in some set-ups, the movement of the sample) is controlled by the piezoelectric elements. The feedback of the piezoelectric sensors is thus giving rise to a "conductivity" map. In constant height mode, the tunnelling current is recorded at a fixed tip-sample distance. The STM image contains the topologic trace of the surface, which is affected by local variations in the electronic structure.[48]

Atomic force microscopy (AFM) monitors the electrode surface topology and surface forces. A typical set-up is shown in **Figure 14**b. A sharp tip of less than 10 nm diameter in the apex is mounted on the free end of a cantilever of 100 – 500 µm length.[188] The forces between tip and surface cause the tip to move closer or further apart from the surfaces. At distances of 10 nm, those forces are electrostatic and can be either repulsive or attractive. Subsequently, the regime of attractive van der Waals forces holds at a tip-sample spacing of *ca.* 3 nm. Eventually, the forces become repulsive at even smaller distances ("contact mode").[48] The movement of the tip causes the cantilever to bend. The cantilever position is measured by the deflection of a laser beam, which is impinged on the cantilever. Thus, a map of surface topography can be acquired by scanning the tip across the sample. In this work, the AFM experiments were performed in

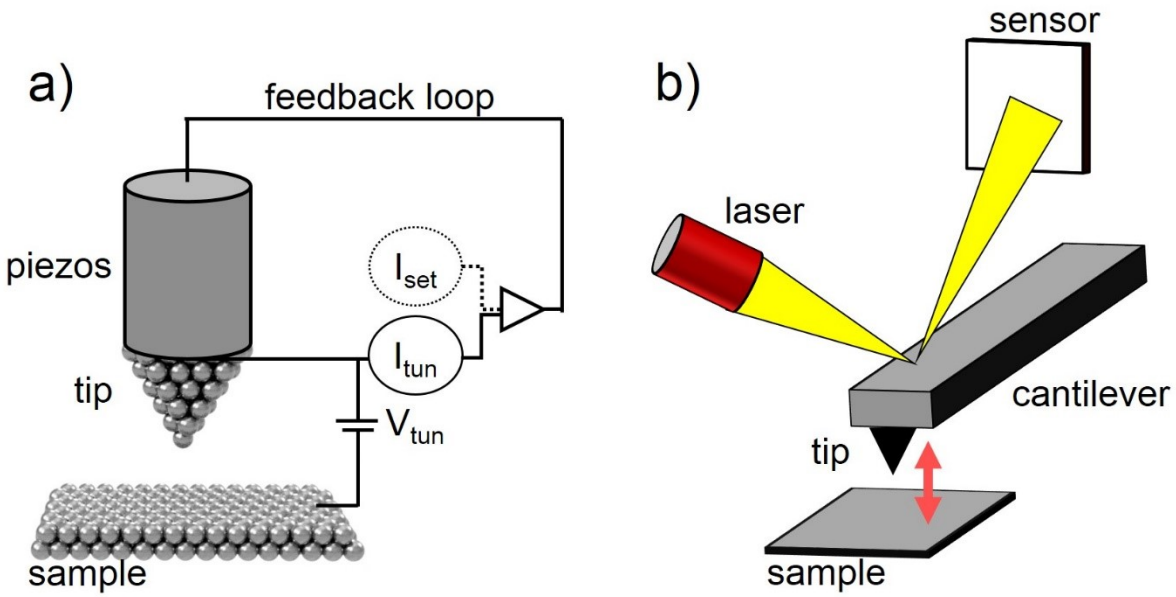

Figure 14 | a) In an STM, a voltage V_{tun} is established between a conductive sample and a sharp tip. The hereby-induced tunnelling current I_{tun} is recorded. The sample-tip distance and the tunnelling current set point are controlled by the piezoelectric sensors and the feedback loop. b) In an AFM, the tip is mounted on a cantilever. Forces lead the tip to approach or repel from the surface. The motions of the tip and cantilever are detected as the deflection of a laser beam.

tapping mode, where the tip is tapping the surface. The image is then determined by deviations from the oscillation set point, which is to be held constant by the feedback system.[188]

In this thesis, the STM and AFM experiments were conducted using a commercial MultiMode EC-STM/EC-AFM scanning probe microscope (Veeco Instruments) connected to a NanoScope III scan feedback controller. STM tips were mechanically ripped from a Pt80Ir20 wire (GoodFellow, Ø = 0.25 mm). AFM tips were commercial n-doped Silicon tips (Bruker RTESP-300). To isolate the set-up from mechanical vibrations, an air table (Newport) and a heavy stone slap were installed. The measurements were recorded with the Nanoscope 5.31r1 software (Veeco Instruments). The data was evaluated with the WSxM 5.0 Develop 9.4 software. [189]

Low-temperature scanning tunnelling microscopy (LT-STM) was performed with a CreaTec instrument under UHV conditions ($p \approx 10^{-10}$ mbar) and at a temperature of 6 K. For tip functionalisation, carbon monoxide (CO) was dosed onto the cold sample and transferred to the tip. The STM images were recorded in constant current mode and subjected to standard corrections such as plane-subtraction and brightness/contrast adjustments.

4.3 X-ray Photoelectron Spectroscopy

XPS is a surface-sensitive tool to identify elements and their oxidation states. Monochromatic X-rays impinge on the surface and eject electrons from the sample. Typically, electrons from the surface until *ca.* 2 nm depth can escape without undergoing inelastic scattering. The initial energy of the X-ray beam $h\nu$ is thus transferred according to

$$h\nu = E_b + E_k + \Phi_{sp}. \qquad \textbf{Eq. 34}$$

The kinetic energy of the electron E_k is detected in the experiment. Each electron had to overcome the binding energy E_b to escape from the atom it was bound to. Besides, the work function of the spectrometer Φ_{sp} has to be taken into account. The type of element present on the sample surface can then be detected according to the binding energy, which can be assigned

to a certain atomic core level of a specific element. Information of the oxidation state is accessible since the binding energy of a given orbital is altered by its electronic surrounding.[48]

In this work, XPS was measured with a SPECS XR50 X-ray source (SPECS GmbH) and a hemispherical energy analyser PHOIBOS 150. The sample was probed by the Al emission line at an energy of 1487 eV. The spectra were fitted using the CasaXPS software.

4.4 X-ray Diffraction

X-ray Diffraction (XRD) experiments can address the degree of crystallinity of a sample. Here, a monochromic X-ray beam impinges on the sample. The X-ray beam is scattered at the crystal planes under specific reflection angles following Bragg's law, which yields a characteristic pattern. With this pattern, crystal orientations can be detected.[48]

In this work, XRD measurements were conducted on an X'Pert PRO (Malvern Panalytical GmbH, Germany) instrument. The samples were impinged with a Ni-filtered Cu K_α radiation (λ = 1.5406 Å) and scanned in 0.78° min^{-1} steps. A scanning region of 10-87° was chosen.

4.5 Low Energy Electron Diffraction

Low Energy Electron Diffraction (LEED) allows for evaluating the unit cell size and its symmetry. In this technique, a single-crystalline sample is bombarded with a collimated beam of monochromatic electrons with energies between 10 and 300 eV in UHV. The electrons impinge on the surface at normal incidence and penetrate only a few monolayers of the sample surface. Therefore, the technique is highly surface-sensitive. The electrons are elastically backscattered from the sample surface and subsequently visualised on a fluorescent screen. Due to the conditions of elastic scattering (Laue condition), the electrons yield a well-defined pattern determined by the periodicity and the symmetry of the sample surface. For example, an *fcc*(111) surface yields a typical LEED pattern with three-fold symmetry.[190]

In this work, a commercial LEED apparatus (SPECTALEED, Omicron Nano Technology GmbH) was employed at a pressure of *ca.* 3 x 10^{-10} mbar.

5 Introduction to Electrochemical Scanning Tunnelling Microscopy for Active Site Identification

A tool, which can map the electrode surface with outstanding resolution and potential control, is the EC-STM. Since the objective of this thesis comprises the application of EC-STM to determine active sites, this chapter is dedicated to its basic functionality and set-up. At first, electron tunnelling in different tunnelling media is addressed. Next, an introduction to monitoring electrocatalytically active areas by a higher noise level of the respective STM signal ("noise" or n-EC-STM) is given. Besides a mere qualitative differentiation of active centres, a measure to quantify the noise level and the local activity is established. Still, EC-STM cannot distinguish chemical species on the surface or access the surface orientation. Therefore, complementary techniques, as introduced in Chapter 4, are necessary.

5.1 EC-STM Working Principle and Set-Up

Shortly after implementing the STM in vacuum[184, 185], its range of application was extended to operate in solutions.[191] Afterwards, the set-up was advanced to be able to work in an electrolyte under potential control.[192] Essentially, the EC-STM technique is the combination of the regular STM set-up (Chapter 4.2) and the three-electrode configuration (Chapter 2.1.3), which results in the four-electrode set-up shown in **Figure 15**a.[193] The sample, which acts as WE, is mounted at the bottom of a small electrochemical cell. The cell contains the electrolyte, and the RE and CE are immersed in the same. As in UHV-STM, the scanning tip is located close to the sample. As in a conventional electrochemical cell, the potential is referred to the RE, whereas the electrochemical currents are grounded *via* the CE. A bipotentiostat is employed to control the potentials of the WE and the tip. The tunnelling current plus disruptive Faradaic currents pass an operational amplifier and into a feedback loop. As in accustomed STM, the feedback loop is connected to the piezoelectric sensors, which adjust the sample-tip distance to

the tunnelling current (or *vice versa*). Since for most applications only the tunnelling current is of interest, electrode reactions occurring on the tip are undesired. Therefore, the tip potential is kept in a regime where electrochemical currents are negligible. In addition, the tip is isolated with wax to suppress Faradaic reactions. Thus, the tunnelling current can serve as the feedback parameter to probe the sample topography.[48, 154, 187, 194]

The EC-STM method was applied in manifold ways in electrocatalysis since it can monitor under reaction conditions and with down to atomic resolution.[195] Moreover, it can detect structural changes induced by the catalytic reaction itself.[196, 197] Furthermore, adsorbates and their movement on the surface can be time-dependently visualised ("video"-STM).[198] In addition to optimising catalytic processes by visualising reaction intermediates, EC-STM can

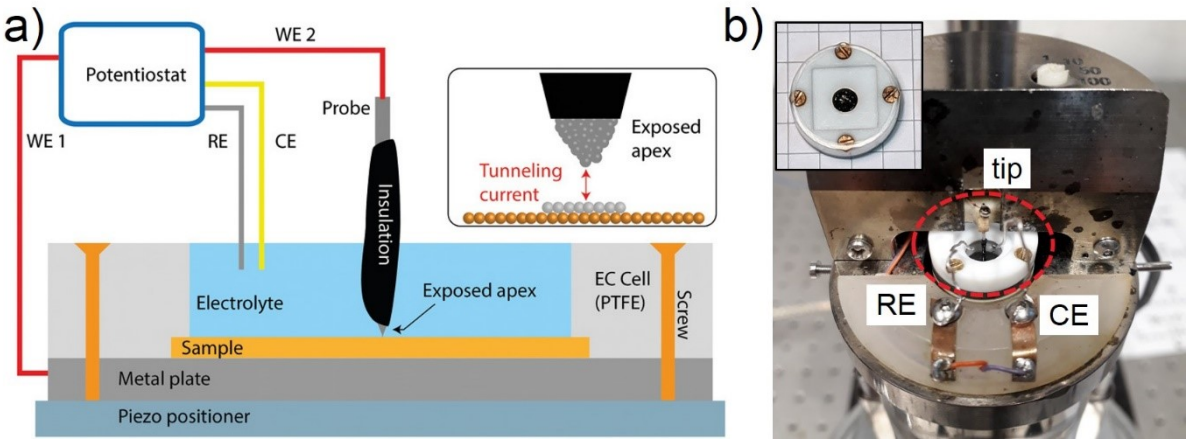

Figure 15 | a) Schematic of the EC-STM set-up. In addition to a conventional STM, a RE, CE and bipotentiostat are needed to control the potentials of both sample and tip. The tip is isolated with wax to prevent the occurrence of Faradaic currents. Reprinted with permission from [193]. Copyright © 2018 WILEY-VCH Verlag GmbH & Co. KGaA. b) Photograph of the set-up used in this work. The sample is mounted between a stainless steel plate and a PTFE ring, as shown in the in-set and brought into proximity to the tip. Finally, RE and CE are immersed in the electrolyte next to the tip. The sample holder is encircled in red, and an enlarged view is given in the inset.

give insights into preventing the adsorption of certain species. A prominent example is the adsorption of CO on Pt, which can act as a poison in fuel cells.[199]

The EC-STM instrument used in this thesis was a commercial MultiMode EC-STM/EC-AFM scanning probe microscope (Veeco Instruments) connected to a NanoScope III scan feedback controller and a Universal Bipotentiostat (Veeco Instruments). A photograph is depicted in **Figure 15**b. The STM tips were mechanically ripped from a Pt80Ir20 wire (GoodFellow, Ø 0.25 mm) and subsequently isolated with Apiezon wax.[200] The sample was clamped between a homemade stainless steel sample holder and a PTFE ring, which exposed a sample area of 0.126 cm^2 for the single crystal samples (*cf.* Chapter 6-8) and 0.28 cm^2 for the carbon sample (*cf.* Chapter 9) to the electrolyte, respectively. The RE and CE were immersed into the electrolyte close to the STM tip. Due to the restricted dimensions of the cell, a conventional RE, *e.g.* as recently reported for EC-STM purposes[201], was infeasible. Instead, a Pt wire was employed as quasi-RE (MaTecK, Ø 0.5 mm, 99.99% purity), which has been established as credible for n-EC-STM measurements.[151, 154, 202, 203] As CE, a second Pt wire (MaTecK, Ø 0.5mm, 99.99% purity) was chosen for the transition metal surfaces (*cf.* Chapter 6-8). For the carbon sample in Chapter 9, a graphite rod (Goodfellow, Ø 0.5 mm, 99.95% purity) was selected to prevent the deposition of foreign active materials. All measurements were conducted at room temperature, and the electrolyte was exposed to air.

5.2 Electron Tunnelling in Different Media

The tunnelling current is not only sensitive to the electronic structure of the surface but also to the tunnelling medium. Therefore, EC-STM can do more than monitoring. The quantum-mechanical phenomenon of electron tunnelling in different media is discussed in this chapter.

Electron Tunnelling in Vacuum. In the first step, the tunnelling medium is the vacuum. A tip material with work function Φ_T is at a distance d from the sample with work function Φ_{WE}. **Figure 16** provides a schematic of the energy changes experienced by an electron moving perpendicular to the sample surface (in z-direction) in the metal/vacuum/metal junction. At equilibrium, the two metals share a common Fermi level. Thus, the vacuum level differs locally,

and an electric field builds up across the tunnelling gap. Thereby, a trapezoidal potential barrier is established across the junction, which depends on both work functions, Φ_{WE} and Φ_T.[204] Since the electronic potential of the gap region is typically much higher than thermal energies at room temperature, electrons from both tip and sample cannot penetrate the barrier in the classical view. However, in the quantum-mechanical view of electrons, described by delocalised wave functions, there is a non-zero probability for electrons to tunnel in the barrier. In an unpolarised sample-tip junction as shown in **Figure 16**a, the net tunnelling current is zero. Instead, a bias voltage V_{tun} needs to be applied to induce electron tunnelling, *e.g.* from the tip to the sample. In this case, depicted in **Figure 16**b, the applied voltage lowers the Fermi level of the sample by eV_{tun}, where e denotes the electron charge. The tunnelling current can be calculated by considering the stationary Schrödinger equations of the sample and the tip as unperturbed

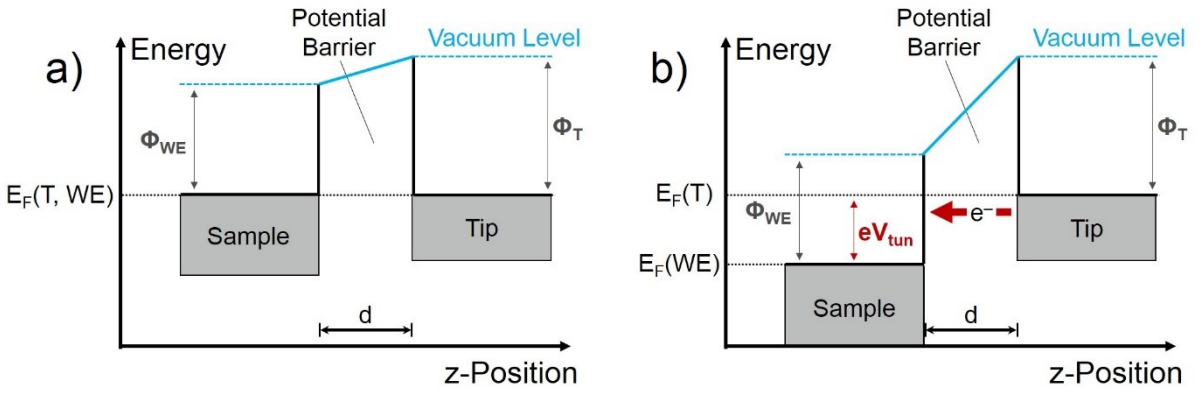

Figure 16 | Diagrams of the electron energy potentials in a metal tip/vacuum/metal sample junction. The z-direction is perpendicular to the sample surface. The tip-sample distance is *d*. The Fermi-Dirac distributions at 0 K are sketched with grey boxes. a) In the equilibrium, the Fermi levels of tip (T) and sample (WE) are aligned. A trapezoidal potential barrier forms across the junction. b) The application of a bias V_{tun} lowers the Fermi level of the sample by eV_{tun} (with elementary charge e). Consequently, electrons tunnel from the tip to the sample indicated by the red arrow. Reproduced with permission from reference [204]. Copyright © 2012 Springer Science+Business Media.

systems. To solve the problem, a plane wave ansatz is taken for the electron wave function. Inside of the barrier, the electron wave function decays exponentially with the wavenumber κ. The tunnelling current can eventually be obtained from the transmission coefficient, *i.e.*, the probability of a particle crossing the barrier. For the explicit calculations, the reader is referred to references [204–207]. The result for the tunnelling current yields

$$I_{tun} \propto \rho_T \, \rho_{WE} \frac{V_{tun}}{d} \exp(-2\kappa d) \qquad \textbf{Eq. 35}$$

with $\kappa = (2\pi/h)\sqrt{2m\Phi_{eff.}}$ [194, 208, 209] Here, ρ_T and ρ_{WE} are the respective surface DOS of the tip and sample, V_{tun} is the bias voltage, d is the tip-sample distance, h is the Planck's constant, m is the electron mass, and Φ_{eff} is the effective potential barrier height. In the vacuum, Φ_{eff} is determined by the work functions of tip and sample.

Several insights can be derived from **Eq. 35**. The tunnelling current relates to the tip-sample distance exponentially. The reason is the overlap between filled and empty states in the tunnelling gap depending mainly on the tails of the respective wave functions of tip and sample. Therefore, if the atom on the apex of the tip sticks out by 1 Å compared to the other tip atoms, it carries 90 % of the tunnelling current. As a result, one can monitor the sample atoms with atomic resolution.[34] Furthermore, the DOS of the sample governs the tunnelling current. Hence, the STM records the surface topology and its electronic structure.

Electron Tunnelling in Solution. The aforementioned considerations relate to electron tunnelling across a vacuum gap. If the tunnelling gap is filled with a liquid such as an aqueous electrolyte, the respective tunnelling current depends on the tunnelling medium. Most conveniently, changes, which arise because of the presence and properties of the electrolyte, can be summarised in the effective tunnelling barrier Φ_{eff}. This value can be accessed experimentally from distance tunnelling spectroscopy. Hereby, the tunnelling current is measured with varying sample-tip distance but at fixed tip and sample potentials. The effective tunnelling barrier Φ_{eff} can then be extracted from the slope of the logarithmic current *versus* the tip-sample distance (*cf.* **Eq. 35**).[194, 208–210] In such measurements, Φ_{eff} ranges in 4-5 eV in the

vacuum.[211] In aqueous solutions, those values drop to around 1-2 eV.[194, 208, 210, 212, 213] In a first approximation, the liquid tunnelling medium can be modelled as a dielectric continuum. The interactions of the electron states at the metal surface with the tunnelling medium (*e.g.*, water) lower the Φ_{eff} values for water-filled tunnelling junctions compared to UHV-STM.[213]

As stated above, assuming the liquid tunnelling medium as a dielectric continuum can explain its lower effective tunnelling barrier. However, it turned out that the tunnelling current deviates from a strictly exponential behaviour due to the structure of the (water) molecules in the tunnelling gap. In detail, if an exponential fit is subtracted from the current-*versus*-gap-width data, an oscillating signal remains. The period of that signal matches the distance between the water molecules in the Helmholtz layer of the electrified solid-liquid interface.[208, 209, 214] Thus, the structure of the molecules in the tunnelling gap affects electron tunnelling.[215, 216] In such a tunnelling medium, charge transport can be mediated *via* hydrogen bonding networks. Well-ordered water dipoles at the two metal/electrolyte interfaces can be polarised upon applying a bias.[194] Therefore, also the polarizability of the solvent can influence the tunnelling.[216] Apart from a well-structured water layer, also irregularities can enhance the tunnelling current. Based on a numerical model, concavities in the water structure were proposed to support electron trap states. Those can provide resonances with a short lifetime (*ca.* 10 fs), lowering the effective tunnelling barrier.[217] Thus, the properties of the liquid tunnelling medium, such as its structure and polarizability, impact the overall tunnelling barrier and consequently the tunnelling current.

In addition, the presence of localised charges like solvent molecules is a factor in EC-STM. It has been suggested that ions near the electrified solid-liquid interface modify the tunnelling current.[215, 216, 218, 219] Besides, Φ_{eff} was found to depend on the charge density distribution in the tunnelling gap. The corresponding experiment was conducted in an H_2SO_4 electrolyte and Φ_{eff} was stated to be affected by the charge density distribution of the constituent sulphur and oxygen ions, as well as the hydronium ions of the electrolyte.[212]

All the above-mentioned considerations show that the tunnelling current is indeed governed by the structure and composition of the electrolyte present in the tunnelling gap. This circumstance

is the basis of using fluctuations in the tunnelling current to monitor changes *in situ* and with high spatial resolution.

5.3 Identifying Active Sites *via* Noise Analysis of the STM Signal

The dependence of the tunnelling current on the tunnelling medium, as introduced in the last chapter, opens up new pathways beyond common monitoring. An example of such a possibility is to detect electrocatalytically active sites with high resolution, which is the aim of n-EC-STM. In this work, the technique was applied to several model catalysts for the ORR and the OER.

The idea to use features in the tunnelling current to deduce events at the electrified solid-liquid interface is not new. In 1986, Binnig *et al.* announced the possibility of monitoring the dynamic behaviour of oxygen atoms migrating on Ni surfaces in UHV-STM. The authors report spikes in the transient current, and ascribed them to "single diffusing oxygen atoms crossing the tunnelling region". Moreover, the current pulses were locally confined to the adsorption site of the oxygen atoms on the Ni surface.[220] Subsequent STM studies confirmed the occurrence of characteristic noise in the tunnelling current, which was related to the movements of the adsorbates on the sample surface.[221–223]

The objective of the n-EC-STM method is to elucidate the nature of electrocatalytically active sites under reaction conditions and at an applied potential. The sample potential can be controlled to enable ("on") or disable ("off") the reaction of interest. For reaction "off", as shown in **Figure 17**a, the electronically modulated topology of the sample is mapped. The noise level of the STM signal is low, despite some unavoidable thermal or shot noise. Switching the reaction "on" leads to an increase in the noise level, which is particularly distinct at the position of the active sites. In the sketch in **Figure 17**b, the atoms near the top of the step edge (coloured in green) are exemplarily assigned as "active". As depicted in the inset, the line scan shows noise features (spikes) at the active centres if the reaction is switched "on". Said locally confined noise serves as means for the identification of active sites. The origin of the noise under reaction conditions can be traced back to the sensitivity of the tunnelling current on the composition of the tunnelling barrier (*cf.* Chapter 5.2).

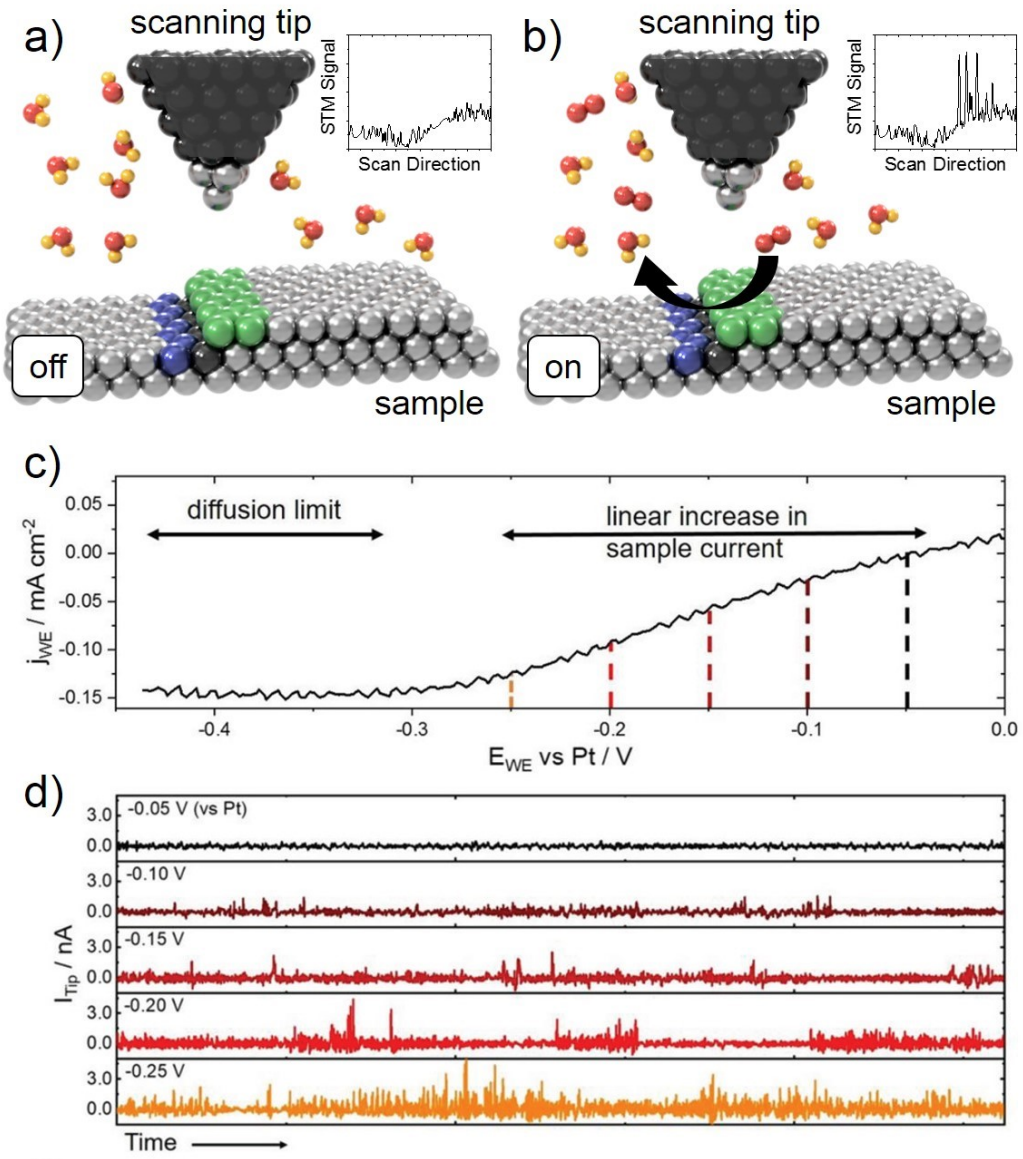

Figure 17 | Principle of n-EC-STM. Altering the sample potential can a) inhibit "off" or b) initiate "on" the reaction. For reaction "on", the STM signal exposes a high noise level at active sites. In the example, sites near the top of the step (coloured in green) are "active". Therefore, pronounced spikes are locally confined to the active sites in the line scan (inset). Colour code: Terrace sites (silver), sites of higher/lower coordination (blue/green), sterically hindered sites (black), oxygen atoms (red) and hydrogen atoms (yellow). c) CV of a Pt(111) surface in air-exposed 0.1 M $HClO_4$, recorded in the EC-STM set-up against a Pt quasi-RE. d) Corresponding EC-STM measurement at a (111) terrace site on Pt(111) in 0.1 M $HClO_4$. At more negative potentials and thus at higher ORR reaction rates, the noise level in the tunnelling current increases. Images c,d) reprinted with permission from reference [54].

Since an ongoing reaction continuously changes the composition and structure of the electrolyte, continuous changes in the tunnelling barrier and thus the tunnelling current can be explained.

More insights on the n-EC-STM technique are given by taking the example of the ORR on Pt(111) in 0.1 M $HClO_4$. Details of this system are specified in Chapter 3.4.1. In the past, the ORR active sites could be predicted with the help of a geometric descriptor to be located near the bottom of step edges.[31, 76] Such spots of higher coordination are marked in blue in **Figure 17**ab. Atoms at the very bottom of the step edge (coloured in black) are unlikely to contribute to the reaction due to steric hindrance.[76] It was confirmed by n-EC-STM that the active sites are indeed near step sites, as is outlined in the following.[54, 151]

In the first step of the experiment, the STM tip was fixed over a Pt(111) terrace site in a constant tip-sample distance. While recording, the sample potential was stepwise decreased. As can be seen from the CV in **Figure 17**c, the ORR current increases the lower the potential value recorded *versus* a Pt quasi-reference. At a potential of 0 V_{Pt}, no reaction takes place. In the EC-STM measurement in **Figure 17**d, the tunnelling current is comparatively stable for reaction "off" (black lines at 0 V_{Pt}). At more negative potentials, the tunnelling current exhibits an increased noise level, which leads to a higher number of spikes in the tunnelling current. The trend of an elevated noise level at higher reaction rates is in line with the above-explained principle of n-EC-STM.

In the next step, n-EC-STM was used to elucidate the nature of the ORR active sites on Pt(111) by enabling the tip to scan across the surface. In **Figure 18**a, n-EC-STM measurements in the constant current mode are shown, which include a step edge. For every applied potential under the ORR conditions, the noise level of the STM signal was higher at the step edge than at the adjacent terrace sites. Therefore, the active sites were assigned to be near step edges. This example confirms that n-EC-STM can identify the geometry of active sites.

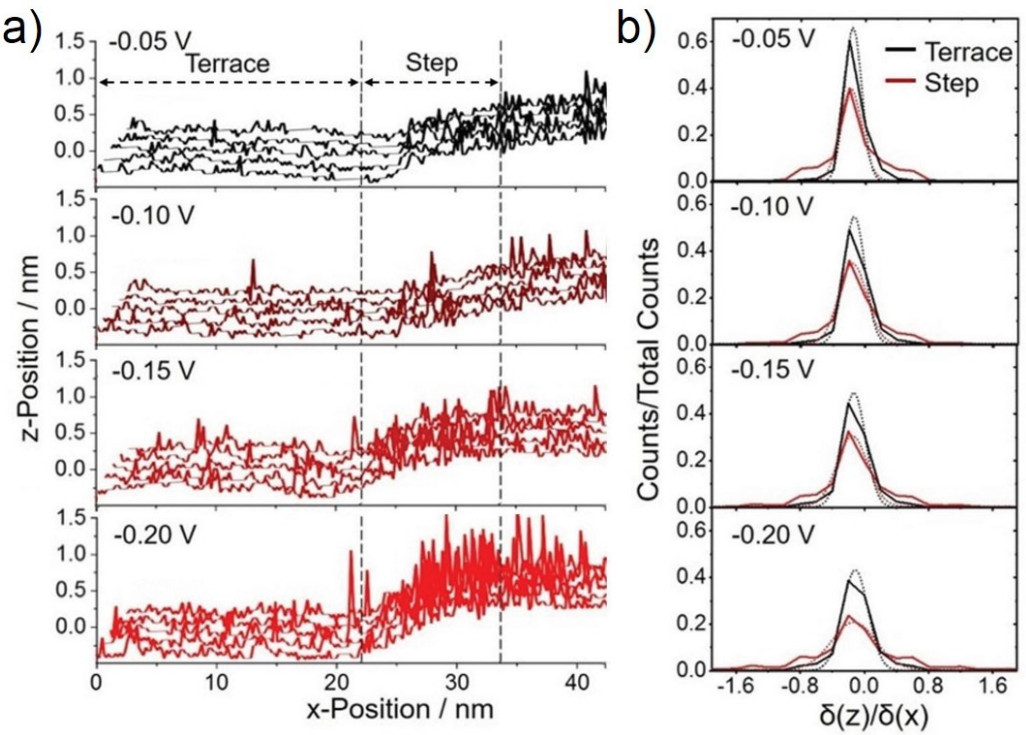

Figure 18 | n-EC-STM on Pt(111) in 0.1 M $HClO_4$. a) Line scans across a step edge recorded at different potentials. For more negative potentials, the ORR current is higher, and the noise level of the STM signal is more pronounced. The most distinct spikes are located near the step edge, where the active sites can be pinpointed. b) Noise level quantification for terrace (black) and step sites (red). The histograms of the height derivatives were fitted with Gaussian curves (grey dotted lines); see text for details. The FWHM and height of the fit measured the noise level. Broad and low-intensity histograms indicate a high noise level and *vice versa*. Image reprinted with permission from reference [54]. © 2020 The Authors. Published by Wiley-VCH GmbH.

5.4 Quantification of the Noise Level and Local Reactivity

Before, n-EC-STM was introduced to monitor the active sites qualitatively. Beyond that, a quantitative approach to assess the local reactivity from the noise level was explained in reference [54]. The procedure was reported for the ORR on Pt(111) in 0.1 M $HClO_4$. The result is given in **Figure 18**. In the first step, the data was divided among the surface structures, which should be compared, *e.g.* terrace and step sites. Per each data set, the STM signal (tunnelling current or height) was derived with respect to adjacent data points, according to

$$\left(\frac{\delta z}{\delta x}\right)_{x_1} = \frac{1}{2}\left(\frac{z_2 - z_1}{x_2 - x_1} + \frac{z_1 - z_0}{x_1 - x_0}\right) \qquad \textbf{Eq. 36}$$

where (x_0,z_0), (x_1,z_1) and (x_2,z_2) are three successive data points. The signal derivative at a certain data point is equal to the slope of the line scan at the said position.

In the next step, histograms were compiled from the signal derivatives. To compare data sets of unequal sizes, each histogram was divided by the number of data points to "normalised counts". The histograms were fitted by Gaussian curves, and the full width at half maximum (FWHM) and the height of the Gaussian fit served as quantitative descriptors of the noise level. If there are spikes present in the scan, a large number of different slopes arises. Consequently, for an elevated noise level in the STM signal, the derivatives are scattered widely around zero. The corresponding histogram is broad and of lower intensity. Indeed, in **Figure 18**, the histograms broadened and the intensity decreased with more negative potentials. With increasing reaction rate (more negative potential *versus* Pt), the ORR reaction rate increased and so did the noise level of both terrace and step sites. Besides, step sites are more active than terrace sites, which is in line with the previous observations.

In addition, this quantification process can be extended to obtain the local reactivity from the local noise level. As a measure of activity, the TOF was chosen, which is introduced in Chapter 2.1.4. To give an example of local activity, the step and terrace sites in **Figure 18** were

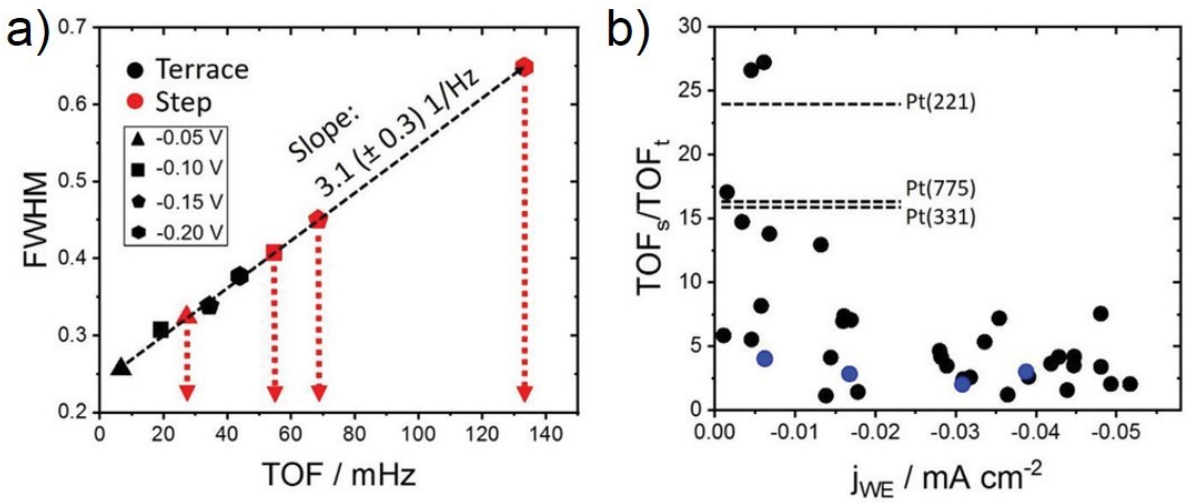

Figure 19 | Quantification of the local reactivity on Pt(111) electrodes in 0.1 M $HClO_4$. a) The TOF of the terrace and step sites were plotted *versus* the FWHM values from **Figure 18**b. Herein, the TOF of the terrace sites (TOF_t) were obtained from the overall sample current, whereas the TOF of the step sites (TOF_s) were extrapolated from the linear relation between TOF_t and the FWHM. b) Enhancement factors (TOF_s/TOF_t) from a variety of measurements. The data of a) is coloured in blue. The comparison to RDE measurements on stepped single crystals is possible at the low sample currents. As indicated in the graph, the step sites of the highest activity were ascribed to structural motives on Pt(221), (775) and (331), respectively. Image reprinted with permission from reference [54]. © 2020 The Authors. Published by Wiley-VCH GmbH.

compared to each other. The TOF of the terrace sites (TOF_t) was approximated by the TOF of the whole sample. Since the sample preparation method should yield a low number of steps,[224] the assumption that terrace sites mainly govern the overall sample current is justified. The TOF_t was calculated according to **Eq. 14** (Chapter 2.1.4) with $\alpha = 60°$ for an *fcc* surface, n = 4 for the ORR, and a lattice constant d = 2.77 Å for Pt(111).[225] Subsequently, the values were plotted against the respective FWHM extracted from the Gaussian fits of the histograms (**Figure 18**b). As can be seen in **Figure 19**a, the curve yielded a linear trend for the terraces (black symbols). In turn, the linear fit of the terrace data (black curve) can serve as a calibration to acquire the

local activity of the adjacent step sites. Therefore, the TOF of the step sites (TOF_s) can be read off by knowing the corresponding FWHM from the histograms (**Figure 18**b). In the last step, the local activities of step and terrace sites were compared *via* enhancement factors, which were defined as TOF_s/TOF_t. To account for the statistics, the procedure was repeated and yielded **Figure 19**b. The blue symbols belong to the data in **Figure 18** and **Figure 19**a. For a profound comparison to literature data from RDE measurements, lower sample activities have to be considered. In this range, the step sites reach a proportionally higher reaction rate than terrace sites. A spread in enhancement factors can be observed, which was ascribed to the spread in activities of different crystal facets as experiments on stepped Pt single crystals revealed (*cf.* **Figure 12**a in Chapter 3.4.1). Accordingly, the maximal enhancement factor of *ca.* 27 in the n-EC-STM study was attributed to the most active concave sites on Pt(221). Lower enhancement factors were with decreasing magnitude attributed to the Pt(221), the (775), the (331) facets, and other high-index planes, respectively.[54] Thus, the enhancement factors were in good agreement with previous studies. This approach confirmed the potential of the n-EC-STM method to provide access to activity with a high spatial resolution.

After having established the functionality of the n-EC-STM technique, the next chapters proceed with its application to model systems for the OER and ORR.

6 Assessment of Active Areas on Iridium Oxide for the Oxygen Evolution Reaction

"Green" production of hydrogen in PEM electrolysers still suffers from the low kinetics of the complex multistep reaction at the anode, the OER. Thus, a need for suitable and high-performing OER catalysts arises to reduce the required overpotentials. Today, IrO_x catalysts offer the best compromise between good stability and activity in acidic media. Under "real" operation conditions, IrO_x becomes amorphous. The formation of an amorphous and hydrated oxide surface was even reported to be beneficial for the OER activity compared to its rutile counterparts.[112-117] Still, the structure-activity relations for this material class remain largely unknown, and the reaction mechanism is under debate (see Chapter 3.3). For amorphous surfaces, Ir vacancies can "hole-dope" neighbouring oxygen atoms to a formal state of O^{-I} and turn adjacent Ir atoms into Ir^{III}. A combination of O^{-I} and Ir^{III} species was proposed as active centres.[123-125] While there are multiple studies of the reaction mechanism, less is known on the structure of the active sites. Therefore, n-EC-STM is applied to amorphous IrO_x for the OER. Further information, including additional n-EC-STM measurements, can be found in reference [226].

In this study, IrO_x was formed during electrochemical cycling of an annealed Ir(111) single crystal (Ø 5mm, MaTecK). Before each experiment, the crystal was annealed in an H_2/Ar atmosphere (Varigon® H5, Linde) at 1100 °C for *ca.* 10 min and then slowly cooled down to room temperature. After annealing, the crystal was cycled in 0.1 M $HClO_4$ for approximately 80 cycles between potentials of 0.05 and 1.5 V_{RHE}. Details on the experimental techniques and the equipment are included in Chapter 4.

Figure 20a shows a typical CV. At *ca.* 0.2 V_{RHE} and lower, the underpotential deposition of hydrogen and the onset of the HER can be observed. At the potentials more positive than the

double layer region, a pronounced pair of redox peaks appear at *ca.* 0.9 V_{RHE}, which can be ascribed to an Ir^{III}-Ir^{IV} transition.[227-230] Additionally, a shoulder in the reduction part of the curve at *ca.* 1.35 V_{RHE} can correlate to an Ir^{IV}-Ir^{V} transition.[229, 231] Alternatively, that shoulder can be interpreted as the oxidation of O^{-II} to O^{-I}, in the context of the model explained in the introduction of this chapter.[123-125] In **Figure 20**b, an RDE measurement of the IrO_x surface is presented. Here, an MMS RE was employed, and the potential was recalculated to RHE scale

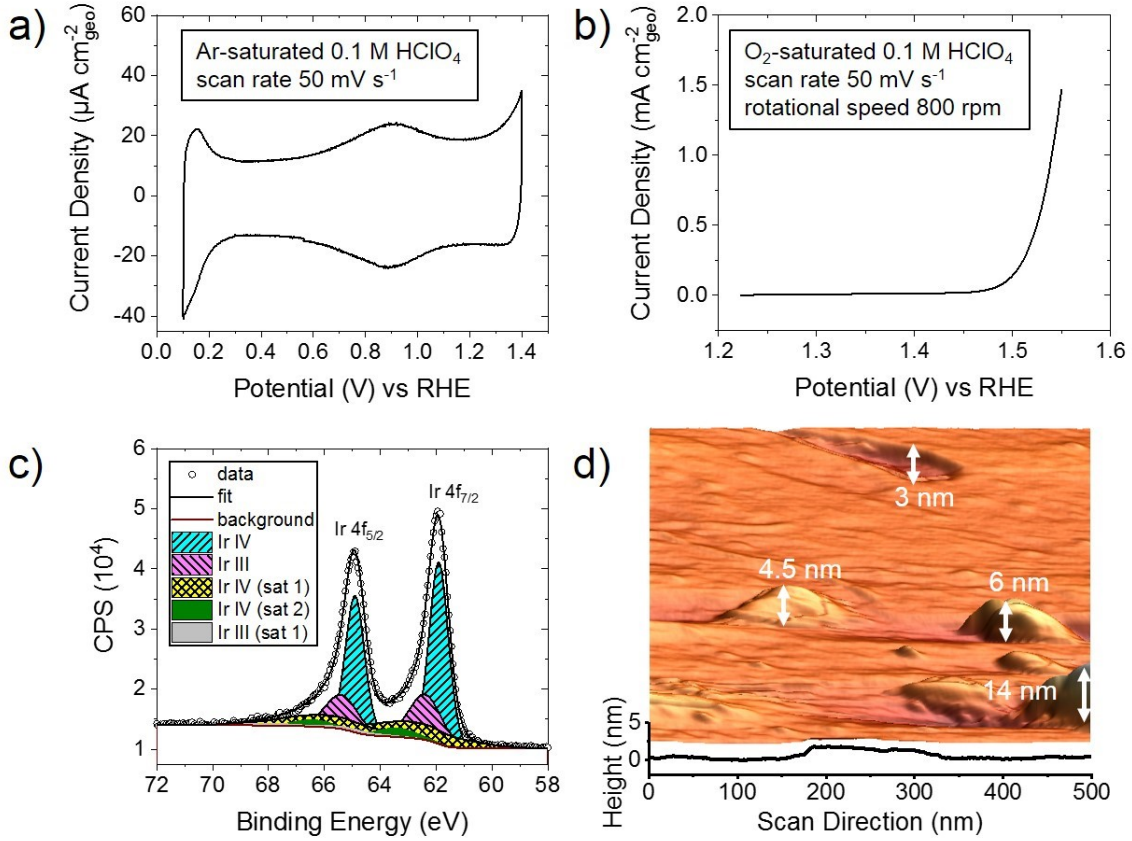

Figure 20 | Electrochemical and compositional characterization of amorphous IrO_x. a) CV in Ar-saturated 0.1 M $HClO_4$ at a rate of 50 mV s^{-1}. b) RDE recorded at 50 mV s^{-1} scan rate and 800 rpm rotational speed in O_2-saturation; iR corrected. c) XPS of the 4f Ir peak. The fitting procedure is explained in the main text. d) AFM image of the mainly flat Ir oxide surface. The heights of some features are given and the line scan was performed along the lower edge. Data published in reference [226].

via $U_{RHE} = U_{MMS} + 0.72$ V. At 1.51 V_{RHE}, the geometric current density is 0.23 mA cm^{-2}, which is comparable to literature reports.[126, 232]

To assess the crystallinity and the chemical composition of the sample, LEED and XPS were employed. The LEED measurement (not shown) yielded no periodic pattern, which indicates an amorphous surface. Therefore, the amorphous layer may be several atomic layers thick, which would be larger than the penetration depth of the beam. The XPS data of the Ir 4f peak is supplied in **Figure 20**c. A Shirley background was subtracted from the data. The binding energy was aligned by adjusting the C-C bond to 284.8 eV. The C 1s XPS data is included in reference [226]. For the fit of the Ir 4f doublet, the two peaks were restrained to the same FWHM, a distance of 3.0 eV in binding energy and an area ratio of 4 to 3 for the Ir $4f_{7/2}$ to $4f_{5/2}$. The positions of the satellite peaks were set in 1 eV and 3 eV distance to the main peak according to reference [233]. Two Ir species can be identified at 65.5 eV and 62.5 eV binding energy, which can be assigned to Ir^{IV} and Ir^{III}. Due to the ambiguity in the literature regarding the oxidation state of the active species, the species at 62.5 eV can also be Ir^{V}. Since, however, Ir^{V} species are unlikely to exist *ex situ*[124, 234], the peaks in **Figure 20**c were labelled with Ir^{III}. Irrespective of their true oxidation state, these species have been reported as the active kind.[123-126, 234] From the XPS spectrum, a ratio of 0.4 for Ir^{III} to Ir^{IV} species can be extracted. It is thus evident that the IrO_x sample comprises a considerable share of active species. In addition, the surface morphology was probed with AFM, as shown in **Figure 20**d. The surface was mainly flat, with a root-mean-square roughness of 1.3 ± 0.5.

After the confirmation of an amorphous and active IrOx sample, n-EC-STM was applied to elucidate the structure of the active sites. The functionality of the technique is explained in Chapter 5. At first, CVs were recorded in the EC-STM set-up to determine the potentials for reaction "on" and "off". A typical CV is shown in **Figure 21**. A potential of 350 mV_{Pt} was used for reaction "off", a potential of 500 mV_{Pt} or higher for "on". Higher potentials were avoided not to roughen the surface. Besides, the evolution of oxygen bubbles would retract the tip from the sample such that it cannot scan any further. The experimental parameters are given in **Table 1**.

In **Figure 22**, a typical n-EC-STM measurement of the amorphous IrO_x surface is given. The monitored area contains monoatomic step edges. During the capture of the image, the sample potential was altered from reaction "on" to "off". For reaction "on", the STM signal is modulated with noise, which appears as white dots in the image. For the reaction "off", the signal is stable, and a sharp image is obtained. The occurrence of the noise under reaction conditions is expected from the functioning of the technique. Therefore, n-EC-STM was successfully applied to the OER for the first time.

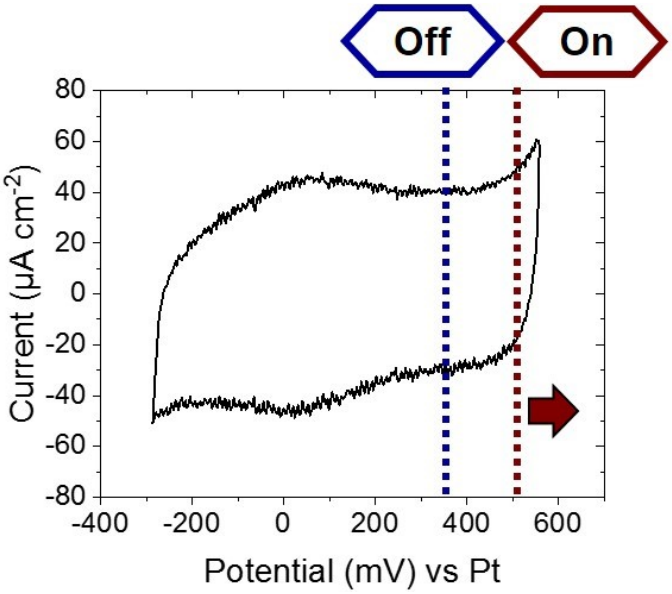

Figure 21 | CV recorded in the EC-STM set-up. A sample potential of 350 mV_{Pt} was assigned to reaction "off". The potentials for reaction "on" are given in **Table 1**.

Table 1 | Experimental parameters of the n-EC-STM measurements in **Figure 22** and **Figure 23**.

	Sample Potential "on" (mV_{Pt})	**Current Setpoint (nA)**	**Tip Potential (mV_{Pt})**
Figure 22	600	4	250
Figure 23	500	3	150

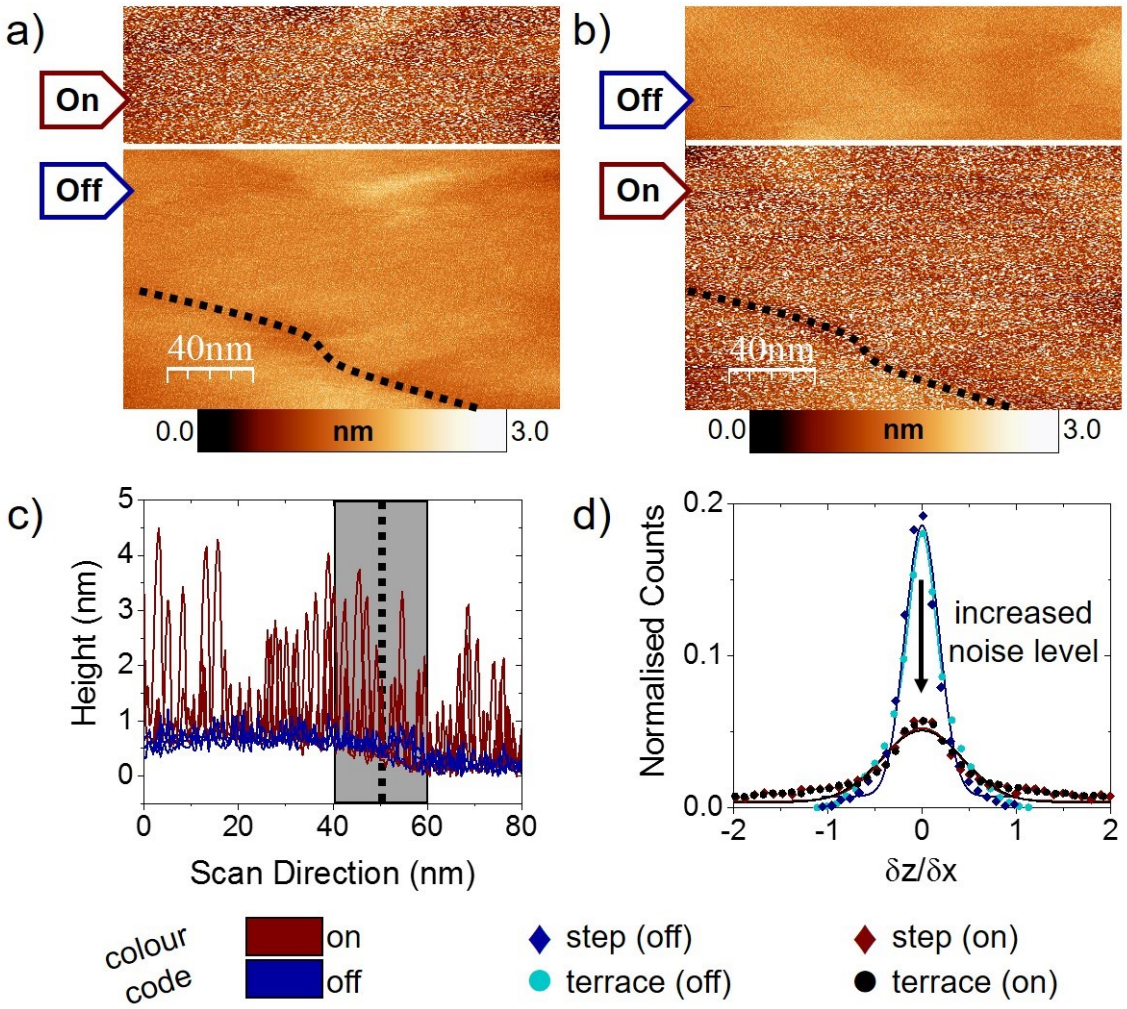

Figure 22 | n-EC-STM measurement on amorphous IrO_x in 0.1 M $HClO_4$ for the OER. a) EC-STM measurement of a mono-atomic step edge (dotted line). During recording, the sample potential was altered from "on" to "off". For reaction "on", the STM signal exhibits a considerable increase in the noise level (spots of high intensity that correspond to a white colour in the colour code). b) The same area of the sample was captured again, but inverting reaction "on" and "off" for a direct comparison. c) Multiple line scans stacked on top of each other for reaction "off" (blue) and "on" (brown). The position of the step edge is marked with a dotted line. d) Corresponding histograms. The data set taken for the step edge is encircled by a grey box in c). A high noise level results in a large FWHM and a small height of the Gaussian, and *vice versa*. Comparing terrace and step sites under reaction conditions, they show a similar noise level and thus activity. Data published in reference [226].

In **Figure 22**b, the image of the same area was re-recorded with the reaction "on" and "off" inverted. The two images can directly be compared to each other. By eye, it can be assumed that the noise level increase is homogeneously distributed across the surface irrespective of the type of site. To compare terrace and step sites in more detail, the step edge marked in **Figure 22**a,b is evaluated. **Figure 22**c shows multiple line scans (height profile in scan direction) layered on top of each other. A dotted line marks the position of the step edge. Again, the noise levels of step and terrace sites seem similar.

Next, step and terrace sites were quantitatively compared. The respective processing of the data is given in Chapter 5.4. A grey box encircles the data set for step sites in **Figure 22**c. The STM signal was derived with respect to adjacent data points ($\delta z/\delta x$). **Figure 22**d includes the histograms for step and terrace sites. They were fitted with Gaussian curves, and their FWHM and height quantify the noise level of the respective surface site. The correlation can be illustrated as follows: At low noise levels, there is a low amount of distortion to the signal, and hence, the corresponding histogram of the change in recorded signal shows a narrow distribution. Vice versa, at high noise levels, the signal experiences many fluctuations, which results in a broad histogram. As expected for reaction "off", in **Figure 22**d, the histograms yield a narrow and high-intensity line since the noise level is low. Moreover, the step and terrace sites have equal histograms as the STM signal is equally stable across the whole surface. For reaction "on", the histograms are broader and of lower intensity which is equivalent to a higher noise level. The histograms for step and terrace sites are congruent, which means that they show comparable noise levels and thus OER activities.

From the measurements and the quantification, step and terrace sites on the amorphous IrO_x show comparable activities. To account for the statistics, additional n-EC-STM images are given in **Figure 23**. In **Figure 23**a, a terrace framed by two step edges was recorded. The sample potential was altered multiple times between reaction "on" and "off" as labelled in the image. The step edge marked with a dotted line in **Figure 23**a was examined more closely. In **Figure 23**b, multiple line scans across the same are layered on top of each other. The noise levels of step and terrace sites seem to be similar. This impression is confirmed by the matching

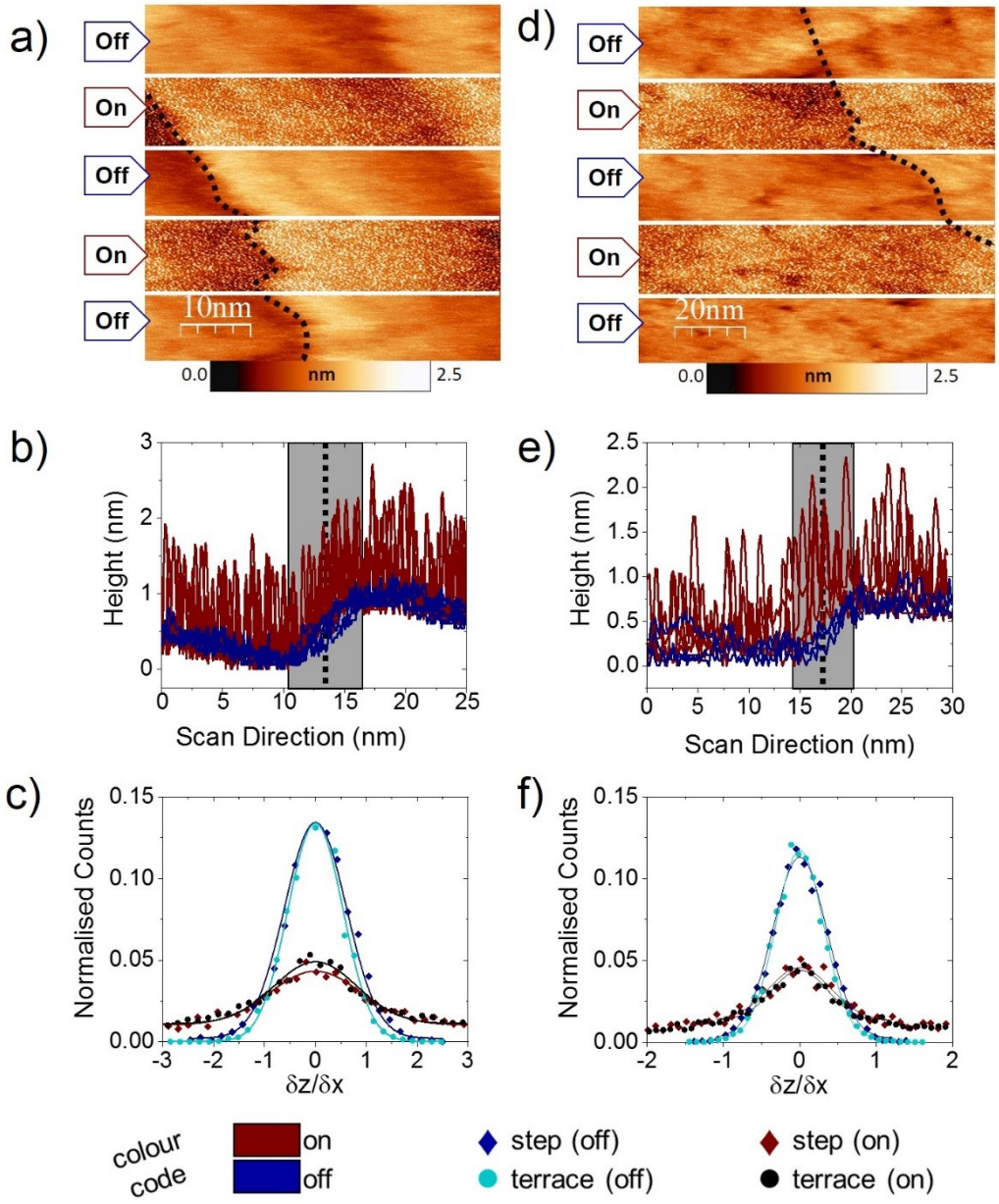

Figure 23 | n-EC-STM measurements on amorphous IrO_x to compare the local noise level of terrace and step sites. a) A terrace framed by two step edges, the left one marked by a dotted line. The sample potential was altered multiple times between "off" and "on" during recording. The noise in the STM signal under reaction "on" conditions seems comparable between the terrace and step sites. b) Multiple line scans (height profile in scan direction) stacked on top of each other, performed across the left step edge. The position of the step edge is marked with a dotted line. c) Corresponding histograms for step and terrace sites. The data assigned to the step sites are tagged in b with a grey box. d) Analogous n-EC-STM experiment with corresponding e) line scans and f) histograms. In both measurements, step and terrace sites show similar noise levels. Data published in reference [226]. Copyright © 2021 Elsevier Inc.

histograms of step and terrace sites shown in **Figure 23**c. An analogous n-EC-STM measurement is presented in **Figure 23**d. Noteworthy, the terraces on either side of the step edge (dotted line) show some minor concavities. Still, the terrace exhibits a homogeneous noise level for the OER "on". Again, from the image and the line scans in **Figure 23**e, the noise at the step and terrace sites seems commensurate. This is proven by the equal histograms shown in **Figure 23**f.

To sum up the findings from the n-EC-STM experiments, surface sites on amorphous IrO_x show similar activities independent of their "coordination". In other words, the OER on amorphous IrO_x surfaces is likely not sensitive to the structure. The outcome of this study is in good agreement with previous literature reports. Maillard *et al.* synthesised and investigated Ir oxide surfaces of different initial morphologies. The authors report that during electrochemical cycling, the initially different morphologies all diverged into the same surface state.[126] Also in line with this study is the observation that Ir(111) and Ir(110) surfaces approach the same OER activity with increasing cycling number.[235] The reason for the surface insensitivity of the OER on an amorphous IrO_x surface is purely speculative. Ir vacancies introduce OER active species in the material according to the model mentioned in the introduction.[123–125] Presumably, such vacancies can occur independently of the site geometry on an amorphous surface. In line with this assumption would be the findings of this study, namely, that all surface sites contribute equally to the activity. Extending the observations of a structure-insensitive OER on amorphous IrO_x to nanostructured electrocatalysts, one can assume that the shape of such nanoparticles should not affect the OER activity. Such nanoparticles with an amorphous IrO_x shell on an IrNi core have been synthesised by Strasser *et al.*[236] They also give interesting insights into the "morphology" of the amorphous IrO_x shell. Still, these observations only hold for amorphous IrO_x in an acidic medium. In general, the nature of active sites depends on crystallinity and the electrolyte composition. As an example, for rutile IrO_2 in an alkaline medium, the orientation of the surface plays a significant role in the OER activity.[237]

In summary, the observations on an amorphous extended IrO_x surface in 0.1 M $HClO_4$ suggest that all surface sites contribute equally to the overall activity. The OER is not structure-sensitive

here. Extending this behaviour to nanoparticulate electrocatalysts, one can assume that their activity is independent of their shapes and sizes. This model study shows that after the successful application of n-EC-STM to HER and ORR in the past[151, 154, 202, 203], the technique is equally valuable to identify active sites for the OER.

7 Identification of Active Centres on Pt-Lanthanide Alloys for the Oxygen Reduction Reaction

The application of hydrogen as the fuel in zero-emission PEMFCs is desirable due to low operational temperatures, advanced power densities, and short start-up times.[238-240] However, the cathode reaction, the ORR, remains its pivotal element due to relatively slow reaction kinetics. Up to date, ORR catalysts with the highest performances and stability are based on Pt.[241] However, pure Pt surfaces, such as Pt(111), were shown to bind the key intermediates stronger than optimal.[65, 132, 152] A well-known approach to diminish the binding strength and thus increase the ORR activity is to use Pt alloys. An interesting class of alloying partners are rare-earth metals. Because of their negative heat of formation compared to other transition metals, they have been assumed as potentially more stable.[158, 161, 242] Further information on Pt-alloys as ORR catalysts is provided in Chapter 3.4.2.

Encouraged by their previously reported, high ORR performances, polycrystalline Pt-praseodymium (Pr)[157, 243] and Pt-gadolinium (Gd)[155, 158, 178, 244-246] alloy surfaces were investigated. When operating such an alloy electrode under ORR conditions, the rare-earth metal dissolves from the surface.[247-249] The electrode stabilises by the formation of an overlayer consisting solely of Pt.[25] Since the Pt overlayer is composed of several monolayers[158, 250], ligand effects could be ruled out because of a shorter range of these effects[176, 177]. Instead, for such surfaces, strain effects play a major role.[143] The introduction of lanthanide atoms with larger radii compared to Pt causes a lattice mismatch between the alloy bulk and the Pt overlayer. Therefore, the compressive strain on the surface leads to a weakening of the binding strength toward the ORR intermediates and consequently to superior ORR activities. As shown in **Figure 12**b (Chapter 3.4.2), a volcano plot using the radii of the solute elements as the descriptor, these weakened interactions even lead to a less-than-optimal binding energy, and thus the Pt-lanthanides are located on the weaker binding site of the volcano plot.

This effect is more pronounced for the Pt_5Pr surface, whereas Pt_5Gd remains close to the optimum.

Albeit strain effects are likely to be the origin of the improved catalytic performance,[143] little is reported on the geometry or coordination of the active sites. Therefore, n-EC-STM was applied to polycrystalline Pt_5Pr and Pt_5Gd alloy surfaces (both Ø 5 mm, MaTecK). Specifics of the characterisation methods are given in Chapter 4. Details on the instrumentation and working principle of the n-EC-STM technique are provided in Chapter 5.

At first, the surfaces were characterised using electrochemical and spectroscopy measurements. The experiments were executed in both acidic (0.1 M $HClO_4$) and alkaline (0.1 M KOH) media. **Figure A1** (Appendix Chapter 12) displays CV measurements for the four systems. In addition, the ORR activity was probed in an RDE set-up. The corresponding polarisation curves are presented in **Figure 24**ab. The following trend can be extracted from the kinetic current densities (*cf.* **Eq. 33**), included in the insets of **Figure 24**ab, at a potential of 0.9 V_{RHE}: $Pt_5Gd_{HClO4} > Pt_5Pr_{HClO4} > Pt_{KOH} > Pt_{HClO4} > Pt_5Pr_{KOH} > Pt_5Gd_{KOH}$. The index is referring to the respective electrolyte being 0.1 M $HClO_4$ or 0.1 M KOH. Noteworthy, pure Pt performs better in alkaline than acidic medium, whereas the Pt-lanthanide alloys operate better in acidic than in alkaline medium. In addition, XPS measurements were accomplished to assess the composition of the samples, as given in **Figure 24**cd. Each XPS spectrum was fitted using the commercial CasaXPS software and a Shirley background. The fits lead to a share of 3.2 at% of Pr and ~ 0 at% of Gd, respectively. Hence, de-alloyed surfaces can be observed after the electrochemical measurements, which are in line with expectations from the literature.[170] Moreover, XRD experiments were carried out to elucidate the polycrystalline nature of the surfaces, which are shown in **Figure A2**.[243]

After the application of complementary techniques to assess the surface electrochemical behaviour, composition and crystallinity, n-EC-STM was employed for the identification of the ORR active sites. CVs were recorded in the EC-STM set-up to determine the potentials for enabling and disabling the reaction. Typical ones are exhibited in **Figure A3**. Due to a negligible current, a potential of 0 mV_{Pt} was assigned to reaction "off". For reaction "on", a

potential with profound ORR current was chosen. The parameters for each measurement, *i.e.*, sample potential for reaction "on", tip current setpoint and tip potential, are included in **Table A1**.

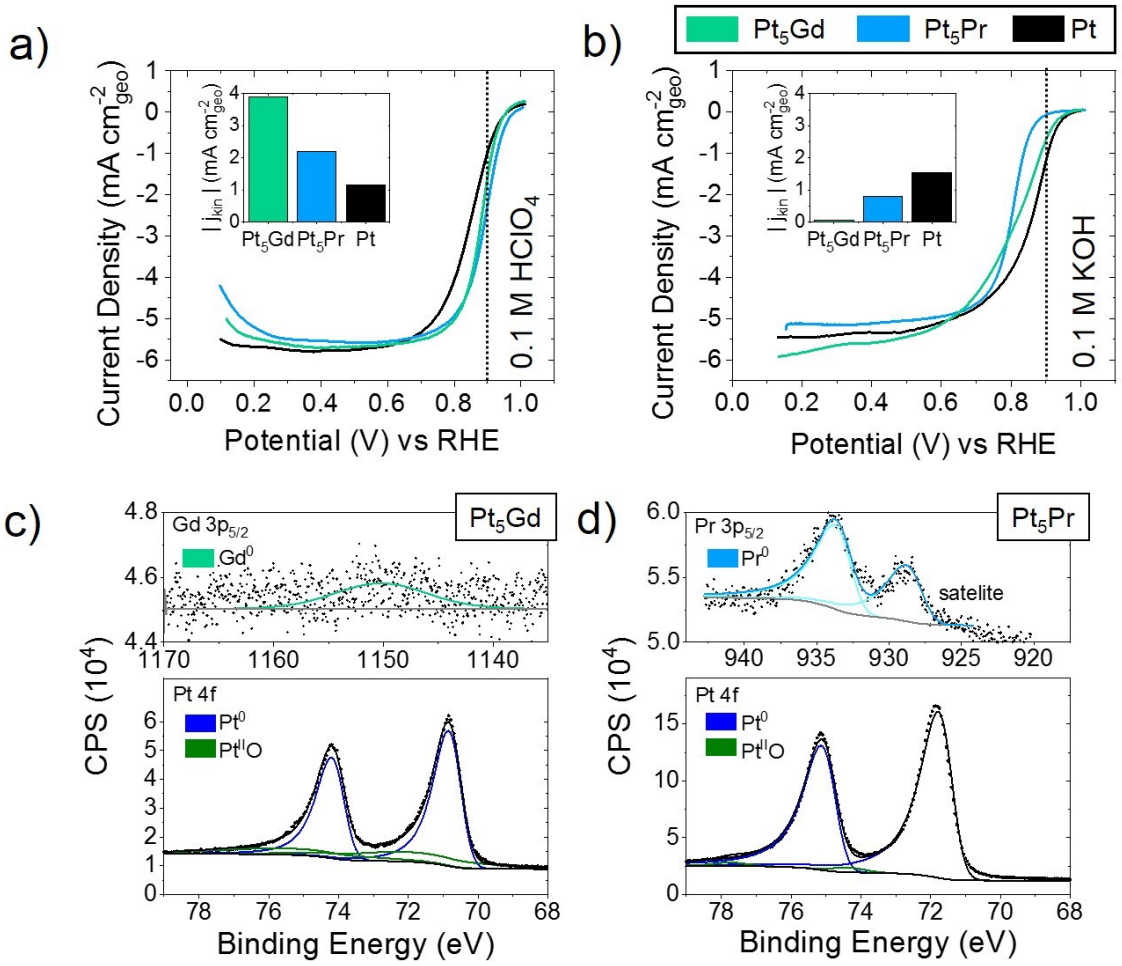

Figure 24 | a,b) Polarization curves (anodic sweeps) obtained from the RDE experiments performed in O_2-saturated electrolytes with a scan rate of 50 mVs^{-1} and a rotational speed of 1600 rpm, iR-corrected. The electrolytes were a) 0.1 M $HClO_4$ and b) 0.1 M KOH. The activities of Pt_5Gd (green) and Pt_5Pr (blue) are compared to polycrystalline Pt (black). In the respective insets, the kinetic current densities normalised to the geometric area and extracted at a potential of 0.9 V_{RHE} are provided. c,d) XPS measurements indicate de-alloying of both surfaces after the electrochemical treatment in acid. Data used for reference [251].

Since the ORR is a structure-sensitive reaction on Pt surfaces, sites of different coordination or geometry may show dissimilar local activities. For pure Pt(111) surfaces, it was discovered that sites of higher coordination bind the intermediates weaker than the regular terrace sites. In turn, sites of lower coordination bind stronger.[75, 76] Since, on average, Pt(111) binds intermediates stronger than optimal,[65, 132, 152] sites with higher coordination were identified as the active centres.[76] Such highly coordinated and thus active sites exist near the bottom of step edges or at concavities. The ORR active sites on Pt-based electrocatalysts is the content of Chapter 3.4. Inspired by the structure-activity relations identified on pure Pt surfaces, the geometry of the surface areas on the Pt alloys are compared according to their different tentative coordination: terrace sites, sites near the top of step edges and sites near the bottom of step edges. At these locations, the "regular", lower and higher coordination is established on the surface, respectively. With these considerations in mind, n-EC-STM was used on the Pt_5Gd and Pt_5Pr surfaces in both acidic (0.1 M $HClO_4$) and alkaline (0.1 M KOH) media.

At first, n-EC-STM was applied to Pt_5Gd in 0.1 M $HClO_4$. A typical image is given in **Figure 25**. The mapped area contains several step edges, two of which are marked in the picture with white dashed lines. The sample potential was switched between reaction "on" and "off" during the recording. If the reaction is "off", the EC-STM permits access to the surface morphology with a stable signal. If the reaction is "on", the image is modulated by noise features, which manifest as high-intensity spots of white colour in **Figure 25**a. As introduced in Chapter 5.3-5.4, the local activity relates to the extent of the noise. Bearing in mind the possibility of structure-activity relations, terrace sites, step tops and bottoms are distinguished. In the EC-STM image of **Figure 25**, less noise seems to be present near the bottom of the step edges, *e.g.*, near the dotted lines or at the position pointed out by an arrow.

For a more flexible view of the data in **Figure 25**a, a waterfall plot was compiled from multiple line scans (height profiles), which were performed in scan direction across the two step edges marked in the STM image. The surface behaviour can be compared for ORR "on" and "off", and the positions of the two step edges are emphasised by the black dotted lines in **Figure 25**b. In line with the expectation, the noise level of the line scans for reaction "off" is negligible.

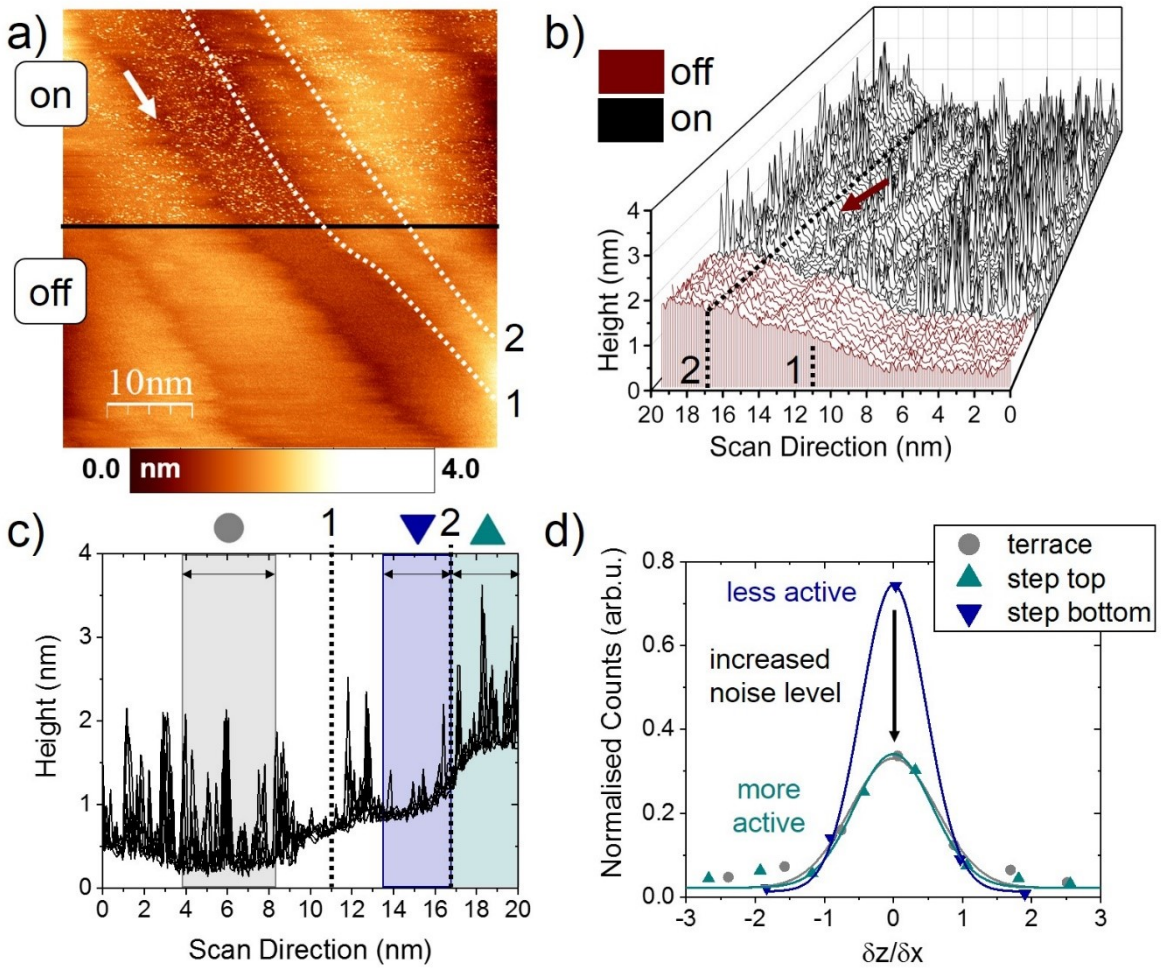

Figure 25 | n-EC-STM measurements on Pt_5Gd in 0.1 M $HClO_4$. a) EC-STM was recorded under reaction "on" and "off" conditions, as labelled in the image. Multiple step edges are present, of which two are numbered and marked by white dashed lines. When the reaction is "on", the noise seems lower at the step bottom compared to the terrace and step top, which can be seen near step edges no. 1 and 2, and at the position pointed out with an arrow. b) Waterfall plot for the reaction "on" and "off" comprise several line scans (height profile in the scan direction) across the two step edges marked in a. The noise is less pronounced at the step bottom; an exemplary spot is badged with an arrow. c) Several line scans for the reaction "on" stacked on top of each other. d) Comparison of the noise level for the terrace, step top, and step bottom. Data was chosen as given in c). Due to the higher intensity and lower FWHM of the respective histogram, one can deduce that step bottoms are less active than terraces and step tops. Data used for reference [251].

For reaction "on", it is visible that the height profiles are less noisy near the bottoms of the step edges, as exemplarily badged with the arrow. In contrast, terrace sites and spots near the top of the step show more distinct noise than the step bottom. The noise level of the terrace and top sites seems comparable.

To complement the quantitative observations of a lower activity near step bottoms, the extent of the noise was quantified with regard to the geometry of the surface areas. The procedure is explained in Chapter 5.4. For an accurate comparison, the area widths for step bottom and top sites around step no. 2 were equal. Each data set is encircled in **Figure 25**c. In **Figure 25**d, the histograms for the reaction "on" are given. The curves of the step top and terrace sites match each other. Hence, they can be assigned a comparable activity. The histogram of the step bottom sites exhibits a narrower shape of higher intensity. Therefore, the step bottom remains relatively inactive. The parameters obtained from the fits are provided in **Table A2** for each of the four systems. As a reminder, a large FWHM and a low height of the Gaussian curve correspond to a high noise level and *vice versa*. As the outcome, areas near the bottom of step edges on Pt_5Gd in acidic media show a lower FWHM, and thus activity, than the terrace and step top sites. The latter two types exhibit similar FWHM values and, therefore, comparable activities.

In the second step, the results of the n-EC-STM measurements for Pt_5Pr in 0.1 M $HClO_4$ are presented. A typical EC-STM image is displayed in **Figure 26**a. Numerous steps are present within the mapped area. As an example, a waterfall plot is included in **Figure 26**b for the step traced with a white dotted line in the STM image. Noise features appear when the reaction is switched from "off" to "on". Under ORR conditions, an increased amount of noise at elevated positions, as opposed to recesses, is visible. The arrows point to a selection of recesses with less noise. As a confirmation, histograms of the signal derivatives were compiled for the step marked in white in the STM image. Data sets were divided into step bottom, top and terrace sites as shown in **Figure 26**c. In **Figure 26**d, the step top and terrace areas yield broadened and low-intensity histograms in contrast to the step bottoms. As a result, the step bottom sites possess the least activity, whereas the step tops and terraces exhibit the highest activities, which are similar to each other.

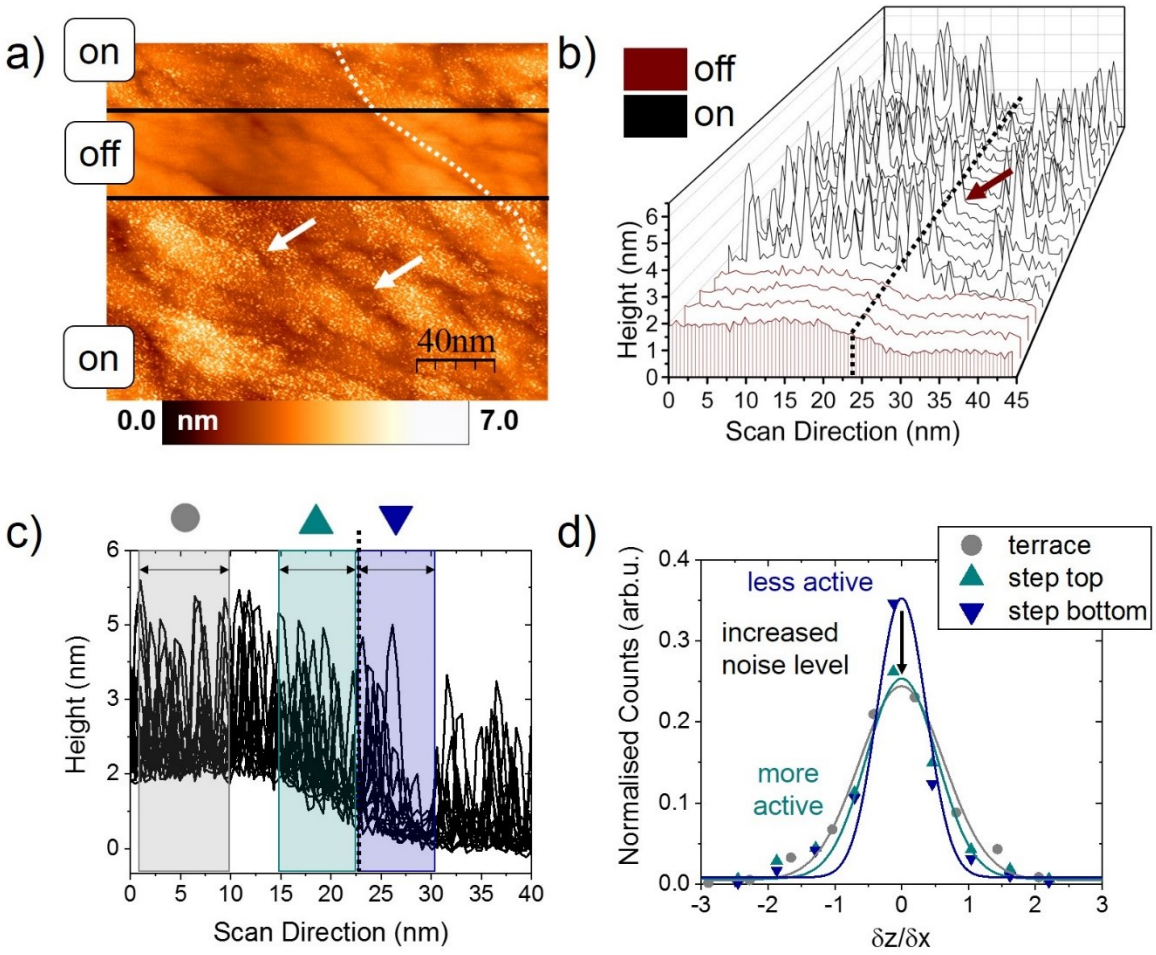

Figure 26 | n-EC-STM measurement on Pt_5Pr in 0.1 M $HClO_4$. a) The mapped area contains multiple step edges; one of them is highlighted with a dotted line. For reaction "on", the noise level seems to be higher at elevated spots and lower at recesses. Some of the low-noise areas are pointed to by arrows. b) Waterfall plot with line scans across the step edge marked in a). Near the bottom of the step is a noise-free gap, which is pointed out by the arrow. c) Height profiles across the step edge highlighted in a. The bottom of the step shows fewer noise features than the top and terraces. d) Histograms from the data shown in c. Step top and terraces possess a broader and low-intensity histogram compared to step bottoms. Therefore, step top and terraces contribute the most to the overall activity and a similar extend. Step bottom sites remain relatively inactive. Data used for reference [251].

In conclusion, the trends on Pt_5Pr are comparable to those observed on Pt_5Gd in an acidic medium. Additional measurements on Pt_5Pr and Pt_5Gd, which substantiate the findings reported here, are included in references [251] and [252]. In these studies, step bottom sites and concavities display the lowest noise level among the considered geometries. In contrast, terrace sites and areas located near the top of step edges contribute the most to the overall activity. The activities between the latter two site types are comparable.

The geometric considerations mentioned in the introduction and Chapter 3.4 can now be of service for the interpretation of the n-EC-STM data gathered in the acidic medium. Pure Pt surfaces yield stronger than optimal adsorption energies. As subject to Chapter 3.4.2, alloying Pt with other metals can lead to compressive strain, which diminishes the binding strength of the surface toward chemisorbed species. As shown in the double volcano in **Figure 12**b for polycrystalline alloys, Pt_5Gd and Pt_5Pr lie on the weaker binding side. In these systems, the alloying effect weakens the interactions "too much". Pt_5Gd is close to the top of the volcano on the weaker binding side, whereas Pt_5Pr binds considerably weaker.[143] Those binding conditions can be seen as an "average" behaviour of the surface. Still, locally, sites of certain coordination can differ from the "average" binding tendency. Inspired by the study on pure Pt, surface sites with lower coordination may bind the ORR intermediates stronger than the terraces and *vice versa*.[75, 76]

From the n-EC-STM study, step bottom sites seem relatively inactive on both Pt_5Gd and Pt_5Pr. These belong to the category of "overcoordinated" sites, and thus one can assume that they possess the weakest binding energies towards the intermediates. Since "on average", sites on the Pt-lanthanide alloys bind weaker than optimal,[143] it seems reasonable that surface sites that bind even weaker show the lowest activity. Hence, the experimental observations are in line with the volcano-type predictions. Moreover, step top and terrace sites demonstrate the best catalytic properties. In the measurements, their noise levels are similar, which indicates comparable ORR performances. Still, one can only speculate about an explanation. A possible reason for the similar activity could be a less pronounced variation in binding energies between the terrace and the step top sites than between the terrace and the step bottom sites. In such a

case, the differences in activities between terrace and step tops would be less pronounced and thus appear similar in the n-EC-STM study. As an alternative explanation, step top sites could bind much stronger than terraces. In this case, step tops would bind "too strongly", which would diminish their activity. In the illustrative view of a volcano plot, step top and terrace sites would be on dissimilar sites of the top of the volcano. Irrespective of the phenomenological origin, one can state that both step top and terrace sites are beneficial for the ORR electrocatalysis on Pt_5Pr and Pt_5Gd.

Subsequently, the particulars gathered on extended surfaces can be applied to nanoparticles. It is suggestive that Pt_5Pr and Pt_5Gd particles, which possess terrace and "undercoordinated" sites, will be more effective toward the ORR. In agreement with this assumption is the report of a prime ORR performance of spherical, defect-free Pt_5Gd nanoparticles.[245] In their report, the ORR activities (normalised to surface area) of the Pt-Gd particles were superior to other alloys exhibiting the same round shape. The comparison between nanoparticles of different mass-selected sizes led to the trend of higher activities for larger particles. With the increasing sizes of the round nanoparticles, the share of terrace sites is larger, which agrees with their better catalytic capabilities. In addition, Fichtner *et al.* synthesised Pt_xPr nanoparticles with deliberately introduced concave defects. Since they yielded a lower ORR activity than the corresponding extended Pt-Pr surface[157], the statement of an inferior performance of concavities to extended surfaces is plausible. This agrees with the findings of the n-EC-STM experiments.

In addition to the experiments in an acidic medium, the equivalent measurements were carried out in an alkaline medium, 0.1 M KOH. It is known that the choice of electrolyte or pH can affect the nature of ORR active sites.[81, 137, 151, 154] Therefore, it is interesting to use n-EC-STM to make a statement on the active sites on the Pt-lanthanide alloy surfaces when changing the electrolyte from 0.1 M $HClO_4$ to 0.1 M KOH.

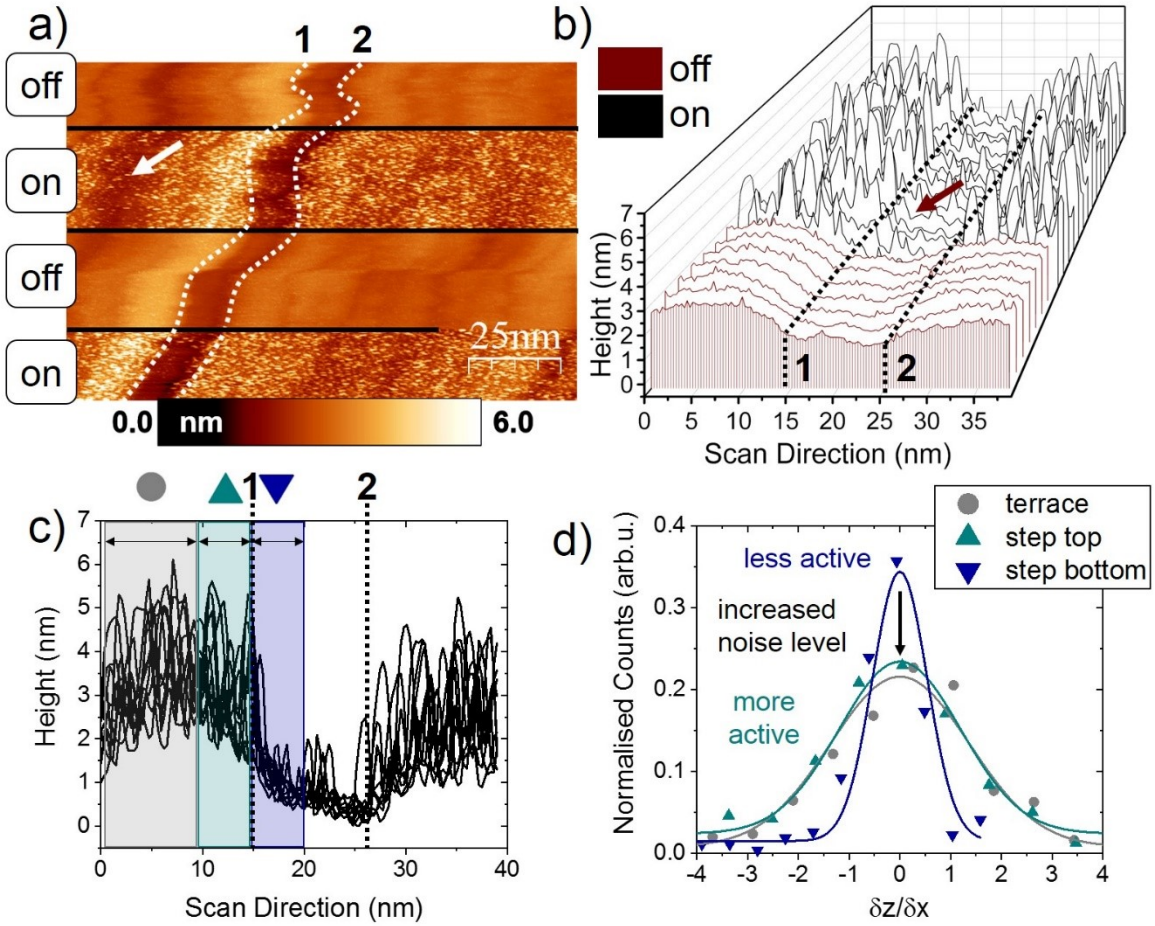

Figure 27 | n-EC-STM measurement on Pt_5Gd in 0.1 M KOH. a) The image includes multiple step edges and concavities. The most prominent is underlined by white, dotted lines. At step bottoms located in-between the dotted lines or at the position marked by the arrow, the appearance of the noise is diminished. b) Waterfall plot rendered for the steps highlighted in a). At the step bottom, areas with less noise are pointed out by the arrow. c) Stacked line scans for reaction "on". Particularly in the middle of the lower terrace where the two step bottoms meet (at x ≈ 20 nm), the noise level is increased again. d) Histograms for step no. 1, confirming that step bottoms have the smallest activity.

Figure 27 gives an n-EC-STM measurement on Pt_5Gd in 0.1 M KOH. The image contains various step edges; two are emphasised by dotted lines. Under an ongoing reaction, the noise level appears similar across the surface, except for step bottom sites, which seem to be less active. Noise-free spots can exemplarily be detected at the position marked with the white arrow or between the two dotted lines. In addition, a waterfall plot across the two selected step edges is provided in **Figure 27**b. At the bottom of each of the two step edges, the noise in the STM signal is less pronounced, pointed out by an arrow. As seen best from the stacked line scans in **Figure 27**c, the noise level is low at the step edge bottoms. Remarkably, in the middle of the ditch (at $x \approx 20$ nm), built up by the two adjacent step bottoms, a distinct increase in noise can be observed. At this position, a similar geometry as on flat terrace sites is established. Hence, the appearance of the noise at this spot matches the observation of a superior activity of terrace sites to step bottoms. For a quantitative understanding, **Figure 27**d contains the histograms compiled for the step on the left side (step no. 1). Since step bottom sites belong to the curve with the lowest FWHM (*cf.* **Table A2**), they can be ascribed to the lowest activity. Sites near the top of the step and on terraces show a higher activity, which is comparable to one another.

As the last system, the n-EC-STM measurements on Pt_5Pr in 0.1 M KOH are considered. An example is depicted in **Figure 28**. In the recorded area, the surface contains multiple concavities and elevations. According to the image, the noise is less conspicuous at recesses compared to elevations. White arrows mark examples of such lesser noisy areas in **Figure 28**a. As supplemental information, the waterfall plot across the step traced with a dotted line in **Figure 28**a is accounted for in **Figure 28**b. **Figure 28**c provides a version where the ORR "on" data is stacked on top of each other. Here, it shows that there is less noise at the lower half of the step for some of the line scans, badged with an arrow. For the noise level quantification, **Figure 28**d displays the histograms for the data sets assigned in **Figure 28**c. The shapes of the histograms suggest that step bottom sites possess lower activities than terrace and step top sites. However, for this system, the relative differences in the noise level are less striking than for the other systems. This also becomes apparent from the fitting parameters given in **Table A2**.

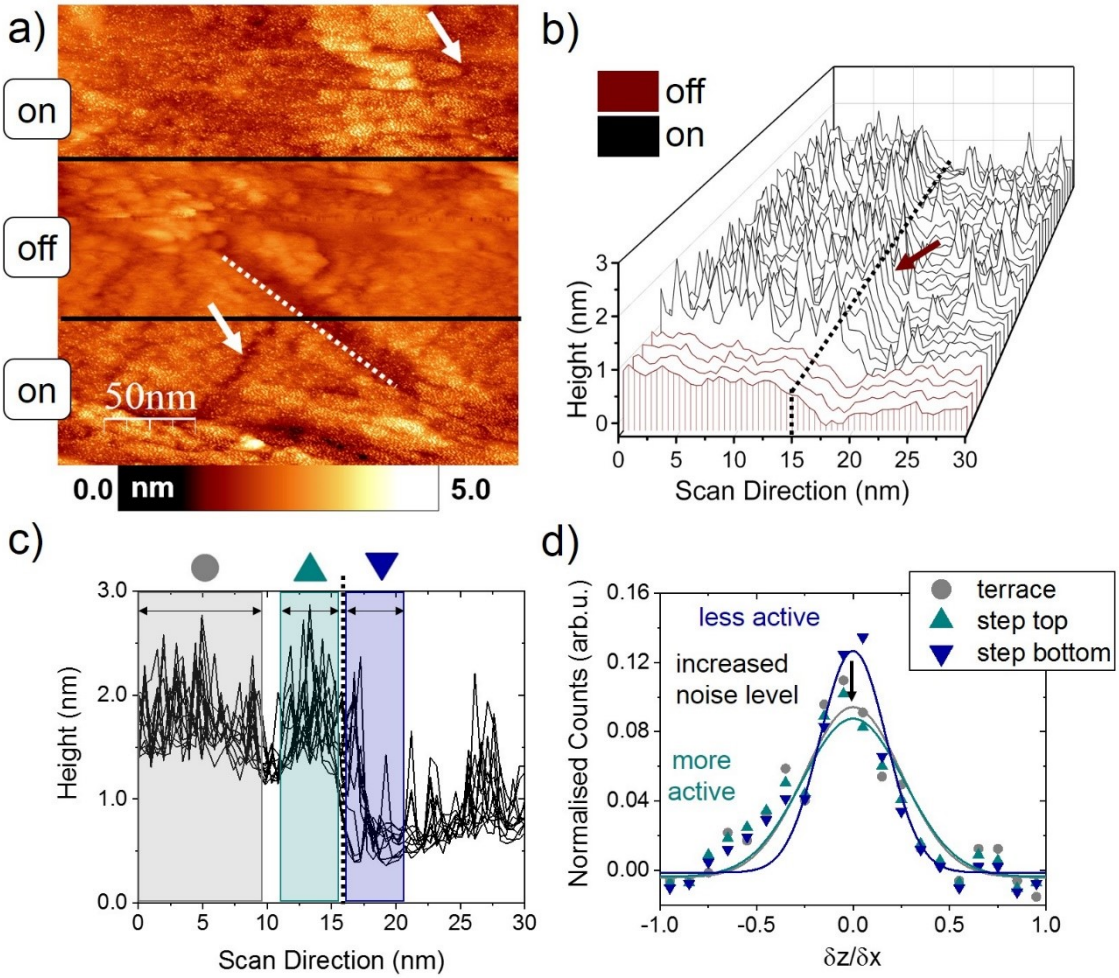

Figure 28 | n-EC-STM measurement on Pt_5Pr in 0.1 M KOH. a) During the recording, the sample potential was switched from reaction "on" to "off" and back. At some concavities or step bottoms, the noise level may be diminished, *e.g.* at the positions marked by the arrows. The step edge with the dotted line will be further investigated. b) Waterfall plot across that step edge. Near the step bottom, the noise seems to be less prominent, *e.g.*, as assigned with the arrow. c) Line scans across the step stacked on top of each other. d) Corresponding histograms rendered from the data in c) lead to the assumption of all three site types showing comparable noise levels, with the step bottom sites tending to be less active.

As a summary of the findings in the alkaline medium, the step bottom sites on these electrocatalysts seem to be less active than terraces and step tops. However, for the alkaline electrolytes, the activity trends are less established, especially when taking the additional measurements in reference [252] into account. In some images, the step bottom sites show similar activities to terrace and step top sites. The following discussion of the results is, therefore, to be treated with care since corroborating experiments would be necessary for a more decisive identification of the active geometries.

In alkaline media, the nature of the active sites on Pt surfaces is less well understood, even though dependences on the pH and the cation type have been reported.[80, 81, 253, 254] Pt(111) was proven to be a better ORR catalyst in 0.1 M KOH than 0.1 M $HClO_4$.[80] A divergent trend is observed on Pt-stepped single crystals. Here, a higher density of steps diminishes its capacities toward the ORR in alkaline media.[153] This leads to the assumption that, in contrast to acidic media, step sites on Pt(111) have inferior activity compared to terrace sites. Previous n-EC-STM measurements have confirmed this.[154] Thus, alkaline media may shift the surface toward weaker binding. Thus, Pt(111) terrace sites, which bind too strongly in acidic, perform best in alkaline media. *Vice versa*, step sites of weaker binding in acidic media bind even weaker in alkaline solutions, which reduces their activity. In contrast to pure Pt surfaces, less is reported about the ORR active centres on Pt alloys in alkaline media. Cu/Pt(111) near-surface alloys and $Pt_3Ni(111)$ performed better in the alkaline than in the acidic medium.[253, 255] Concerning the Pt_5Gd and Pt_5Pr surfaces, we observe a higher ORR activity in acidic than alkaline medium. In this study, the most efficient catalyst in acidic, Pt_5Gd, operates the worst in alkaline. Based on those literature findings, an attempt can be made to interpret the n-EC-STM results. Transferring the theory that surface sites bind weaker in alkaline than acidic media to Pt_5Gd and Pt_5Pr is partially congruent with the n-EC-STM experiments. On Pt_5Gd, indeed, the step bottoms are inactive, step tops and terrace sites bind comparably. The weak-binding step bottoms bind weaker in alkaline and are thus less active. However, on Pt_5Pr, all surface geometries showed similar noise levels. This would explain why Pt_5Pr performs better than Pt_5Gd, because, for a yet-unknown reason, step bottoms contribute to the ORR as well. Note, however, that comparing noise levels between different systems, let alone images, is not

feasible. Between the measurements, the extent of the overall noise can vary, *e.g.* with the shape and the isolation of the tip. Therefore, it is only possible to compare the degree of noise within the same image or in successively recorded images, but not between various systems. Therefore, with the n-EC-STM method alone, one cannot conclude whether the alloys perform better in alkaline or acidic medium. Unfortunately, a clear trend in the nature of active sites in the alkaline medium cannot be established yet. Further experiments or additional calculations would be necessary.

In summary, the active sites on Pt_5Pr and Pt_5Gd surfaces were explored using n-EC-STM. In alkaline media, the results are yet not conclusive enough to shape a statement. For acidic media, *i.e.* in 0.1 M $HClO_4$, terraces and spots near the top of step edges have been identified as the most active. In contrast, sites near the bottom of step edges show inferior activity. This trend differs from the observations on pure Pt surfaces.[54, 75, 76, 151] A brief explanation is that Pt(111) surfaces bind intermediates stronger than optimal[65, 132, 152] while terraces of the Pt-lanthanide alloys tend to bind them too weakly[143]. These findings can be useful for the rational design of nanostructured ORR electrocatalysts based on Pt-lanthanide alloys. Guided by the n-EC-STM results, one can predict that in contrast to pure Pt, spherical particles[155] should outperform their concave and defective counterparts[157] for alloyed Pt-Gd and Pt-Pr nanostructures. Furthermore, it becomes clear that insights into the nature of active sites for an individual catalyst material are vital in rational catalyst design; and there is a need for suitable surface-sensitive techniques providing access to the active sites.

8 Monitoring Active Sites on $Pt_3Ni(111)$ for the Oxygen Reduction Reaction

As discussed previously, the ORR activity of Pt catalysts can be enhanced by alloying. An exceptional ORR activity was reported for $Pt_3Ni(111)$, which approached the optimal binding conditions.[148] Inspired by this discovery, many groups have synthesised Pt_xNi nanoparticles with high performances[23, 158-160]. However, the nanocatalysts are not yet competitive with the extended surfaces.

To contribute to the understanding of these highly active Pt-Ni catalysts, well-defined $Pt_3Ni(111)$ surfaces were studied regarding the ORR active sites. Prior to the electrochemical examination, the $Pt_3Ni(111)$ single crystal (Ø 5 mm, MaTecK) was sputter-cleaned under UHV conditions using an Ar^+-beam of 10 µA ion current and 1 kV energy. It was annealed for 10 min after each sputtering step, and the temperature was stepwise increased to a maximum of 1050 K. After the last annealing step, the sample was slowly cooled down to room temperature. Methodical details and instrumentation are given in Chapter 4. The n-EC-STM technique is referred to in Chapter 5.

For the above-described sample preparation procedure, it was stated that the atomic layer on the surface contains only Pt ("Pt-skin"). This Pt-enrichment may be balanced by the composition of the two to three layers below the surface, which may be depleted of Pt and contain more Ni compared to the bulk ratio.[148]

With LT-STM, a well-ordered surface was monitored with atomic resolution, as presented in **Figure 29**ab. The lattice constant was obtained from eight independent LT-STM measurements. Per image, the atom-to-atom distance was measured twice in each of the three directions of the crystal lattice and was averaged over ten atoms. In addition, the length scale was calibrated with a reference Ag(111) sample. The error of the lattice constant includes statistical errors for both the $Pt_3Ni(111)$ lattice constant and the Ag(111) calibration sample.

Finally, the lattice constant yielded a value of (2.611 ± 0.073) Å. In comparison with the lattice constant of 2.77 Å for Pt(111)[225], the $Pt_3Ni(111)$ surface is compressed. Remarkably, an irregular pattern of darker and brighter intensities seems to superimpose the actual lattice in **Figure 29**a. Even though not exhibiting a well-ordered Moiré pattern, this irregular superlattice may establish by non-uniform strain. Hence, it is suggestive that strain effects play a crucial role in ORR electrocatalysis. Furthermore, the (111) arrangement of the atoms, visible in the LT-STM images, is in agreement with the geometry of the LEED scattering pattern (**Figure 29**c).[148, 256]

After the surface science study, the sample was subject to an electrochemical analysis in 0.1 M $HClO_4$. The CV in **Figure 29**d agrees with the literature.[148, 172] The RDE experiment, shown in **Figure 29**e, yields an ORR activity (*cf.* **Eq. 33**) of 7.6 mA cm^{-2}, which is slightly above the value reported in reference [172]. It is thus confirmed that the $Pt_3Ni(111)$ sample exhibits a high ORR performance.

In the next step, n-EC-STM measurements were carried out to determine the nature of the active sites, which are responsible for the superior ORR performance compared to pure Pt(111). At first, CVs were recorded in the EC-STM set-up, against a Pt RE and in air, to distinguish sample potentials for reaction "on" and "off". An example is shown in **Figure 29**f. Due to a negligible sample current, the potential for reaction "off" was set to 0 mV_{Pt}. To switch the ORR "on", a negative potential resulting in considerable current was selected (*i.e.* potentials smaller than -0.1 mV_{Pt}). For convenience, a more negative potential yielding a higher ORR current is in the following termed a higher "overpotential", even though the Pt *quasi*-RE is not transferable to an absolute scale.

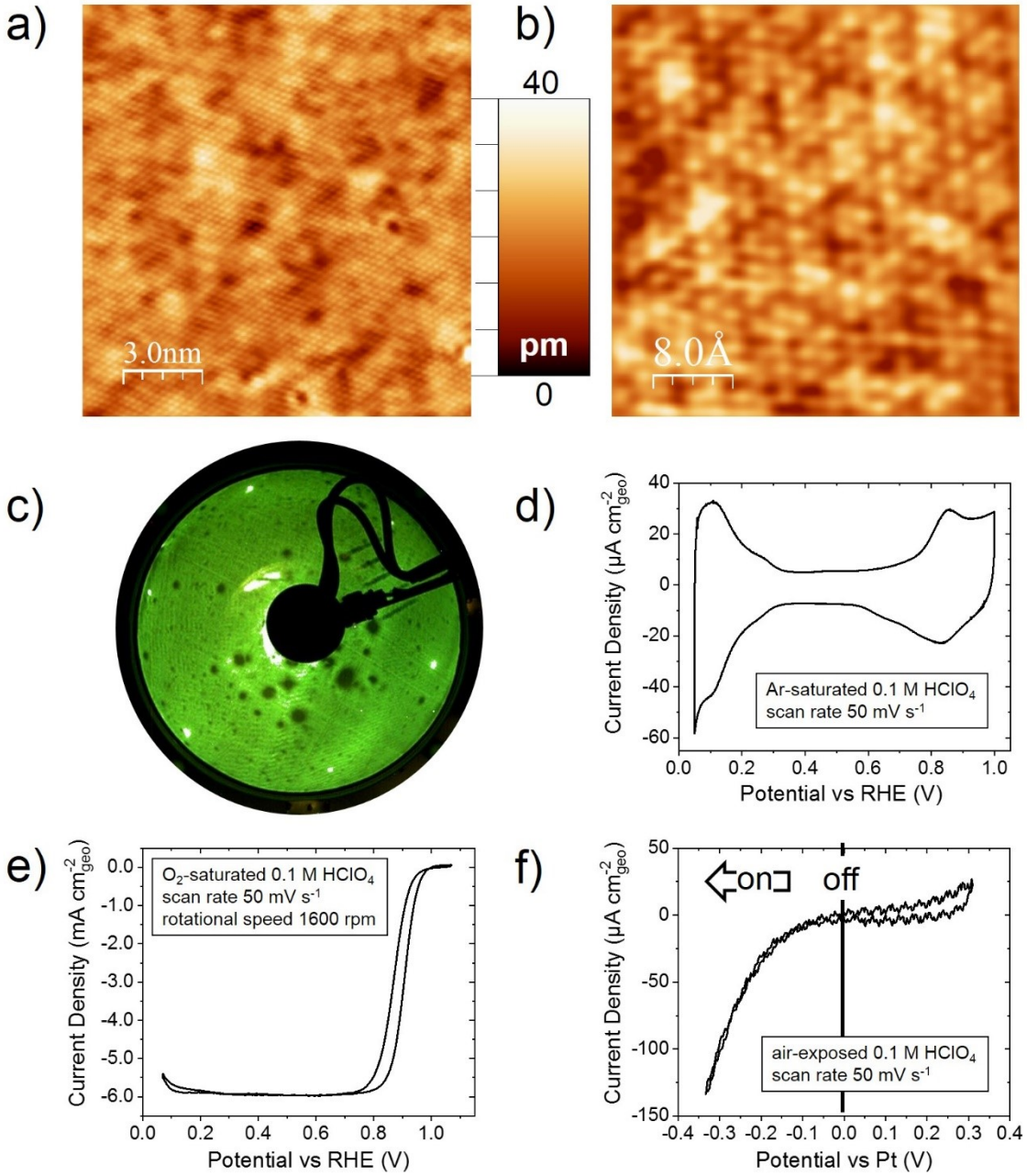

Figure 29 | Surface and electrochemical characterization of $Pt_3Ni(111)$. a,b) High-resolution LT-STM images. The colour code applies to both images. c) LEED of the freshly prepared crystal. d) CV in Ar-saturated 0.1 M $HClO_4$ at a scan rate of 50 mV s^{-1}. e) Polarisation curve recorded in O_2-saturated 0.1 M $HClO_4$ at 1600 rpm rotational speed and a scan rate of 50 mV s^{-1}, 85% iR-corrected. f) CV performed in the EC-STM set-up against a Pt quasi-reference electrode and with the electrolyte exposed to air. For the later n-EC-STM experiments, a potential of 0 mV_{Pt} was chosen for reaction "off" and a potential with noteworthy current as ORR "on".

Figure 30a provides the n-EC-STM results of a flat (111) terrace. If no reaction occurs on the surface (black height profiles), the signal is stable. In line with the functionality of the technique, the noise level is considerably increased if the ORR is switched "on" (green curves). This can be seen from the numerous spikes in the signal of the otherwise flat terrace. To strengthen the expressiveness of the images, the quantification approach introduced in Chapter 5.4, is applied to the EC-STM data. For the histograms in **Figure 30**b, data points within a width of 10 nm scan size were extracted, as marked with the arrow in **Figure 30**a. To account for the possibility of data sets of different sizes, the histograms were normalised to the number of data points per set. As seen from **Figure 30**b, the histogram of the terrace sites for reaction "on" is of higher FWHM and lower intensity than for reaction "off", which is in line with a higher degree of noise in the signal. Judging from the noise features under reaction conditions, the (111) terrace sites contribute evenly to the overall reaction.

After affirming the activity of (111) terrace sites, one can proceed to evaluate more complex geometries, *e.g.* as found at step edges. **Figure 30**c includes the height profiles of the STM signal across such a step. Its position is indicated by the red diamond-shaped symbol. In agreement with the previous measurement, extended terrace sites, as found to the right of the step, display a homogenous noise level increase under ORR conditions. The noise features seem less pronounced at the step edge, especially toward the bottom of the step (*cf.* position marked with the red arrow). Subsequently, histograms are rendered from the data around the step centre and the extended terrace on the right, as marked in the image. For a profound evaluation, the width of the data sets in the scan direction is again set to 10 nm, and a bin size of 0.2 was chosen for all images. If the reaction is prohibited (black-grey curves), the histograms possess a narrow FWHM and are of high intensity. The two curves for step and terrace sites match each other, which confirms a noise-free signal of the whole surface. In contrast, for ORR "on", the histograms are of higher FWHM and lower intensity, in line with a higher degree of noise. According to the Gaussian fits for step and terrace sites, less noise emerges at the steps than at the adjacent terrace.

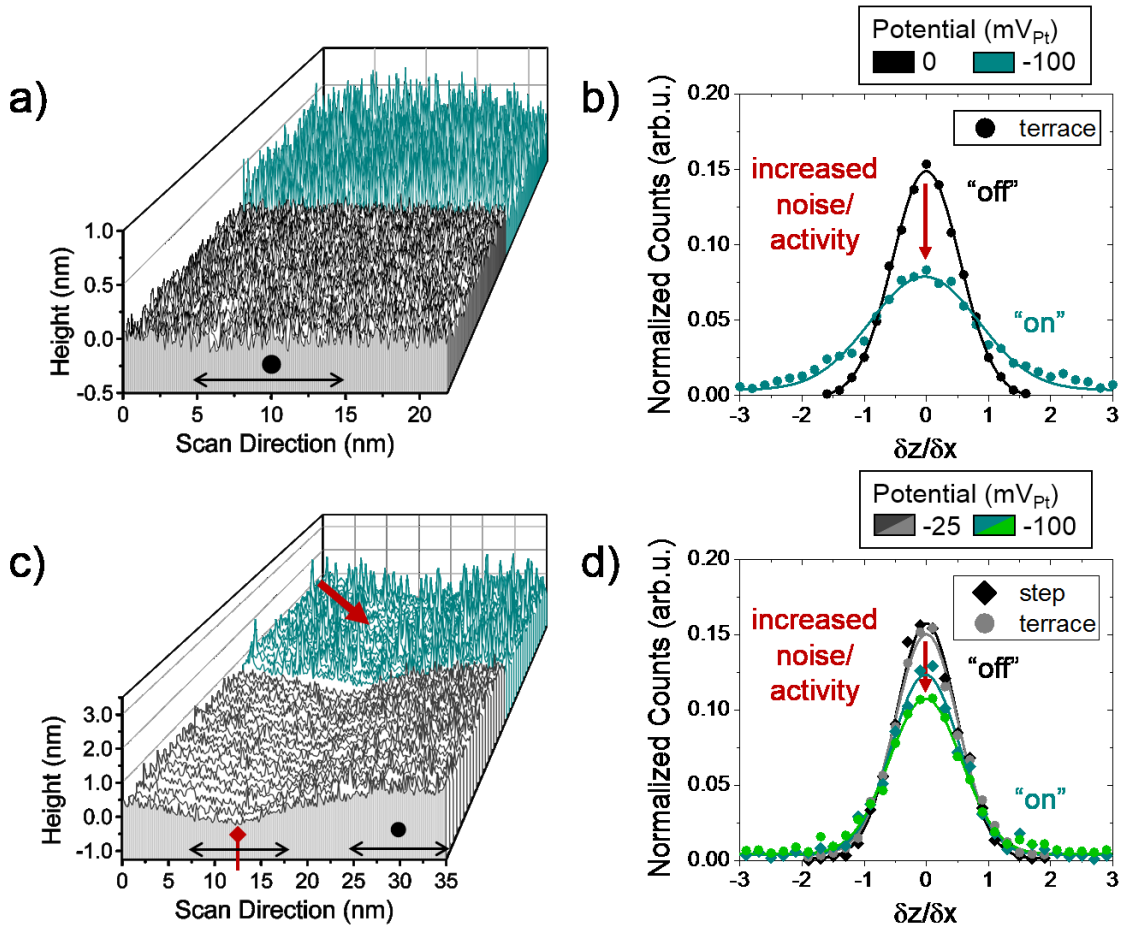

Figure 30 | n-EC-STM measurements on $Pt_3Ni(111)$ in 0.1 M $HClO_4$. a) The EC-STM signal (height profile) of a flat terrace under ORR "on" (green colour) and "off" (black) conditions. Homogenous fluctuations in the signal are visible for reaction "on", which indicates an equal activity of the (111) terrace sites. b) Histograms compiled from the terrace data in a. Under reaction conditions (green curve), the Gaussian fit shows a higher FWHM and lower intensity, which is in line with a higher noise level. c) Waterfall plot comprising of line scans across a step edge, marked with the red diamond symbol. Compared to the adjacent terraces, the bottom of the step edge seems to show a lesser degree of noise for ORR "on" (green curves), *e.g.* at the position of the arrow. d) Noise quantification of the data marked in c. If the reaction is disabled (black-grey), the histograms of step and terrace sites match, which is in line with the expectation of a noise-free signal irrespective of the surface sites. Under ORR conditions (green), the histogram of the step edges exhibits a lower FWHM and higher intensity, and thus lower activity, than the terrace sites.

The observations in **Figure 30** imply that $Pt_3Ni(111)$ terrace sites are active toward the ORR. Step sites show a lower activity. To substantiate this hypothesis, more n-EC-STM measurements were conducted and are given in reference [257]. It turned out that step sites are of either lower activity than terrace sites or are comparable but never more active.

Such an additional measurement across step sites is shown in **Figure 31**. During the recording, the sample potential was stepwise altered to yield higher ORR reaction rates. In the last step, the reaction was switched "off". The image yields various observations. First, the noise features grow larger in number and density at higher "overpotential". Second, the appearance of the noise is "reversible", meaning that it disappears if no reaction takes place. Contemplating the STM signal of step and terrace sites, in this case, spots yield similar noise extents at every applied sample potential. Exemplarily, a waterfall plot, composed of height profiles across the left step edge, is provided in **Figure 31**b. This graph confirms that the overall noise level is increasing with the "overpotential", and that step can reach the activity of terrace sites.

In the following, the quantification procedure reported in reference [54] for Pt(111) is extended to $Pt_3Ni(111)$. In this procedure, the local activities between step and terrace sites can be related. A more detailed introduction is given in Chapter 5.4. In the first step, data sets are divided into step and terrace sites, as marked in **Figure 31**b. To be consistent, the width of the data sets was set to 10 nm, and the bin size for the histograms to 0.2. The corresponding histograms of step and terrace sites are given in **Figure 31**c and d, respectively. The FWHM from the fits is plotted *versus* the potential for terrace and steps in **Figure 31**e. A linear trend can be seen, which agrees with the findings on pure Pt(111).[54] In the second step, the local activities are quantified. Therefore, the TOF of the sample is calculated from the overall sample current at a certain potential according to **Eq. 14** in Chapter 2.1.4. For a (111) arrangement, the angle α can be set to 60°. The atom-to-atom distance, d = 2.611 Å, was extracted from the LT-STM data. The number of electrons transferred per reaction event is n = 4 for the ORR. Thus, the TOF of the sample at the geometric sample current density j amounts to

$$\mathrm{TOF} = \frac{|\,j\,|\,d^2 \sin\alpha}{ne} = \frac{(2.611\ \text{Å})^2 \sin 60°}{4 \times 1.602 \times 10^{-19}\mathrm{C}}\,|j| = 921\,\frac{\mathrm{cm}^2}{\mathrm{As}} \times |j|. \qquad \textbf{Eq. 37}$$

According to the sample preparation method and the LT-STM images, a mainly defect- and step-free surface is assumed. Therefore, one can suppose that the sample current constituted mainly from terrace sites and that other sites contribute only negligibly. Thus, the TOF of the terrace sites (TOF_t) can be equalised to the TOF calculated from the whole sample current as given in **Eq. 37**. The TOF_t is then plotted against the FWHM for each sample potential, as shown in **Figure 31**f. TOF and FWHM can be related linearly, and the curve of terrace sites is accordingly fitted with a straight line. Thus, the linear fit of the terrace data can serve as a calibration to acquire the local activity of the adjacent step sites.[54]

The TOF of the step sites (TOF_s) is then extracted from the linear relation between FWHM and TOF. The FWHM of the step sites is known from the corresponding histograms (**Figure 31**c). In **Figure 31**f, the TOF_s of the steps can then be read off. In the last step, an enhancement factor is defined as the ratio of the TOF of step and terrace, *i.e.*, TOF_s/TOF_t. These are shown in the inset of **Figure 31**f. Here, the enhancement factors lie close to one, which again confirms the similar activities of the terrace and the step sites. This procedure can serve as confirmation for the quantification approach established for Pt(111) to be extendable to diverse catalyst systems.

From the n-EC-STM measurements, one can conclude from the homogeneous appearance of the recorded noise that a defect-free $Pt_3Ni(111)$ terrace consists solely of active sites. This becomes understandable if one keeps in mind the close-to-optimal binding conditions to key intermediates such as *OH.[148] Further experimental reports verify the superior activity of the (111) facet as opposed to other low-index surfaces such as (100) and (110).[148] In addition, the high activity of the (111) orientation was observed on nanoparticles, where particles of octahedral shape with (111) facets exhibited superior activity to cubic shapes with (100) facets.[258] Motivated by the extraordinary performance of $Pt_3Ni(111)$ single crystals, many groups synthesised Pt_3Ni octahedral nanoparticles and stabilised them by the introduction of foreign atoms, such as Ga, Mo or Rh.[24, 259-261]

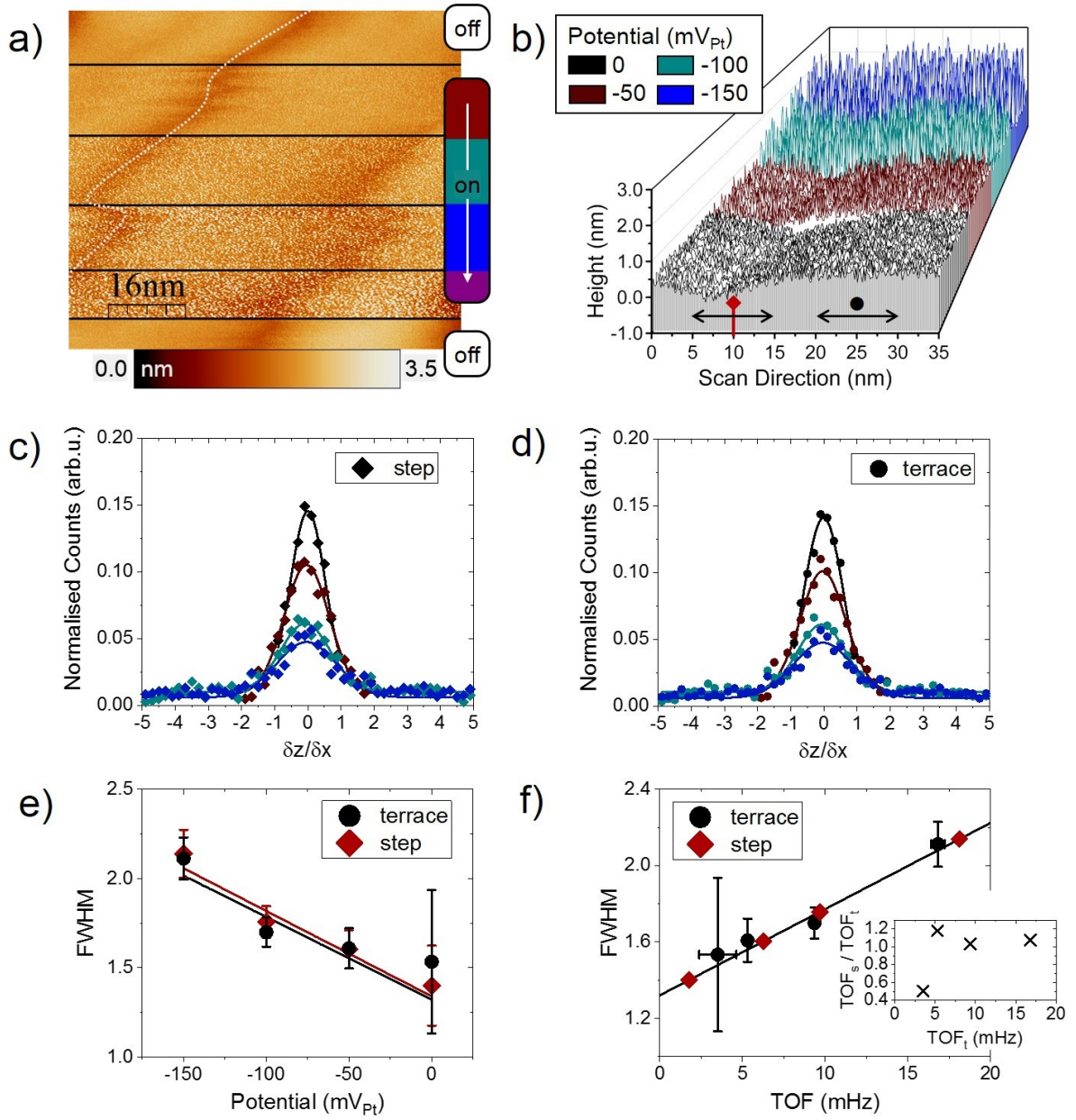

Figure 31 | a) n-EC-STM measurement of two regular step edges on the $Pt_3Ni(111)$ surface with the applied potential according to the colour code. With increasing the "overpotential", the noise features get more pronounced. Step and terrace sites show a comparable noise level at each potential. b) Waterfall plot comprising the height profiles in scan direction across the step marked in a. From the data, histograms for the c) step and d) terrace sites were compiled. The histograms broaden and lose in intensity with increasingly negative potential, which is in line with a higher noise level. For each potential, the curves for step and terrace sites are comparable, yielding a similar ORR activity. e) The FWHM from the Gaussian fits plotted *versus* sample potential. f) The FWHM plotted against the TOF of step and terrace sites (see text for details) yields a linear trend. The enhancement factors are given in the inset.

The involvement of the step sites in the ORR is more difficult to distinguish. In this regard, Hoshi *et al.* studied stepped $Pt_3Ni(111)$ single crystals with monoatomic step edges in (111) and (110) orientation.[172] The authors state that an increasing number of (111) steps decrease the activity, whereas the Pt[n(111)x(100)] series showed a hypothetical optimum for n = 4. One can hence conclude that (100) steps are more active than (111) steps. The stepped single crystal study is summarised in **Figure 12**a and compared to stepped Pt single crystals.[143] Remarkably, the range in which the activity of the Pt alloy stepped crystals lie is smaller than for the corresponding series on Pt. One can speculate that the occurrence of step sites may have a larger impact on the overall activity on pure Pt surfaces than for Pt_3Ni. In the n-EC-STM measurements, step sites demonstrate an inferior or similar activity to adjacent terrace sites. A simplistic explanation may be that the steps exhibit different facets, *e.g.* (100) or (111), and therefore possess dissimilar activates. Since it is not possible to access the orientation of the step edges in n-EC-STM, this remains speculation. As a side note, since the activities of the Pt_3Ni series in **Figure 12** seem to vary less with the orientation and number of step edges than on Pt, the difference in noise levels between step and terrace sites may be less pronounced.

In summary, $Pt_3Ni(111)$ was examined, and its higher ORR performance was confirmed. Notably, with LT-STM it was possible to resolve the atomic lattice, yielding a lower lattice constant than pure Pt(111). This suggests that strain effects could play an important role. With n-EC-STM, (111) terrace sites were identified as most active, whereas step sites ranged from inferior to similar activities as terraces. The varying activity of step edges may be ascribed to differences in orientation. Currently, DFT calculations are being undertaken to elucidate the binding conditions of numerous geometric surface features of $Pt_3Ni(111)$. Preliminary results suggest that step sites bind weaker than terrace sites and thus exhibit lower activities. With this study, the knowledge about active sites for the ORR at Pt alloys can be expanded and provide ideas for the catalyst design.

9 Outlook: Bifunctional Carbonaceous Materials

Both the OER and ORR are fundamental to electrochemical energy storage and conversion devices. In special cases such as for reversible fuel cells or metal-air batteries, so-called bifunctional catalysts are required, which show good activity toward both the OER and the ORR. The previous chapters are dedicated to state-of-the-art uni-functional materials for the ORR and OER, respectively. However, the abilities of these transition metals for bifunctional catalysis are limited. The reason is the formation of insulating Pt oxides during the OER on the one side [262] and a reduced ORR activity of IrO_2 and RuO_2 on the other side[263]. Moreover, their scarcity and high-cost limit large-scale implementation motivate the search for alternatives.

A promising class of such alternatives are carbon-based materials due to their high specific surface area, electrical conductivity and economic viability.[264, 265] In the past, they were mostly employed as support for metal electrocatalysts.[266-269] More recently, studies have shown that doping (with *e.g.* nitrogen, sulphur or boron) and structural modification of the pure carbon lattice can yield higher durability and activity in alkaline media.[265, 270-276] In these studies, carbon-based catalysts have not only been reported as interesting alternatives for individual reactions but also as promising bifunctional electrodes. To make this material class-competitive in real-world applications, an in-depth understanding of their behaviour *in-situ* is advisable.

This outlook is, therefore, dedicated to the use of n-EC-STM on carbonaceous bifunctional surfaces in an alkaline medium. It is demonstrated that both the OER and ORR active sites can be monitored at the same position of the sample with down to atomic resolution. In this study, highly oriented pyrolytic graphite (HOPG) serves as a model for more advanced carbon systems.[264, 265] The sample (MikroMasch, spread 3.5°±1.5°) was prepared by removing several surface layers with scotch tape. The electrolyte was 0.1 M KOH, which was prepared by dissolving KOH pellets (99.99%, Sigma Aldrich) in ultrapure water. The EC-STM system is

described in Chapter 5. In this case, as the CE, a graphite rod (Goodfellow, Ø 0.5mm, 99.95% purity) was used to rule out the deposition of foreign material on the sample. Further information and additional n-EC-STM images are included in reference [277].

The n-EC-STM technique can identify active sites by virtue of a locally confined increase in the noise level of the STM signal with respect to inactive sites. To assess the active centres, the surface morphology was compared between reaction "on" and "off" , and the respective sample potentials were chosen according to a CV recorded in the STM set-up (*cf.* **Figure 32**a). A potential of 0 V_{Pt} was assigned to reaction "off" as the corresponding net sample current is zero. Toward negative and positive potentials, the ORR and OER occur, respectively. For the n-EC-STM measurements, multiple potentials were chosen for ORR and OER and are marked in the CV in **Figure 32**a. In the notation, the index refers to the applied potential. For example, "$OER_{0.6}$" denotes a sample potential of 0.6 V_{Pt} at which the OER occurs. Higher potentials in either direction were avoided in order not to destruct the STM tip. Besides, high OER potentials lead to oxygen bubble formation, which disengages the scanning probe from the surface.

In **Figure 32**b, an n-EC-STM measurement across a step edge on the HOPG sample is shown. During the recording, the sample potential was altered from the ORR (yellow and red lines) to reaction "off" (black) and the OER (green, blue, purple). If no reaction takes place, the height signal is stable and monitors the course of the step edge. Under ORR conditions close to the reaction onset ($ORR_{-0.3}$, yellow), spikes in the STM signal occur near the upper edge of the step. Terrace sites and sites close to the bottom of the step show no noise. Therefore, sites near the step top can be identified as active for the ORR, whereas the rest of the surface remains inactive. A potential increase ($ORR_{-0.6}$, red) does not change this overall trend. However, the noise features (height and density of the spikes) at the active sites get more pronounced. The explanation is that an increased reaction rate leads to stronger fluctuations in the tunnelling medium and thus more noise in the signal.

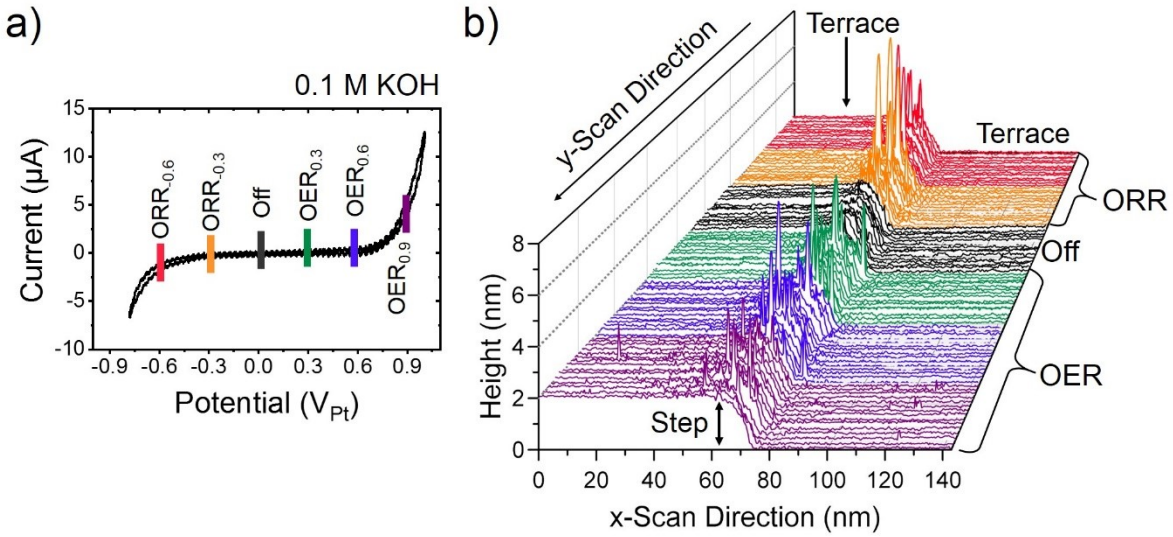

Figure 32 | n-EC-STM measurement on HOPG in 0.1 M KOH. a) A typical CV recorded in the STM set-up in air and against a Pt quasi-reference. A potential of 0 V_{Pt} without a net sample current was applied to switch the reaction "off". Towards negative and positive potentials, the ORR and OER occur, respectively. A variety of potentials for both ORR and OER was chosen during the n-EC-STM experiment as marked in the CV. b) n-EC-STM measurement across a step edge. As denoted with the colour code, the potential was varied from negative potentials where the ORR takes place (yellow, red) to reaction "off" (black) and to positive potentials where the OER occurs (green, blue, purple). Compared to reaction "off", the signal exhibits noise features (spikes) confined near the upper part of the step edge when either reaction is turned "on". The higher the respective reaction rate, the more pronounced the noise. Only for the highest potential chosen for the OER ($OER_{0.9}$, purple), also the terrace exhibits some smaller spikes. Data published in reference [277].

The application of a potential close to the onset of the OER ($OER_{0.3}$, green), on the other hand, also leads to an increase in the noise level of sites close to the top of the step edge. Again, higher potentials lead to more pronounced noise features. Noteworthy, at the highest applied potential, $OER_{0.9}$, also terrace sites exhibit some noise. The extent of the noise level is, however, lower than at the step sites. Still, the spikes in the signal show that terrace sites become involved in the OER at higher potentials. As carbon-based materials are prone to degradation during the OER[278-281], the noise could also indicate carbon corrosion. Note that in an additional n-EC-STM experiment (shown in reference [277]), after the OER, the potential was set back to the ORR region, and no changes in the surface morphology were observed. If at the highest applied OER potential, carbon corrosion would take place. This would imply the creation of defects at terrace sites, which would be active towards the ORR. Since no noise could be observed for the ORR on terrace sites after the application of the OER, defects at the terrace sites could be ruled out. It is therefore likely that the carbon surface is stable at the applied potentials, but higher potentials would presumably lead to carbon corrosion. Unfortunately, it is not possible to pinpoint the potential where this "transition" from stable to unstable behaviour occurs.

After demonstrating the viability of n-EC-STM for bifunctional catalysts in general, its outstanding resolution is promoted. Increasing the resolution requires the constant height mode with a relatively high current setpoint and scanning speed of the STM probe. Furthermore, the feedback loop is disabled for these measurements. Due to these demanding requirements, it is refrained from investigating the OER but the ORR.

Figure 33 shows high-resolution measurements for two different ORR potentials recorded at the same step edge (marked with a dotted line). The fast Fourier transform (FFT) procedure was applied to increase the noise originating from the ongoing reaction and suppress ambient noise to sharpen the image. The as-recorded data is included in reference [277]. On the step edge and the adjacent terraces, the typical honeycomb lattice of graphite can be resolved. At the potential closer to the reaction onset (-0.5 V_{Pt}), in **Figure 33**a, only a few sites near the upper part of the step edge exhibit noise features. An exemplary position is labelled "α". Due to the FFT filtering, the increased noise level (fluctuations) in the as-recorded image translates

to sites with higher STM intensity (white colour). If applying a more negative potential (-0.7 V_{Pt}), in **Figure 33**b, additional sites near the step edge appear brighter and thus become active. An example of a site, which is not active at the reaction onset and becomes activated at a more negative potential is labelled with "β". Below each figure, the line scan (height profile in scan direction) is given across the "β"-site. Their location is marked with solid black lines in the STM images. For the more negative potential, a spike in the tunnelling current can be seen at the upper step edge, which is not present at the lower "overpotential". The observation that more step sites become activated at a more negative potential could also be made for the n-EC-STM image of lower resolution (**Figure 33**). Here, however, we can pinpoint their position with down to atomic resolution. At both potentials, the terrace sites remain noise-free, which is also in line with the findings in **Figure 33**.

In summary, the measurements show that sites near step edges are active for both ORR and OER. Under a higher overpotential, more step sites become active for either reaction. For the ORR, high-resolution measurements pinpoint the active sites near the upper part of the step edge. Exclusively for the OER at the highest applied potential, the terrace sites show noise features, which are less pronounced than the ones near step sites. Other than that, terrace sites remain inactive for the ORR irrespective of the potential and the OER at lower potentials.

For the ORR, it is known that terrace sites are inactive, which is in agreement with our findings here.[282-285] For the application of carbon as support material, this would suggest that defect-free carbon is desirable. Other than terrace sites, step sites and defects were reported as active.[275, 278, 282-287] In these studies, sites near the step edge showed different binding energies toward reaction intermediates. This would explain why some sites are already active close to the reaction onset, while others require larger potentials to be activated. This assumption would require a more detailed investigation or calculation. Still, we can deduce from the atomically resolved images that the active sites are confined to a few rows of atoms at the upper edge of the steps, implying that the lower layer of graphene does not influence the activity. This could be interesting for catalysts based on lower dimensional structures like graphene and nanotubes.

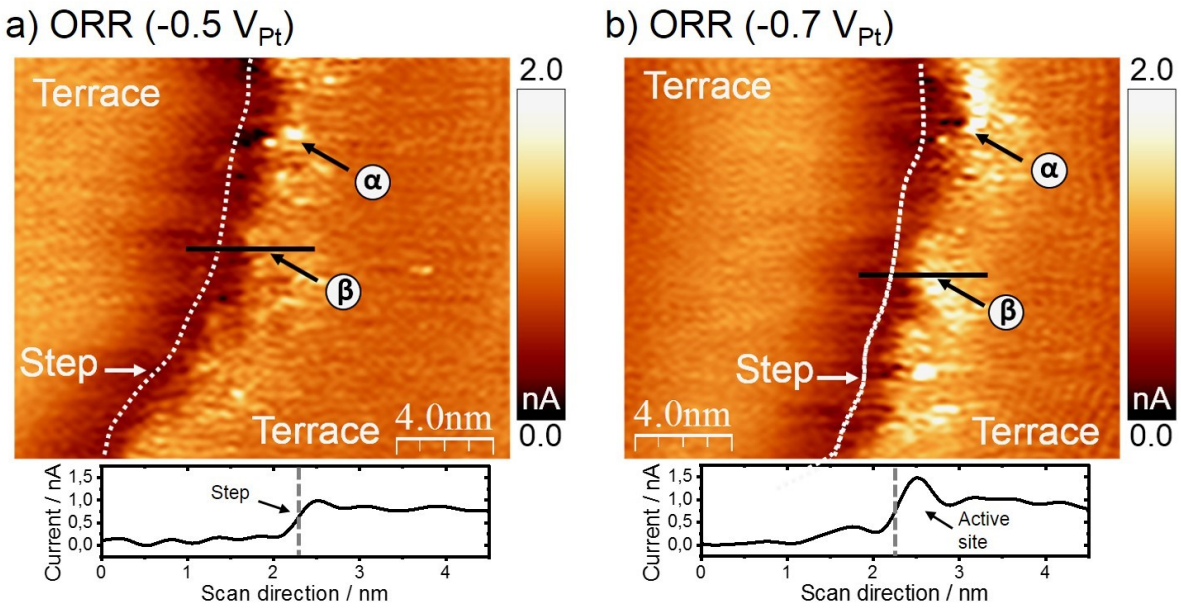

Figure 33 | High-resolution n-EC-STM for the ORR on HOPG in 0.1 M KOH. Both on the step edge (white line) and the terraces, the typical graphite honeycomb lattice can be resolved. a) Closer to the ORR onset, only some sites near the step edge exhibit noise, *e.g.* at the site "α". Since the images are FFT filtered, the increased noise level exposes as sites of high intensity (white colour). b) At a more negative potential, in addition, more step sites become active, *e.g.* at position "β". The line scan below each figure was performed across the "β"-site and its location is marked with a black solid line in each image. It shows a noise feature (current increase near the top of the step) at the more negative potential. Reprinted with permission from reference [277]. © 2021 Elsevier Ltd. All rights reserved.

The OER, on the other hand, is more complex and literature reports are vague in this aspect.[275, 288] The n-EC-STM experiments yield active step sites, which agrees with the rare literature reports.[275, 288] Terrace sites exhibit noise only at the highest applied potential. Due to the stability issues connected to the OER [278-281], this activity may be accompanied by corrosion. However, as defects are active towards the ORR[275, 278, 282-287] an increased activity should occur when going back to ORR conditions (see report in reference [277]). Since this is not the case, the surface may not be affected by the OER conditions applied in the experiments. Since stability is a vital aspect of a bifunctional catalyst, one can only assume that the carbon surface is stable until exceeding a certain potential. As the surface quality seemed unaffected, commensurate stability may apply at lower potentials. Increasing the potential further would presumably lead to carbon corrosion; the exact potential value where this "transition" happens is unfortunately not accessible with the n-EC-STM method.

After the successful application of n-EC-STM to a carbon-based model system, it can in the future be adapted to more complex (bifunctional) systems. Owing to its high resolution, active centres can be addressed in detail. An interesting group of materials are heterogeneous metal-doped carbon surfaces[274], which are at the moment subject to the n-EC-STM technique. However, the report of those measurements is beyond the scope of this thesis.

10 Conclusions

The complex, multistage reactions of the ORR and OER still show slow kinetics, even when using state-of-the-art electrocatalysts. Accordingly, their improvement is inevitable for "green" energy provision and storage systems. The OER is required as counterbalancing electron-donating reaction in water electrolysis, whereas fast ORR kinetics is paramount in efficient hydrogen fuel cells. In the particular application of metal-air batteries, so-called bifunctional catalysts are required for both the OER and ORR.[171, 289, 290] A promising route in optimising catalyst design is the identification of electrocatalytically active centres, which contribute the most to the overall activity. Knowing their nature can help in designing catalysts of specific shapes and sizes with a maximal number of active sites exposed on the surface.[25, 27-30]

In this thesis, an experimental method, termed n-EC-STM, was employed to *in-situ* assess the active centres on OER and ORR catalysts. The technique is based on observing a higher noise level of the STM signal at active relative to inactive sites. Furthermore, an approach was reported to quantify the spatially confined noise and relate it to the local activity of specific surface features.

In the first step, the n-EC-STM approach was used on amorphous IrO_x, which offers a promising compromise between good OER activity and stability. To elucidate the active areas, the extent of the noise at different surface geometry such as terrace, steps, and concavities was determined quantitatively. The ensuing outcome yielded a similar increase in noise under OER conditions. Hence, the OER shows low structure sensitivity on amorphous IrO_x. This suggests that the shape of amorphous IrO_x nanoparticles in an acidic medium should not significantly influence the OER TOF.

In the second step, the focus was set to the ORR, for which the best-performing pure material is Pt. However, Pt(111) binds the key reaction intermediates stronger than optimal.[65, 132, 152] Therefore, weakly binding sites with higher coordination, as present at concavities or the bottom of step edges, have been determined as active.[76] A well-known approach to enhance

the ORR activity is to alloy Pt with other metals. In this case, the so-called ligand and strain effects weaken the binding of the reaction species. The former stems from dissimilar atoms in the alloy bulk, which interact with the surface atoms and alter their electronic properties. The latter arises from different lattice parameters between surface and bulk.

In the case of polycrystalline alloys, the less noble metal leaches out of the surface during the electrochemical measurements, leaving behind a Pt shell. This shell is compressively strained compared to the alloyed bulk, which leads to weaker interaction with ORR intermediates and higher performance than Pt.[143] In this work, the interest was set to rare-earth metals as alloying partners to Pt. Because of their negative heat of formation in comparison to transition metals, they are expected to be potentially more stable.[158, 161, 242] In particular, n-EC-STM was applied to Pt_5Pr and Pt_5Gd in both alkaline and acidic electrolyte. In 0.1 M KOH, the outcomes are not yet conclusive enough to form a constructive statement. In 0.1 M $HClO_4$, terraces and spots near the top of step edges were identified as active. In contrast, sites near the bottom of step edges showed inferior activity. As mentioned above, this trend differs from Pt(111). A brief explanation is that Pt(111) binds chemisorbed species stronger than optimal[65, 132, 152], while terraces of the Pt-lanthanide alloys tend to bind them too weakly[143].

In addition, $Pt_3Ni(111)$ was explored due to its outstandingly high ORR activity.[148] For this model surface, it was reported that a Pt-skin is established on the Pt_3Ni bulk if the crystal is sputtered and annealed in UHV.[148] Subsequently, the atomic arrangement of the (111) surface could be visualised with LT-STM. From the images, the lattice constant could be extracted and yielded a smaller value than pure Pt(111). Hence, it is suggestive that indeed compressive strain plays an important role in the superior ORR activity of $Pt_3Ni(111)$. In a subsequent step, it was found that the defect-free, planar (111) surface is the most active. In the n-EC-STM, step sites exhibited activities ranging from inferior to comparable to terraces. A simplified clarification can be that steps of different orientations display dissimilar activities.[172] At the moment, DFT calculations are undertaken to shed light on the local activities of sites with various coordination. Preliminary results imply that terrace sites are most active, whereas step sites bind weaker and are less active.

Up to here, the investigated systems were among the best-performing classes for the respective reactions. However, they belong to the precious transition metals, which make their application costly. Capable alternatives are carbon-based materials because of their high specific surface area, electrical conductivity and economic viability.[264, 265] In an alkaline medium, they showed considerate ORR/OER activity and can thus potentially serve as bifunctional catalysts.[265, 270-276] In this study, n-EC-STM was employed on model graphite samples. Remarkably, it was possible to access the same surface area under both ORR and OER conditions with down to atomic resolution. In the experiment, steps were active for both OER and ORR. In addition, terrace sites were inactive for the ORR but exhibited noise features at higher OER potentials. After the successful use of n-EC-STM on a basic carbon-based model electrode, it can be adapted to more complex (bifunctional) catalysts in the future.[274]

In total, this work confirms the power of the n-EC-STM technique to be adaptable to various types of reactions and materials. Due to its *in-situ* functionality and its outstanding resolution, it can provide valuable guidelines in catalyst design.

11 Acknowledgements

This PhD thesis would not be complete without my sincerest gratefulness to

- Prof. **Aliaksandr Bandarenka** for supervising and supporting the experimental part of my work, for the introduction to the corresponding theoretical concepts, for improving and proofreading various reports, and for the opportunity to present my work at conferences in Germany and abroad.

- Prof. **Ifan Stephens** for being the second examiner of my thesis and for the fruitful discussions about our experimental results. I would also like to thank Prof. **Martin Zacharias** for being the head of commission.

- our collaboration partners for their contribution to this thesis and beyond. I am especially grateful to Dr. **Federico Calle-Vallejo** (University of Barcelona) for his support and for contributing DFT calculations to substantiate our experimental findings. I would like to thank Dr. **Jun Maruyama** (Osaka Research Institute) for providing us with advanced carbon samples for our n-EC-STM experiments, Prof. **Egill Skúlason**, and **André Wark** (both University of Iceland) for dedicating their DFT skills to the same project. I am grateful to Prof. **Plamen Atanassov** and Prof. **Iryna Zenyuk** (both UC Irvine), and Prof. **Frédéric Maillard** (Université Grenoble) for the discussion of certain findings and their contribution to the interpretation. I would like to thank Prof. **Julia Kunze-Liebhäuser** (Universität Innsbruck) for the friendly collaboration and the invitation to visit and work at her Chair. I am also thankful to **Andrea Auer** for making me feel welcome in Innsbruck and for preparing the stage for our joint experiments. It is such a pity that a certain pandemic disrupted our plans. I owe special thanks to our surface science collaborators from the E20 chair at TUM, Prof. **Willi Auwärter**, Prof. **Francesco Allgretti**, **Karl Eberle**, Dr. **Yang Bao**, Dr. **Alexander Riss** and Dr. **Knud Seufert**, for providing their outstanding techniques and knowledge to our joint work.

- my colleagues with whom I worked in the "Dungeon" of our STM lab. I would like to particularly thank **Richard Haid** for his expertise and his many contributions, his abilities to avoid my "difficult wordings and turns" in various manuscripts and my thesis, and for his patience in sometimes turbulent times. A big thank you goes to Dr. **Yunchang Liang** for first introducing me to the n-EC-STM technique and his help, even after his graduation. I am thankful to **Eleftherios Psaltis** for his diligent work and excellent results in his Master thesis. I thank **Thorsten Schmidt** for joining the team of us PhD students after his Master thesis, and in particular for his thoroughness in the set-up of the new device.

- the whole ECS group for numerous laughs, card games and encouraging conversations, but of course equally important, for their scientific expertise, for extensive explanations, and fruitful discussions. I am sincerely grateful for a wonderful time to Dr. **Batyr Garlyyev**, Dr. **Sebastian Watzele**, Dr. **Johannes Fichtner,** Dr. **Daniel Scieszka**, **Philipp Marzak**, Dr. **Song Xue**, **Leon Katzenmeier**, **Shujin Hou**, **Xaver Lamprecht**, **Xing Ding**, Dr. **Jeongsik Yun**, **Göktug Yesilbas**, **Kun-Ting Song, Leif Carstensen**, Dr. **Tim Lochner**, **Theophilus Sarpey**, **Jarek Sabawa**, **Peter Schneider**, **Xiaoxin Ma**, **Nina Thomsen**, Dr. **Rohit Gaddam**, Dr. **Elena Gubanova** and every single (former and current) member of the chair.

- our secretary **Manuela Ritter** for her competent and kind support in organisational matters, be it the purchase of a new device or business travel. I would like to express my gratitude to our technician **Siegfried Schreier** for the maintenance of our lab equipment and his ability to make our experimental lives easier.

- the many people who lent me a hand with the proofreading of my thesis.

- **my family**. I am grateful to be blessed with the unconditional love and support of my parents Monika & Gerhard, my brother Christian, my partner Thomas, and my parents-in-law-to-be Anita & Gerhard.

12 Appendix: Supplement to Chapter 7

For the sake of completeness, supporting information to Chapter 7, which is not implicitly necessary to understand the study's outcome, is provided in this chapter.

Typical CVs, recorded in Ar-saturated atmosphere and electrolyte against an MMS RE, are provided in **Figure A3** and agree with the literature.[9,10] For the alkaline media, no literature reference could be found.

Additionally, CVs were performed against a Pt quasi-reference in the EC-STM set-up and are shown in **Figure A3**. To perform the noise measurements, a potential of 0 mV_{Pt} was chosen for reaction "off" since the corresponding currents are low or negligible. For comparison, potentials with a notable increase in the ORR current were chosen as ORR "on". The parameters for each n-EC-STM measurement are given in **Table A1**.

Table A1 | Parameters for the n-EC-STM experiments.

	sample potential "on" (mV_{Pt})	**tip potential (mV_{Pt})**	**current set point (nA)**
Figure 25	-400	-50	1.0
Figure 26	-400	-50	2.5
Figure 27	-200	-50	3.0
Figure 28	-150	-50	4.0

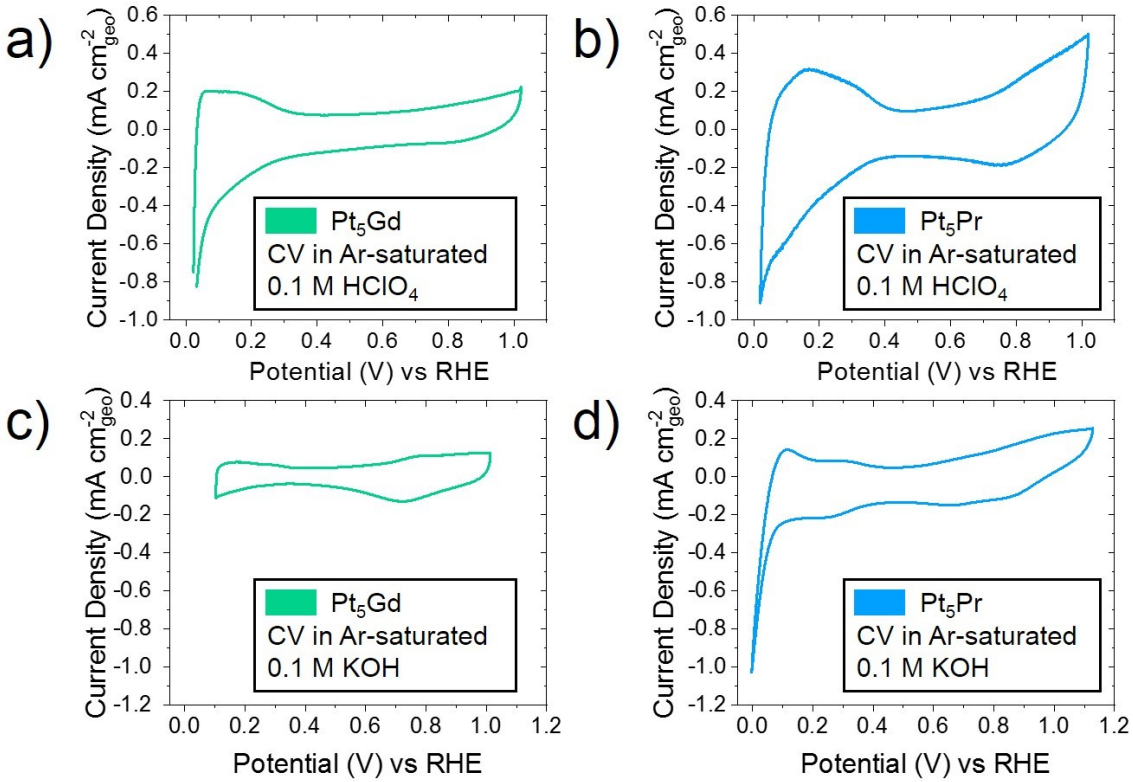

Figure A1 | Typical CVs of Pt_5Gd and Pt_5Pr electrodes performed in Ar-saturated (Argon 5.0, Westfalen, Germany) a,b) 0.1 M $HClO_4$ and c,d) 0.1 M KOH electrolytes. The scan rate was 50 mV s^{-1}.

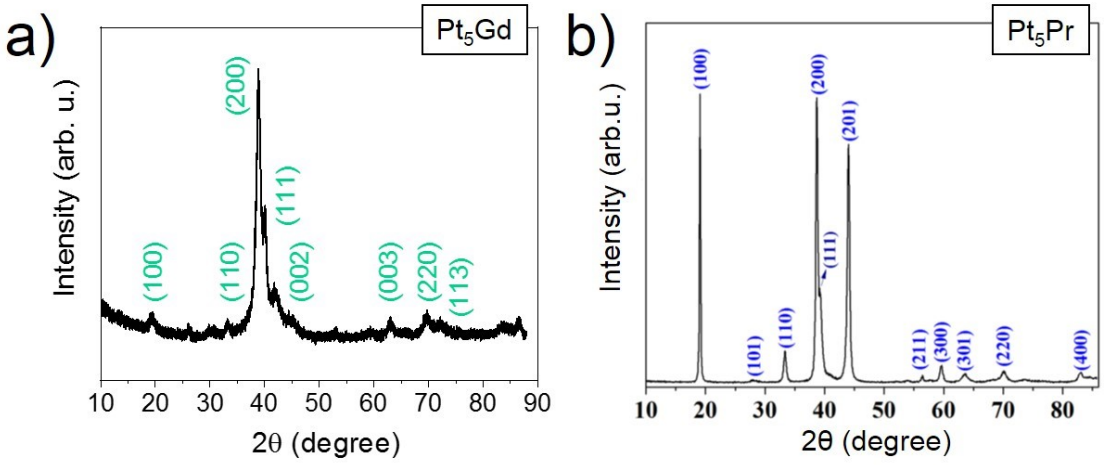

Figure A2 | XRD data of the a) Pt_5Gd and b) Pt_5Pr crystals. Figure b) is reprinted with permission from reference [243].

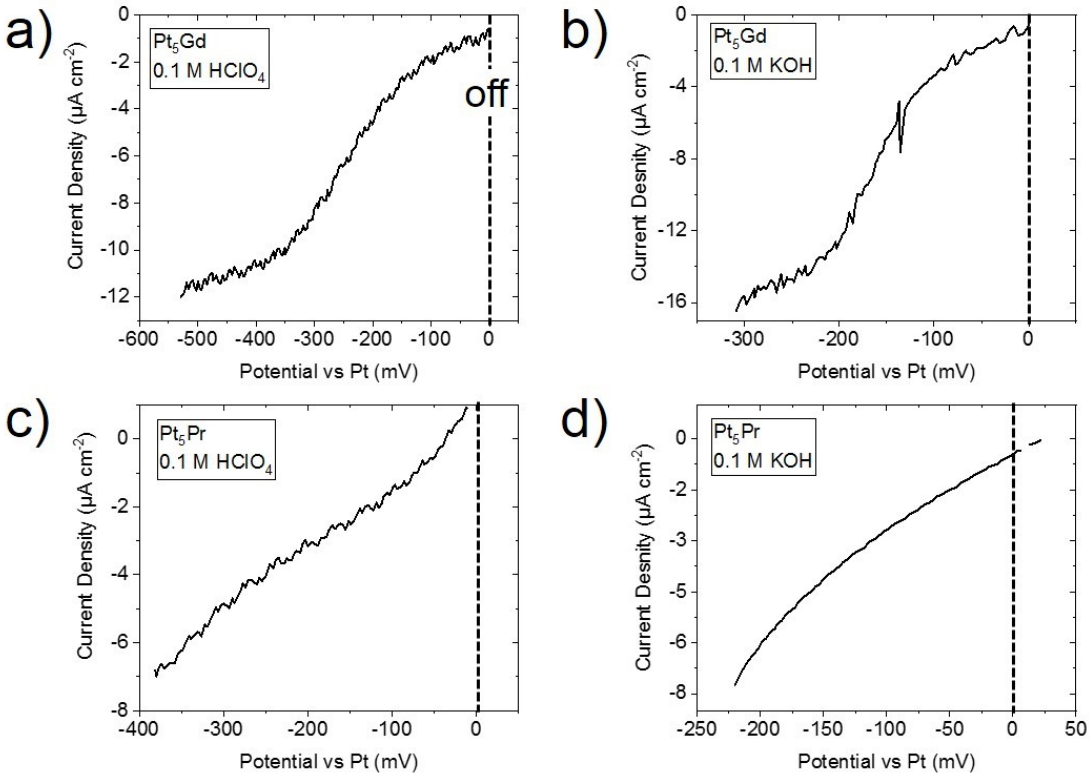

Figure A3 | CVs recorded in the EC-STM set-up *versus* a Pt-quasi reference and exposed to air. A potential of 0 mV_{Pt} was chosen as ORR "off" for all systems. The potentials applied for ORR "on" are given in **Table A1** for each n-EC-STM image.

The parameters obtained from fitting the histograms corresponding to the n-EC-STM measurements are given in **Table A2**.

Table A2 | Fitting parameters of the histograms of the n-EC-STM images on Pt-Gd and Pt-Pr. Symbols refer to ● – terrace site, ▲ – step top, and ▼ – step bottom.

		FWHM	**FWHM**	**Height**	**Height**	**reduced chi-square**	**r-square**
		value	error	value	error		
Figure 25							
	●	1.5	0.10	0.31	0.018	3.1E-04	0.95
	▲	1.3	0.11	0.32	0.020	2.9E-04	0.96
	▼	1.1	0.032	0.73	0.015	1.5E-04	1.00
Figure 26							
	●	1.50	0.11	0.24	0.01	2.2E-04	0.97
	▲	1.25	0.11	0.25	0.02	3.4E-04	0.95
	▼	0.86	0.09	0.34	0.03	7.5E-04	0.93

		FWHM	**FWHM**	**Height**	**Height**	**reduced chi-square**	**r-square**
		value	error	value	error		
Figure 27							
	●	3.22	0.35	0.21	0.02	4.4E-04	0.93
	▲	2.82	0.20	0.21	0.01	1.7E-04	0.97
	▼	1.27	0.15	0.33	0.03	1.1E-03	0.91
Figure 28							
	●	0.59	0.07	0.10	0.01	2.3E-04	0.84
	▲	0.62	0.07	0.09	0.01	1.7E-04	0.86
	▼	0.40	0.04	0.13	0.01	1.7E-04	0.90

13 References

[1] UNFCCC. Adoption of the Paris Agreement. Report No. FCCC/CP/2015/L.9/Rev.1, http://unfccc.int/resource/docs/2015/cop21/eng/l09r01.pdf (accessed on 22.03.2021).

[2] M. Z. Jacobson, M. A. Delucchi, Z. A. Bauer, S. C. Goodman, W. E. Chapman, M. A. Cameron, C. Bozonnat et al., 100% Clean and Renewable Wind, Water, and Sunlight All-Sector Energy Roadmaps for 139 Countries of the World. *Joule* **2017**, *1*, 108.

[3] Hydrogen Council. How hydrogen empowers the energy transition. https://hydrogencouncil.com/wp-content/uploads/2017/06/Hydrogen-Council-Vision-Document.pdf (accessed on 22.02.2021).

[4] International Energy Outlook 2019. https://www.eia.gov/outlooks/ieo/pdf/ieo2019.pdf (accessed on 23.03.2021).

[5] P. B. Weisz, Basic Choices and Constraints on Long-Term Energy Supplies. *Phys. Today* **2004**, *7*, 47.

[6] BP. Statistical Review of World Energy, 2019. https://www.bp.com/en/global/corporate/energy-economics/statistical-review-of-world-energy.html (accessed on 23.03.2021).

[7] R. Vakulchuk, I. Overland, D. Scholten, Renewable energy and geopolitics: A review. *Renew. Sustain. Energy Rev.* **2020**, *122*, 109547.

[8] George W. Crabtree, Mildred S. Dresselhaus, and Michelle V. Buchanan, The Hydrogen Economy. *Phys. Today* **2004**, *57*, 39.

[9] Office of Energy Efficiency & Renewable Energy, US. https://www.energy.gov/eere/fuelcells/h2scale (accessed on 23.03.2021).

[10] Toyota Homepage. https://www.toyota.de/automobile/mirai/ (accessed on 23.03.2021).

[11] Hyundai Homepage. https://www.hyundaiusa.com/us/en/vehicles/nexo (accessed on 23.03.2021).

[12] Honda Homepage. https://automobiles.honda.com/clarity-fuel-cell (accessed on 23.03.2021).

[13] Daimler Press Release. https://www.daimler.com/products/passenger-cars/mercedes-benz/glc-f-cell.html (accessed on 23.03.2021).

[14] BMW press release. https://www.bmwblog.com/2020/03/30/bmw-group-reaffirms-commitment-to-hydrogen-fuel-cell-technology/ (accessed on 23.03.2021).

[15] ADAC Report. https://www.adac.de/rund-ums-fahrzeug/autokatalog/marken-modelle/toyota/toyota-mirai/ (accessed on 23.03.2021).

[16] Tesla Homepage. https://www.tesla.com/de_DE/modelx (accessed on 23.03.2021).

[17] Universität Ulm Homepage. https://www.uni-ulm.de/in/fakultaet/in-detailseiten/news-detail/article/wasserstoff-flugzeug-hy4-erhaelt-permit-to-fly-forschung-wasserstoff-brennstoffzellen-antrieb-schon-2030-fit-fuer-40-sitzer/ (accessed on 06.07.2021).

[18] Airbus Press Release. https://www.airbus.com/newsroom/news/en/2020/10/hydrogen-fuel-cell-cross-industry-collaboration-potential-for-aviation.html (accessed on 23.03.2021).

[19] V. R. Stamenkovic, D. Strmcnik, P. P. Lopes, N. M. Markovic, Energy and fuels from electrochemical interfaces. *Nat. Mater.* **2016**, *1*, 57.

[20] W. T. Hong, M. Risch, K. A. Stoerzinger, A. Grimaud, J. Suntivich, Y. Shao-Horn, Toward the rational design of non-precious transition metal oxides for oxygen electrocatalysis. *Energy Environ. Sci.* **2015**, *5*, 1404.

[21] P. C. K. Vesborg, T. F. Jaramillo, Addressing the terawatt challenge: scalability in the supply of chemical elements for renewable energy. *RSC Adv.* **2012**, *21*, 7933.

[22] C. Chen, Y. Kang, Z. Huo, Z. Zhu, W. Huang, H. L. Xin, J. D. Snyder et al., Highly crystalline multimetallic nanoframes with three-dimensional electrocatalytic surfaces. *Science* **2014**, *6177*, 1339.

[23] C. Cui, L. Gan, H.-H. Li, S.-H. Yu, M. Heggen, P. Strasser, Octahedral PtNi nanoparticle catalysts: exceptional oxygen reduction activity by tuning the alloy particle surface composition. *Nano Lett.* **2012**, *11*, 5885.

[24] X. Huang, Z. Zhao, L. Cao, Y. Chen, E. Zhu, Z. Lin, M. Li et al., High-performance transition metal-doped Pt_3Ni octahedra for oxygen reduction reaction. *Science* **2015**, *6240*, 1230.

[25] P. Strasser, M. Gliech, S. Kuehl, T. Moeller, Electrochemical processes on solid shaped nanoparticles with defined facets. *Chem. Soc. Rev.* **2018**, *3*, 715.

[26] F. Maillard, S. Pronkin, E. R. Savinova, in *Handbook of Fuel Cells* (Eds.: W. Vielstich, A. Lamm, H. A. Gasteiger, H. Yokokawa), John Wiley & Sons, Ltd, Chichester, UK **2010**.

[27] H. S. Taylor, A theory of the catalytic surface. *Proceedings of the Royal Society of London* **1925**, *745*, 105.

[28] J. Kibsgaard, Z. Chen, B. N. Reinecke, T. F. Jaramillo, Engineering the surface structure of MoS_2 to preferentially expose active edge sites for electrocatalysis. *Nat. Mater.* **2012**, *11*, 963.

[29] B. Garlyyev, Y. Liang, S. Xue, S. Watzele, J. Fichtner, W.-J. Li, X. Ding et al., Theoretical and experimental identification of active electrocatalytic surface sites. *Curr. Opin. Electrochem.* **2019**, 206.

[30] B. Garlyyev, J. Fichtner, O. Piqué, O. Schneider, A. S. Bandarenka, F. Calle-Vallejo, Revealing the nature of active sites in electrocatalysis. *Chem. Sci.* **2019**, *35*, 8060.

[31] F. Calle-Vallejo, J. Tymoczko, V. Colic, Q. H. Vu, M. D. Pohl, K. Morgenstern, D. Loffreda et al., Finding optimal surface sites on heterogeneous catalysts by counting nearest neighbors. *Science* **2015**, *6257*, 185.

[32] Z. W. Seh, J. Kibsgaard, C. F. Dickens, I. Chorkendorff, J. K. Nørskov, T. F. Jaramillo, Combining theory and experiment in electrocatalysis: Insights into materials design. *Science* **2017**, *6321*, eaad4998.

[33] G. Rothenberg, Catalysis: Concepts and green applications, 2nd edn., *Wiley-VCH Verlag*, Weinheim **2017**.

[34] I. Chorkendorff, J. W. Niemantsverdriet, Concepts of modern catalysis and kinetics, *Wiley-VCH*, Weinheim **2017**.

[35] R. A. van Santen, Modern heterogeneous catalysis: An introduction, *Wiley-VCH Verlag*, Weinheim **2017**.

[36] G. Ertl, Reactions at surfaces: from atoms to complexity (Nobel Lecture). *Angew. Chem. Int. Ed.* **2008**, *19*, 3524.

[37] A. S. Bandarenka, E. Ventosa, A. Maljusch, J. Masa, W. Schuhmann, Techniques and methodologies in modern electrocatalysis: evaluation of activity, selectivity and stability of catalytic materials. *The Analyst* **2014**, *6*, 1274.

[38] R. C. Alkire, Electrocatalysis, *Wiley-VCH*, Weinheim, Germany **2013**.

[39] R. P. O'Hayre, F. B. Prinz, S.-W. Cha, W. G. Colella, Fuel cell fundamentals, *Wiley*, Hoboken **2016**.

[40] C. H. Hamann, A. Hamnett, W. Vielstich, Electrochemistry, 2nd edn., *Wiley-VCH*, Weinheim **2007**.

[41] J.H. Hirschenhofer, D.B. Stauffer, R.R. Engleman, and M.G. Klett, Fuel Cell Handbook, *Parsons Corporation* **1998**.

[42] K. Jiao, X. Li, Water transport in polymer electrolyte membrane fuel cells. *Prog. Energy Combust. Sci.* **2011**, *3*, 221.

[43] K. Zeng, D. Zhang, Recent progress in alkaline water electrolysis for hydrogen production and applications. *Prog. Energy Combust. Sci.* **2010**, *3*, 307.

[44] L. L. Zhang, X. S. Zhao, Carbon-based materials as supercapacitor electrodes. *Chem. Soc. Rev.* **2009**, *9*, 2520.

[45] N. Eliaz, E. Gileadi, Physical Electrochemistry: Fundamentals, Techniques and Applications, 2nd edn., *John Wiley & Sons Incorporated*, Newark **2018**.

[46] A. J. Bard, G. Inzelt, F. Scholz, Electrochemical dictionary, 2nd edn., *Springer-Verlag*, Berlin **2012**.

[47] W. Schmickler, E. Santos, Interfacial Electrochemistry, *Springer Berlin Heidelberg; Springer e-books; Imprint: Springer*, Berlin, Heidelberg **2010**.

[48] A. J. Bard, L. R. Faulkner, Electrochemical methods: Fundamentals and applications, 2nd edn., *Wiley*, Hoboken, NJ **2001**.

[49] K. R. Cooper, M. Smith, Electrical test methods for on-line fuel cell ohmic resistance measurement. *J. Power Sources* **2006**, *2*, 1088.

[50] G. Zhao, K. Rui, S. X. Dou, W. Sun, Heterostructures for Electrochemical Hydrogen Evolution Reaction: A Review. *Adv. Funct. Mater.* **2018**, *43*, 1803291.

[51] U. A. Paulus, T. J. Schmidt, H. A. Gasteiger, R. J. Behm, Oxygen reduction on a high-surface area Pt/Vulcan carbon catalyst: a thin-film rotating ring-disk electrode study. *J. Electroanal. Chem.* **2001**, *2*, 134.

[52] J. Nikolic, E. Expósito, J. Iniesta, J. González-Garcia, V. Montiel, Theoretical Concepts and Applications of a Rotating Disk Electrode. *J. Chem. Educ.* **2000**, *9*, 1191.

[53] J. M. Thomas, W. J. Thomas, Principles and practice of heterogeneous catalysis, 2nd edn., *Wiley-VCH*, Weinheim **2014**.

[54] R. W. Haid, R. M. Kluge, Y. Liang, A. S. Bandarenka, In Situ Quantification of the Local Electrocatalytic Activity via Electrochemical Scanning Tunneling Microscopy. *Small Methods* **2020**, *5*, 2000710.

[55] P. Sabatier, Hydrogénations et déshydrogénations par catalyse. *Berichte der deutschen chemischen Gesellschaft* **1911**, *3*, 1984.

[56] A. S. Bandarenka, M. T. Koper, Structural and electronic effects in heterogeneous electrocatalysis: Toward a rational design of electrocatalysts. *J. Catal.* **2013**, *308*, 11.

[57] C. Kittel, Introduction to solid state physics, 8th edn., *Wiley*, Hoboken, NJ **2005**.

[58] R. Gross, A. Marx, Festkörperphysik, 3rd edn., *De Gruyter Inc*, Berlin/Boston **2018**.

[59] M. Che, Nobel Prize in chemistry 1912 to Sabatier: Organic chemistry or catalysis? *Catal. Today* **2013**, *218-219*, 162.

[60] A. J. Medford, A. Vojvodic, J. S. Hummelshøj, J. Voss, F. Abild-Pedersen, F. Studt, T. Bligaard et al., From the Sabatier principle to a predictive theory of transition-metal heterogeneous catalysis. *J. Catal.* **2015**, *328*, 36.

[61] F. Calle-Vallejo, M. T. M. Koper, A. S. Bandarenka, Tailoring the catalytic activity of electrodes with monolayer amounts of foreign metals. *Chem. Soc. Rev.* **2013**, *12*, 5210.

[62] A. R. Zeradjanin, J.-P. Grote, G. Polymeros, K. J. J. Mayrhofer, A Critical Review on Hydrogen Evolution Electrocatalysis: Re-exploring the Volcano-relationship. *Electroanalysis* **2016**, *10*, 2256.

[63] T. Bligaard, J. K. Nørskov, S. Dahl, J. Matthiesen, C. H. Christensen, J. Sehested, The Brønsted–Evans–Polanyi relation and the volcano curve in heterogeneous catalysis. *J. Catal.* **2004**, *1*, 206.

[64] B. Hammer, J. K. Nørskov, in *Impact of Surface Science on Catalysis*, Elsevier **2000**, 71.

[65] V. Stamenkovic, B. S. Mun, K. J. J. Mayrhofer, P. N. Ross, N. M. Markovic, J. Rossmeisl, J. Greeley et al., Changing the activity of electrocatalysts for oxygen reduction by tuning the surface electronic structure. *Angew. Chem. Int. Ed.* **2006**, *18*, 2897.

[66] F. Abild-Pedersen, J. Greeley, F. Studt, J. Rossmeisl, T. R. Munter, P. G. Moses, E. Skúlason et al., Scaling properties of adsorption energies for hydrogen-containing molecules on transition-metal surfaces. *Phys. Rev. Lett.* **2007**, *1*, 16105.

[67] J. Rossmeisl, A. Logadottir, J. K. Nørskov, Electrolysis of water on (oxidized) metal surfaces. *J. Chem. Phys.* **2005**, *1-3*, 178.

[68] S. Dahl, A. Logadottir, C. J. Jacobsen, J. K. Nørskov, Electronic factors in catalysis: the volcano curve and the effect of promotion in catalytic ammonia synthesis. *Appl. Catal. A* **2001**, *1-2*, 19.

[69] N. B. Halck, V. Petrykin, P. Krtil, J. Rossmeisl, Beyond the volcano limitations in electrocatalysis - oxygen evolution reaction. *Phys. Chem. Chem. Phys.* **2014**, *27*, 13682.

[70] A. D. Doyle, J. H. Montoya, A. Vojvodic, Improving Oxygen Electrochemistry through Nanoscopic Confinement. *ChemCatChem* **2015**, *5*, 738.

[71] H. A. Hansen, J. B. Varley, A. A. Peterson, J. K. Nørskov, Understanding Trends in the Electrocatalytic Activity of Metals and Enzymes for CO_2 Reduction to CO. *J. Phys. Chem. Lett.* **2013**, *3*, 388.

[72] I. Langmuir, Part II. - “Heterogeneous reactions”. Chemical reactions on surfaces. *Trans. Faraday Soc.* **1922**, *17*, 607.

[73] M. T. M. Koper, Structure sensitivity and nanoscale effects in electrocatalysis. *Nanoscale* **2011**, *5*, 2054.

[74] R. A. van Santen, Complementary structure sensitive and insensitive catalytic relationships. *Acc. Chem. Res.* **2009**, *1*, 57.

[75] F. Calle-Vallejo, J. I. Martínez, J. M. García-Lastra, P. Sautet, D. Loffreda, Fast prediction of adsorption properties for platinum nanocatalysts with generalized coordination numbers. *Angew. Chem. Int. Ed.* **2014**, *32*, 8316.

[76] F. Calle-Vallejo, M. D. Pohl, D. Reinisch, D. Loffreda, P. Sautet, A. S. Bandarenka, Why conclusions from platinum model surfaces do not necessarily lead to enhanced nanoparticle catalysts for the oxygen reduction reaction. *Chem. Sci.* **2017**, *3*, 2283.

[77] P. Strasser, S. Koh, T. Anniyev, J. Greeley, K. More, C. Yu, Z. Liu et al., Lattice-strain control of the activity in dealloyed core-shell fuel cell catalysts. *Nat. Chem.* **2010**, *6*, 454.

[78] T. Bligaard, J. K. Nørskov, Ligand effects in heterogeneous catalysis and electrochemistry. *Electrochim. Acta* **2007**, *18*, 5512.

[79] P. Liu, J. A. Rodriguez, Catalysts for hydrogen evolution from the [NiFe] hydrogenase to the $Ni_2P(001)$ surface: the importance of ensemble effect. *J. Am. Chem. Soc.* **2005**, *42*, 14871.

[80] D. Strmcnik, K. Kodama, D. van der Vliet, J. Greeley, V. R. Stamenkovic, N. M. Marković, The role of non-covalent interactions in electrocatalytic fuel-cell reactions on platinum. *Nat. Chem.* **2009**, *6*, 466.

[81] B. Garlyyev, S. Xue, M. D. Pohl, D. Reinisch, A. S. Bandarenka, Oxygen Electroreduction at High-Index Pt Electrodes in Alkaline Electrolytes: A Decisive Role of the Alkali Metal Cations. *ACS omega* **2018**, *11*, 15325.

[82] K. Hermann and F. Rammer. Surface explorer, 2010. http://surfexp.fhi-berlin.mpg.de/ (last assessed: 10.03.2021).

[83] N. Arulmozhi, G. Jerkiewicz, Design and Development of Instrumentations for the Preparation of Platinum Single Crystals for Electrochemistry and Electrocatalysis Research. Part 2: Orientation, Cutting, and Annealing. *Electrocatalysis* **2017**, *5*, 399.

[84] G. Guisbiers, G. Abudukelimu, Influence of nanomorphology on the melting and catalytic properties of convex polyhedral nanoparticles. *J Nanopart Res* **2013**, *15*, 1431.

[85] T. Lochner, R. M. Kluge, J. Fichtner, H. A. El-Sayed, B. Garlyyev, A. S. Bandarenka, Temperature Effects in Polymer Electrolyte Membrane Fuel Cells. *ChemElectroChem* **2020**, *17*, 3545.

[86] J. Macedo-Valencia, J. M. Sierra, S. J. Figueroa-Ramírez, S. E. Díaz, M. Meza, 3D CFD modeling of a PEM fuel cell stack. *Int. J. Hydrog. Energy* **2016**, *48*, 23425.

[87] H. Dau, C. Limberg, T. Reier, M. Risch, S. Roggan, P. Strasser, The Mechanism of Water Oxidation: From Electrolysis via Homogeneous to Biological Catalysis. *ChemCatChem* **2010**, *7*, 724.

[88] B. E. Conway, B. V. Tilak, Interfacial processes involving electrocatalytic evolution and oxidation of H_2, and the role of chemisorbed H. *Electrochim. Acta* **2002**, *22-23*, 3571.

[89] N. Danilovic, R. Subbaraman, D. Strmcnik, V. Stamenkovic, N. Markovic, Electrocatalysis of the HER in acid and alkaline media. *J. Serb. Chem. Soc.* **2013**, *12*, 2007.

[90] J. O. Bockris, E. C. Potter, The Mechanism of the Cathodic Hydrogen Evolution Reaction. *J. Electrochem. Soc.* **1952**, *4*, 169.

[91] S. Trasatti, Work function, electronegativity, and electrochemical behaviour of metals. *J. Electroanal. Chem.* **1972**, *1*, 163.

[92] W. KREUTER, Electrolysis: The important energy transformer in a world of sustainable energy. *Int. J. Hydrog. Energy* **1998**, *8*, 661.

[93] D. M. F. Santos, C. A. C. Sequeira, J. L. Figueiredo, Hydrogen production by alkaline water electrolysis. *Quím. Nova* **2013**, *8*, 1176.

[94] C. G. Morales-Guio, L.-A. Stern, X. Hu, Nanostructured hydrotreating catalysts for electrochemical hydrogen evolution. *Chem. Soc. Rev.* **2014**, *18*, 6555.

[95] M. Zeng, Y. Li, Recent advances in heterogeneous electrocatalysts for the hydrogen evolution reaction. *J. Mater. Chem. A* **2015**, *29*, 14942.

[96] W. Sheng, H. A. Gasteiger, Y. Shao-Horn, Hydrogen Oxidation and Evolution Reaction Kinetics on Platinum: Acid vs Alkaline Electrolytes. *J. Electrochem. Soc.* **2010**, *11*, B1529.

[97] J. Zheng, W. Sheng, Z. Zhuang, B. Xu, Y. Yan, Universal dependence of hydrogen oxidation and evolution reaction activity of platinum-group metals on pH and hydrogen binding energy. *Sci. Adv.* **2016**, *3*, e1501602.

[98] J. Durst, A. Siebel, C. Simon, F. Hasché, J. Herranz, H. A. Gasteiger, New insights into the electrochemical hydrogen oxidation and evolution reaction mechanism. *Energy Environ. Sci.* **2014**, *7*, 2255.

[99] T. Bhowmik, M. K. Kundu, S. Barman, Palladium Nanoparticle–Graphitic Carbon Nitride Porous Synergistic Catalyst for Hydrogen Evolution/Oxidation Reactions over a Broad Range of pH and Correlation of Its Catalytic Activity with Measured Hydrogen Binding Energy. *ACS Catal.* **2016**, *3*, 1929.

[100] H. A. Gasteiger, J. E. Panels, S. G. Yan, Dependence of PEM fuel cell performance on catalyst loading. *J. Power Sources* **2004**, *1-2*, 162.

[101] K. C. Neyerlin, W. Gu, J. Jorne, H. A. Gasteiger, Study of the Exchange Current Density for the Hydrogen Oxidation and Evolution Reactions. *J. Electrochem. Soc.* **2007**, *7*, B631.

[102] P. Liu, J. K. Nørskov, Kinetics of the Anode Processes in PEM Fuel Cells - The Promoting Effect of Ru in PtRu Anodes. *Fuel Cells* **2001**, *3-4*, 192.

[103] A. Serov, C. Kwak, Review of non-platinum anode catalysts for DMFC and PEMFC application. *Appl. Catal. B* **2009**, *3-4*, 313.

[104] J. O. Bockris, Kinetics of Activation Controlled Consecutive Electrochemical Reactions: Anodic Evolution of Oxygen. *J. Chem. Phys.* **1956**, *24 (4).* 4, 817.

[105] I. C. Man, H.-Y. Su, F. Calle-Vallejo, H. A. Hansen, J. I. Martínez, N. G. Inoglu, J. Kitchin et al., Universality in Oxygen Evolution Electrocatalysis on Oxide Surfaces. *ChemCatChem* **2011**, *7*, 1159.

[106] J. Rossmeisl, Z.-W. Qu, H. Zhu, G.-J. Kroes, J. K. Nørskov, Electrolysis of water on oxide surfaces. *J. Electroanal. Chem.* **2007**, *1-2*, 83.

[107] H. G. Sanchez Casalongue, M. L. Ng, S. Kaya, D. Friebel, H. Ogasawara, A. Nilsson, In situ observation of surface species on iridium oxide nanoparticles during the oxygen evolution reaction. *Angewandte Chemie* **2014**, *28*, 7169.

[108] J. Song, C. Wei, Z.-F. Huang, C. Liu, L. Zeng, X. Wang, Z. J. Xu, A review on fundamentals for designing oxygen evolution electrocatalysts. *Chem. Soc. Rev.* **2020**, *7*, 2196.

[109] M. Pourbaix, Atlas of electrochemical equilibria in aqueous solutions, 2nd edn., *National Association of Corrosion Engineers*, Houston, Tex. **1974**.

[110] S. Hackwood, L. M. Schiavone, W. C. Dautremont-Smith, G. Beni, Anodic Evolution of Oxygen on Sputtered Iridium Oxide Films. *J. Electrochem. Soc.* **1981**, *12*, 2569.

[111] B. Johnson, F. Girgsdies, G. Weinberg, D. Rosenthal, A. Knop-Gericke, R. Schlögl, T. Reier et al., Suitability of Simplified (Ir,Ti)O_x Films for Characterization during Electrocatalytic Oxygen Evolution Reaction. *J. Phys. Chem. C* **2013**, *48*, 25443.

[112] M. Bernicke, E. Ortel, T. Reier, A. Bergmann, J. Ferreira de Araujo, P. Strasser, R. Kraehnert, Iridium Oxide Coatings with Templated Porosity as Highly Active Oxygen Evolution Catalysts: Structure-Activity Relationships. *ChemSusChem* **2015**, *11*, 1908.

[113] T. Reier, D. Teschner, T. Lunkenbein, A. Bergmann, S. Selve, R. Kraehnert, R. Schlögl et al., Electrocatalytic Oxygen Evolution on Iridium Oxide: Uncovering Catalyst-Substrate Interactions and Active Iridium Oxide Species. *J. Electrochem. Soc.* **2014**, *9*, F876-F882.

[114] N. Danilovic, R. Subbaraman, K.-C. Chang, S. H. Chang, Y. J. Kang, J. Snyder, A. P. Paulikas et al., Activity-Stability Trends for the Oxygen Evolution Reaction on Monometallic Oxides in Acidic Environments. *J. Phys. Chem. Lett.* **2014**, *14*, 2474.

[115] L. Ouattara, S. Fierro, O. Frey, M. Koudelka, C. Comninellis, Electrochemical comparison of IrO_2 prepared by anodic oxidation of pure iridium and IrO_2 prepared by thermal decomposition of H_2IrCl_6 precursor solution. *J Appl Electrochem* **2009**, *8*, 1361.

[116] T. Binninger, R. Mohamed, K. Waltar, E. Fabbri, P. Levecque, R. Kötz, T. J. Schmidt, Thermodynamic explanation of the universal correlation between oxygen evolution activity and corrosion of oxide catalysts. *Sci. Rep.* **2015**, *5*, 12167.

[117] S. Cherevko, S. Geiger, O. Kasian, A. Mingers, K. J. Mayrhofer, Oxygen evolution activity and stability of iridium in acidic media. Part 2. – Electrochemically grown hydrous iridium oxide. *J. Electroanal. Chem.* **2016**, *774*, 102.

[118] O. Kasian, J.-P. Grote, S. Geiger, S. Cherevko, K. J. J. Mayrhofer, The Common Intermediates of Oxygen Evolution and Dissolution Reactions during Water Electrolysis on Iridium. *Angewandte Chemie* **2018**, *9*, 2488.

[119] J. D. E. McIntyre, S. Basu, W. F. Peck, W. L. Brown, W. M. Augustyniak, Cation insertion reactions of electrochromic tungsten and iridium oxide films. *Phys. Rev. B* **1982**, *12*, 7242.

[120] A. Minguzzi, C. Locatelli, O. Lugaresi, E. Achilli, G. Cappelletti, M. Scavini, M. Coduri et al., Easy Accommodation of Different Oxidation States in Iridium Oxide Nanoparticles with Different Hydration Degree as Water Oxidation Electrocatalysts. *ACS Catal.* **2015**, *9*, 5104.

[121] A. Damjanovic, A. Dey, J. Bockris, Kinetics of oxygen evolution and dissolution on platinum electrodes. *Electrochim. Acta* **1966**, *7*, 791.

[122] N. N. Greenwood, A. Earnshaw, Chemistry of the elements, 2nd edn., *Elsevier Butterworth-Heinemann*, Amsterdam, Oxford **1997**.

[123] C. Massué, V. Pfeifer, M. van Gastel, J. Noack, G. Algara-Siller, S. Cap, R. Schlögl, Reactive Electrophilic OI- Species Evidenced in High-Performance Iridium Oxohydroxide Water Oxidation Electrocatalysts. *ChemSusChem* **2017**, *23*, 4786.

[124] V. Pfeifer, T. E. Jones, J. J. Velasco Vélez, C. Massué, M. T. Greiner, R. Arrigo, D. Teschner et al., The electronic structure of iridium oxide electrodes active in water splitting. *Phys. Chem. Chem. Phys.* **2016**, *4*, 2292.

[125] V. Pfeifer, T. E. Jones, S. Wrabetz, C. Massué, J. J. Velasco Vélez, R. Arrigo, M. Scherzer et al., Reactive oxygen species in iridium-based OER catalysts. *Chem. Sci.* **2016**, *11*, 6791.

[126] M. Scohy, S. Abbou, V. Martin, B. Gilles, E. Sibert, L. Dubau, F. Maillard, Probing Surface Oxide Formation and Dissolution on/of Ir Single Crystals via X-ray Photoelectron Spectroscopy and Inductively Coupled Plasma Mass Spectrometry. *ACS Catal.* **2019**, *11*, 9859.

[127] C. Spöri, P. Briois, H. N. Nong, T. Reier, A. Billard, S. Kühl, D. Teschner et al., Experimental Activity Descriptors for Iridium-Based Catalysts for the Electrochemical Oxygen Evolution Reaction (OER). *ACS Catal.* **2019**, *8*, 6653.

[128] H. S. Wroblowa, Yen-Chi-Pan, G. Razumney, Electroreduction of oxygen. *J. Electroanal. Chem.* **1976**, *2*, 195.

[129] J. R. Kitchin, J. K. Nørskov, M. A. Barteau, J. G. Chen, Modification of the surface electronic and chemical properties of Pt(111) by subsurface 3d transition metals. *J. Chem. Phys.* **2004**, *21*, 10240.

[130] Y. Bing, H. Liu, L. Zhang, D. Ghosh, J. Zhang, Nanostructured Pt-alloy electrocatalysts for PEM fuel cell oxygen reduction reaction. *Chem. Soc. Rev.* **2010**, *6*, 2184.

[131] G. Ertl (Ed.), Handbook of heterogeneous catalysis: *volume 8*, *Wiley-VCH-Verl.*, Weinheim **1997**.

[132] J. K. Nørskov, J. Rossmeisl, A. Logadottir, L. Lindqvist, J. R. Kitchin, T. Bligaard, H. Jónsson, Origin of the Overpotential for Oxygen Reduction at a Fuel-Cell Cathode. *J. Phys. Chem. B* **2004**, *46*, 17886.

[133] A. M. Gómez-Marín, R. Rizo, J. M. Feliu, Some reflections on the understanding of the oxygen reduction reaction at Pt(111). *Beilstein J. Nanotechnol.* **2013**, 956.

[134] I. E. L. Stephens, A. S. Bondarenko, F. J. Perez-Alonso, F. Calle-Vallejo, L. Bech, T. P. Johansson, A. K. Jepsen et al., Tuning the activity of Pt(111) for oxygen electroreduction by subsurface alloying. *J. Am. Chem. Soc.* **2011**, *14*, 5485.

[135] N. M. Marković, T. J. Schmidt, V. Stamenković, P. N. Ross, Oxygen Reduction Reaction on Pt and Pt Bimetallic Surfaces: A Selective Review. *Fuel Cells* **2001**, *2*, 105.

[136] N. Markovic, P. N. Ross, Surface science studies of model fuel cell electrocatalysts. *Surf. Sci. Rep.* **2002**, *4-6*, 117.

[137] V. Colic, M. D. Pohl, D. Scieszka, A. S. Bandarenka, Influence of the electrolyte composition on the activity and selectivity of electrocatalytic centers. *Catal. Today* **2016**, *262*, 24.

[138] N. M. Marković, R. R. Adžić, B. D. Cahan, E. B. Yeager, Structural effects in electrocatalysis: oxygen reduction on platinum low index single-crystal surfaces in perchloric acid solutions. *J. Electroanal. Chem.* **1994**, *1-2*, 249.

[139] M. D. Maciá, J. M. Campiña, E. Herrero, J. M. Feliu, On the kinetics of oxygen reduction on platinum stepped surfaces in acidic media. *J. Electroanal. Chem.* **2004**, *564*, 141.

[140] A. Kuzume, E. Herrero, J. M. Feliu, Oxygen reduction on stepped platinum surfaces in acidic media. *J. Electroanal. Chem.* **2007**, *2*, 333.

[141] A. M. Gómez-Marín, J. M. Feliu, Oxygen reduction on nanostructured platinum surfaces in acidic media: Promoting effect of surface steps and ideal response of Pt(111). *Catal. Today* **2015**, *244*, 172.

[142] A. Hitotsuyanagi, M. Nakamura, N. Hoshi, Structural effects on the activity for the oxygen reduction reaction on n(111)–(100) series of Pt: correlation with the oxide film formation. *Electrochim. Acta* **2012**, *82*, 512.

[143] V. Čolić, A. S. Bandarenka, Pt Alloy Electrocatalysts for the Oxygen Reduction Reaction: From Model Surfaces to Nanostructured Systems. *ACS Catal.* **2016**, *8*, 5378.

[144] T. Yu, D. Y. Kim, H. Zhang, Y. Xia, Platinum Concave Nanocubes with High-Index Facets and Their Enhanced Activity for Oxygen Reduction Reaction. *Angew. Chem. Int. Ed.* **2011**, *12*, 2825.

[145] J. Fichtner, S. Watzele, B. Garlyyev, R. M. Kluge, F. Haimerl, H. A. El-Sayed, W.-J. Li et al., Tailoring the Oxygen Reduction Activity of Pt Nanoparticles through Surface Defects: A Simple Top-Down Approach. *ACS Catal.* **2020**, *5*, 3131.

[146] R. Chattot, T. Asset, P. Bordet, J. Drnec, L. Dubau, F. Maillard, Beyond Strain and Ligand Effects: Microstrain-Induced Enhancement of the Oxygen Reduction Reaction Kinetics on Various PtNi/C Nanostructures. *ACS Catal.* **2017**, *1*, 398.

[147] L. Gan, C. Cui, M. Heggen, F. Dionigi, S. Rudi, P. Strasser, Element-specific anisotropic growth of shaped platinum alloy nanocrystals. *Science* **2014**, *6216*, 1502.

[148] V. R. Stamenkovic, B. Fowler, B. S. Mun, G. Wang, P. N. Ross, C. A. Lucas, N. M. Marković, Improved oxygen reduction activity on $Pt_3Ni(111)$ via increased surface site availability. *Science* **2007**, *5811*, 493.

[149] J. Kibsgaard, Y. Gorlin, Z. Chen, T. F. Jaramillo, Meso-structured platinum thin films: active and stable electrocatalysts for the oxygen reduction reaction. *J. Am. Chem. Soc.* **2012**, *18*, 7758.

[150] L. Dubau, M. Lopez-Haro, J. Durst, L. Guétaz, P. Bayle-Guillemaud, M. Chatenet, F. Maillard, Beyond conventional electrocatalysts: Hollow nanoparticles for improved and sustainable oxygen reduction reaction activity. *J. Mater. Chem. A* **2014**, *43*, 18497.

[151] J. H. K. Pfisterer, Y. Liang, O. Schneider, A. S. Bandarenka, Direct instrumental identification of catalytically active surface sites. *Nature* **2017**, *7670*, 74.

[152] J. Greeley, I. E. L. Stephens, A. S. Bondarenko, T. P. Johansson, H. A. Hansen, T. F. Jaramillo, J. Rossmeisl et al., Alloys of platinum and early transition metals as oxygen reduction electrocatalysts. *Nat. Chem.* **2009**, *7*, 552.

[153] R. Rizo, E. Herrero, J. M. Feliu, Oxygen reduction reaction on stepped platinum surfaces in alkaline media. *Phys. Chem. Chem. Phys.* **2013**, *37*, 15416.

[154] Y. Liang, D. McLaughlin, C. Csoklich, O. Schneider, A. S. Bandarenka, The nature of active centers catalyzing oxygen electro-reduction at platinum surfaces in alkaline media. *Energy Environ. Sci.* **2019**, *1*, 351.

[155] M. Escudero-Escribano, P. Malacrida, M. H. Hansen, U. G. Vej-Hansen, A. Velázquez-Palenzuela, V. Tripkovic, J. Schiøtz et al., Tuning the activity of Pt alloy electrocatalysts by means of the lanthanide contraction. *Science* **2016**, *6281*, 73.

[156] M. Liu, Z. Zhao, X. Duan, Y. Huang, Nanoscale Structure Design for High-Performance Pt-Based ORR Catalysts. *Adv. Mater.* **2019**, *6*, e1802234.

[157] J. Fichtner, B. Garlyyev, S. Watzele, H. A. El-Sayed, J. N. Schwämmlein, W.-J. Li, F. M. Maillard et al., Top-Down Synthesis of Nanostructured Platinum-Lanthanide Alloy Oxygen Reduction Reaction Catalysts: Pt_xPr/C as an Example. *ACS Appl. Mater. Interfaces* **2019**, *5*, 5129.

[158] M. Escudero-Escribano, A. Verdaguer-Casadevall, P. Malacrida, U. Grønbjerg, B. P. Knudsen, A. K. Jepsen, J. Rossmeisl et al., Pt_5Gd as a highly active and stable catalyst for oxygen electroreduction. *J. Am. Chem. Soc.* **2012**, *40*, 16476.

[159] S. Mi, N. Cheng, H. Jiang, C. Li, H. Jiang, Porous Pt_3Ni with enhanced activity and durability towards oxygen reduction reaction. *RSC Adv.* **2018**, *28*, 15344.

[160] X. Tian, X. Zhao, Y.-Q. Su, L. Wang, H. Wang, D. Dang, B. Chi et al., Engineering bunched Pt-Ni alloy nanocages for efficient oxygen reduction in practical fuel cells. *Science* **2019**, *6467*, 850.

[161] P. Malacrida, M. Escudero-Escribano, A. Verdaguer-Casadevall, I. E. L. Stephens, I. Chorkendorff, Enhanced activity and stability of Pt–La and Pt–Ce alloys for oxygen electroreduction: the elucidation of the active surface phase. *J. Mater. Chem. A* **2014**, *12*, 4234.

[162] U. G. Vej-Hansen, M. Escudero-Escribano, A. Velázquez-Palenzuela, P. Malacrida, J. Rossmeisl, I. E. L. Stephens, I. Chorkendorff et al., New Platinum Alloy Catalysts for Oxygen Electroreduction Based on Alkaline Earth Metals. *Electrocatalysis* **2017**, *6*, 594.

[163] Y.-J. Wang, N. Zhao, B. Fang, H. Li, X. T. Bi, H. Wang, Carbon-supported Pt-based alloy electrocatalysts for the oxygen reduction reaction in polymer electrolyte membrane fuel cells: particle size, shape, and composition manipulation and their impact to activity. *Chem. Rev.* **2015**, *9*, 3433.

[164] F. Maroun, F. Ozanam, O. M. Magnussen, R. J. Behm, The role of atomic ensembles in the reactivity of bimetallic electrocatalysts. *Science* **2001**, *5536*, 1811.

[165] Q. Jia, W. Liang, M. K. Bates, P. Mani, W. Lee, S. Mukerjee, Activity descriptor identification for oxygen reduction on platinum-based bimetallic nanoparticles: in situ observation of the linear composition-strain-activity relationship. *ACS nano* **2015**, *1*, 387.

[166] I. E. L. Stephens, A. S. Bondarenko, U. Grønbjerg, J. Rossmeisl, I. Chorkendorff, Understanding the electrocatalysis of oxygen reduction on platinum and its alloys. *Energy Environ. Sci.* **2012**, *5*, 6744.

[167] C. Wang, M. Chi, D. Li, D. Strmcnik, D. van der Vliet, G. Wang, V. Komanicky et al., Design and synthesis of bimetallic electrocatalyst with multilayered Pt-skin surfaces. *J. Am. Chem. Soc.* **2011**, *36*, 14396.

[168] Z. Duan, G. Wang, A first principles study of oxygen reduction reaction on a Pt(111) surface modified by a subsurface transition metal M (M = Ni, Co, or Fe). *Phys. Chem. Chem. Phys.* **2011**, *45*, 20178.

[169] S. Kattel, G. Wang, Beneficial compressive strain for oxygen reduction reaction on Pt (111) surface. *J. Chem. Phys.* **2014**, *12*, 124713.

[170] T.-Y. Jeon, S. J. Yoo, Y.-H. Cho, K.-S. Lee, S. H. Kang, Y.-E. Sung, Influence of Oxide on the Oxygen Reduction Reaction of Carbon-Supported Pt−Ni Alloy Nanoparticles. *J. Phys. Chem. C* **2009**, *45*, 19732.

[171] A. S. Aricò, P. Bruce, B. Scrosati, J.-M. Tarascon, W. van Schalkwijk, in *Materials for Sustainable Energy* (Ed.: V. Dusastre), Co-Published with Macmillan Publishers Ltd, UK **2010**, 148.

[172] T. Rurigaki, A. Hitotsuyanagi, M. Nakamura, N. Sakai, N. Hoshi, Structural effects on the oxygen reduction reaction on the high index planes of Pt_3Ni: *n*(111)–(111) and *n*(111)–(100) surfaces. *J. Electroanal. Chem.* **2014**, 58.

[173] J. Erlebacher, M. J. Aziz, A. Karma, N. Dimitrov, K. Sieradzki, Evolution of nanoporosity in dealloying. *Nature* **2001**, *6827*, 450.

[174] T. P. Moffat, F.-R. F. Fan, A. J. Bard, Electrochemical and Scanning Tunneling Microscopic Study of Dealloying of Cu_3Au. *J. Electrochem. Soc.* **1991**, *11*, 3224.

[175] I. E. L. Stephens, A. S. Bondarenko, L. Bech, I. Chorkendorff, Oxygen Electroreduction Activity and X-Ray Photoelectron Spectroscopy of Platinum and Early Transition Metal Alloys. *ChemCatChem* **2012**, *3*, 341.

[176] M. Shao, J. H. Odell, A. Peles, D. Su, The role of transition metals in the catalytic activity of Pt alloys: quantification of strain and ligand effects. *Chem. Commun.* **2014**, *17*, 2173.

[177] A. Schlapka, M. Lischka, A. Gross, U. Käsberger, P. Jakob, Surface strain versus substrate interaction in heteroepitaxial metal layers: Pt on Ru(0001). *Phys. Rev. Lett.* **2003**, *1*, 16101.

[178] E. T. Ulrikkeholm, A. F. Pedersen, U. G. Vej-Hansen, M. Escudero-Escribano, I. E. Stephens, D. Friebel, A. Mehta et al., Pt Gd alloy formation on Pt(111): Preparation and structural characterization. *Surf. Sci.* **2016**, *652*, 114.

[179] A. S. Bandarenka, H. A. Hansen, J. Rossmeisl, I. E. L. Stephens, Elucidating the activity of stepped Pt single crystals for oxygen reduction. *Phys. Chem. Chem. Phys.* **2014**, *27*, 13625.

[180] J. Tymoczko, F. Calle-Vallejo, V. Čolić, W. Schuhmann, A. S. Bandarenka, Evaluation of the Electrochemical Stability of Model Cu-Pt(111) Near-Surface Alloy Catalysts. *Electrochimica Acta* **2015**, 469.

[181] M. Shao, Q. Chang, J.-P. Dodelet, R. Chenitz, Recent Advances in Electrocatalysts for Oxygen Reduction Reaction. *Chem. Rev.* **2016**, *6*, 3594.

[182] S. Xu, Y. Kim, D. Higgins, M. Yusuf, T. F. Jaramillo, F. B. Prinz, Building upon the Koutecky-Levich Equation for Evaluation of Next-Generation Oxygen Reduction Reaction Catalysts. *Electrochim. Acta* **2017**, *255*, 99.

[183] K. J. J. Mayrhofer, D. Strmcnik, B. B. Blizanac, V. R. Stamenkovic, M. Arenz, N. M. Markovic, Measurement of oxygen reduction activities via the rotating disc electrode method: From Pt model surfaces to carbon-supported high surface area catalysts. *Electrochim. Acta* **2008**, *7*, 3181.

[184] G. Binnig, H. Rohrer, C. Gerber, E. Weibel, Surface Studies by Scanning Tunneling Microscopy. *Phys. Rev. Lett.* **1982**, *1*, 57.

[185] G. Binnig, H. Rohrer, Scanning tunneling microscopy. *Surf. Sci.* **1983**, *1-3*, 236.

[186] Press Release. Nobel Media. https://www.nobelprize.org/prizes/physics/1986/press-release (accessed on 19.10.2020).

[187] E. Meyer, H. J. Hug, R. Bennewitz, Scanning Probe Microscopy: The Lab on a Tip, *Springer Berlin Heidelberg*, Berlin, Heidelberg **2004**.

[188] Veeco Corporate Headquarters, A Practical Guide to SPM: Scanning Probe Microscopy **2005**.

[189] I. Horcas, R. Fernández, J. M. Gómez-Rodríguez, J. Colchero, J. Gómez-Herrero, A. M. Baro, WSXM: a software for scanning probe microscopy and a tool for nanotechnology. *Rev. Sci. Instrum.* **2007**, *1*, 13705.

[190] S. Hunklinger, Festkörperphysik, *Oldenbourg Wissenschaftsverlag* **2009**.

[191] H. Y. Liu, F. R. F. Fan, C. W. Lin, A. J. Bard, Scanning electrochemical and tunneling ultramicroelectrode microscope for high-resolution examination of electrode surfaces in solution. *J. Am. Chem. Soc.* **1986**, *13*, 3838.

[192] K. Itaya, E. Tomita, Scanning tunneling microscope for electrochemistry - a new concept for the in situ scanning tunneling microscope in electrolyte solutions. *Surf. Sci.* **1988**, *3*, L507-L512.

[193] Y. Liang, J. H. K. Pfisterer, D. McLaughlin, C. Csoklich, L. Seidl, A. S. Bandarenka, O. Schneider, Electrochemical Scanning Probe Microscopies in Electrocatalysis. *Small Methods* **2019**, *8*, 1800387.

[194] J. Halbritter, G. Repphun, S. Vinzelberg, G. Staikov, W. J. Lorenz, Tunneling mechanisms in electrochemical STM —distance and voltage tunneling spectroscopy. *Electrochim. Acta* **1995**, *10*, 1385.

[195] L. A. Kibler, A. M. El-Aziz, R. Hoyer, D. M. Kolb, Tuning reaction rates by lateral strain in a palladium monolayer. *Angew. Chem. Int. Ed.* **2005**, *14*, 2080.

[196] J. Kunze, V. Maurice, L. H. Klein, H.-H. Strehblow, P. Marcus, In situ STM study of the duplex passive films formed on Cu(111) and Cu(001) in 0.1 M NaOH. *Corro. Sci.* **2004**, *1*, 245.

[197] A. Auer, M. Andersen, E.-M. Wernig, N. G. Hörmann, N. Buller, K. Reuter, J. Kunze-Liebhäuser, Self-activation of copper electrodes during CO electro-oxidation in alkaline electrolyte. *Nat Catal* **2020**, *10*, 797.

[198] R. Wen, B. Rahn, O. M. Magnussen, In Situ Video-STM Study of Adlayer Structure and Surface Dynamics at the Ionic Liquid/Au (111) Interface. *J. Phys. Chem. C* **2016**, *29*, 15765.

[199] M. Wakisaka, T. Yoneyama, S. Ashizawa, Y. Hyuga, T. Ohkanda, H. Uchida, M. Watanabe, Structural variations of CO adlayers on a Pt(100) electrode in 0.1 M $HClO_4$ solution: an in situ STM study. *Phys. Chem. Chem. Phys.* **2013**, *26*, 11038.

[200] L. A. Nagahara, T. Thundat, S. M. Lindsay, Preparation and characterization of STM tips for electrochemical studies. *Rev. Sci. Instrum.* **1989**, *60*, 3128.

[201] A. Auer, J. Kunze-Liebhäuser, A universal quasi-reference electrode for in situ EC-STM. *Electrochem. Commun.* **2019**, *98*, 15.

[202] Y. Liang, C. Csoklich, D. McLaughlin, O. Schneider, A. S. Bandarenka, Revealing Active Sites for Hydrogen Evolution at Pt and Pd Atomic Layers on Au Surfaces. *ACS Appl. Mater. Interfaces* **2019**, *13*, 12476.

[203] E. Mitterreiter, Y. Liang, M. Golibrzuch, D. McLaughlin, C. Csoklich, J. D. Bartl, A. Holleitner et al., In-situ visualization of hydrogen evolution sites on helium ion treated molybdenum dichalcogenides under reaction conditions. *npj 2D Mater Appl* **2019**, *1*.

[204] A. Della Pia, G. Costantini, in *Encyclopedia of Nanotechnology* (Ed.: B. Bhushan), Springer Netherlands, Dordrecht **2016**, 3531.

[205] F. Schwabl, Quantum mechanics. (Quantenmechanik), *Springer XIII*, Berlin, Heidelberg **1991**.

[206] J. Bardeen, Tunnelling from a Many-Particle Point of View. *Phys. Rev. Lett.* **1961**, *2*, 57.

[207] J. Tersoff, D. R. Hamann, Theory and Application for the Scanning Tunneling Microscope. *Phys. Rev. Lett.* **1983**, *25*, 1998.

[208] M. Hugelmann, W. Schindler, Tunnel barrier height oscillations at the solid/liquid interface. *Surf. Sci.* **2003**, *1-3*, L643-L648.

[209] M. Hugelmann, W. Schindler, In Situ Distance Tunneling Spectroscopy at Au(111)/0.02 M $HClO_4$. *J. Electrochem. Soc.* **2004**, *3*, E97.

[210] G. Engelmann, J. Ziegler, D. Kolb, Electrochemical fabrication of large arrays of metal nanoclusters. *Surf. Sci.* **1998**, *2*, L420-L424.

[211] G. Binnig, N. Garcia, H. Rohrer, J. M. Soler, F. Flores, Electron-metal-surface interaction potential with vacuum tunneling: Observation of the image force. *Phys. Rev. B* **1984**, *8*, 4816.

[212] F. C. Simeone, D. M. Kolb, S. Venkatachalam, T. Jacob, The Au(111)/electrolyte interface: a tunnel-spectroscopic and DFT investigation. *Angew. Chem. Int. Ed.* **2007**, *46*, 8903.

[213] W. Schmickler, Tunneling of electrons through thin layers of water. *Surf. Sci.* **1995**, *335*, 416.

[214] F. C. Simeone, D. M. Kolb, S. Venkatachalam, T. Jacob, Tunneling behavior of electrified interfaces. *Surf. Sci.* **2008**, *7*, 1401.

[215] J. Pan, T. W. Jing, S. M. Lindsay, Tunneling Barriers in Electrochemical Scanning Tunneling Microscopy. *J. Phys. Chem.* **1994**, *16*, 4205.

[216] A. Vaught, T. W. Jing, S. M. Lindsay, Non-exponential tunneling in water near an electrode. *Chem. Phys. Lett.* **1995**, *3*, 306.

[217] C. F. A. Negre, G. E. Jara, D. M. A. Vera, A. B. Pierini, C. G. Sánchez, Detailed analysis of water structure in a solvent mediated electron tunneling mechanism. *J. Phys. Condens. Matter* **2011**, *24*, 245305.

[218] G. Nagy, T. Wandlowski, Double Layer Properties of Au(111)/H_2SO_4 (Cl) + Cu^{2+} from Distance Tunneling Spectroscopy. *Langmuir* **2003**, *24*, 10271.

[219] R. Hiesgen, D. Eberhardt, D. Meissner, Direct investigation of the electrochemical double layer using the STM. *Surf. Sci.* **2005**, *1-3*, 80.

[220] G. Binnig, H. Fuchs, E. Stoll, Surface diffusion of oxygen atoms individually observed by STM. *Surface Science Letters* **1986**, *2-3*, L295-L300.

[221] M. Sumetskii, A. A. Kornyshev, U. Stimming, Adatom diffusion characteristics from STM noise: theory. *Surf. Sci.* **1994**, *307-309*, 23.

[222] Dunphy, Sautet, Ogletree, Dabbousi, Salmeron, Scanning-tunneling-microscopy study of the surface diffusion of sulfur on Re(0001). *Phys. Rev. B* **1993**, *4*, 2320.

[223] T. Tiedje, J. Varon, H. Deckman, J. Stokes, Tip contamination effects in ambient pressure scanning tunneling microscopy imaging of graphite. *J. Vac. Sci. Technol. A* **1988**, *2*, 372.

[224] L. A. Kibler, Preparation and Characterization of Nobel Metal Single Crystal Electrode Surfaces. *International Society of Electrochemistry* **2003**.

[225] A. J. C. Wilson, A Handbook of Lattice Spacings and Structures of Metals and Alloys by W. B. Pearson. *Acta Cryst* **1959**, *2*, 81.

[226] R. M. Kluge, R. W. Haid, A. S. Bandarenka, Assessment of Active Areas for the Oxygen Evolution Reaction on an Amorphous Iridium Oxide Surface. *J. Catal.* **2021**, *396*, 14.

[227] L. D. Burke, D. P. Whelan, A voltammetric investigation of the charge storage reactions of hydrous iridium oxide layers. *J. Electroanal. Chem.* **1984**, *1-2*, 121.

[228] S. Ardizzone, A. Carugati, S. Trasatti, Properties of thermally prepared iridium dioxide electrodes. *J. Electroanal. Chem.* **1981**, *1-3*, 287.

[229] S. Geiger, O. Kasian, B. R. Shrestha, A. M. Mingers, K. J. J. Mayrhofer, S. Cherevko, Activity and Stability of Electrochemically and Thermally Treated Iridium for the Oxygen Evolution Reaction. *J. Electrochem. Soc.* **2016**, *11*, F3132-F3138.

[230] V. A. Saveleva, Li Wang, D. Teschner, T. Jones, A. S. Gago, K. A. Friedrich, S. Zafeiratos et al., Operando Evidence for a Universal Oxygen Evolution Mechanism on Thermal and Electrochemical Iridium Oxides. *J. Phys. Chem. Lett.* **2018**, *11*, 3154.

[231] V. I. Birss, C. Bock, H. Elzanowska, Hydrous Ir oxide films: the mechanism of the anodic prepeak reaction. *Can. J. Chem.* **1997**, *11*, 1687.

[232] A. Ganassin, V. Colic, J. Tymoczko, A. S. Bandarenka, W. Schuhmann, Non-covalent interactions in water electrolysis: influence on the activity of Pt(111) and iridium oxide catalysts in acidic media. *Phys. Chem. Chem. Phys.* **2015**, *13*, 8349.

[233] V. Pfeifer, T.E. Jones, J.J. Velasco Vélez, C. Massué, R. Arrigo, D. Teschner, F. Girgsdies, M. Scherzer, M.T. Greiner, J. Allan, M. Hashagen, G. Weinberg, S. Piccinin, M. Hävecker, A. Knop-Gericke, R. Schlögl, The electronic structure of iridium and its oxides. *Surf. Interface Anal.* **2016**, *48 (5).* 5, 261.

[234] H. Ogasawara, S. Kaya, A. Nilsson, Operando X-Ray Photoelectron Spectroscopy Studies of Aqueous Electrocatalytic Systems. *Top Catal* **2016**, *5-7*, 439.

[235] E. Özer, C. Spöri, T. Reier, P. Strasser, Iridium(1 1 1), Iridium(1 1 0), and Ruthenium(0 0 0 1) Single Crystals as Model Catalysts for the Oxygen Evolution Reaction: Insights into the Electrochemical Oxide Formation and Electrocatalytic Activity. *ChemCatChem* **2017**, *4*, 597.

[236] H. N. Nong, T. Reier, H.-S. Oh, M. Gliech, P. Paciok, T. H. T. Vu, D. Teschner et al., A unique oxygen ligand environment facilitates water oxidation in hole-doped IrNiOx core–shell electrocatalysts. *Nat Catal* **2018**, *11*, 841.

[237] K. A. Stoerzinger, L. Qiao, M. D. Biegalski, Y. Shao-Horn, Orientation-Dependent Oxygen Evolution Activities of Rutile IrO_2 and RuO_2. *J. Phys. Chem. Lett.* **2014**, *10*, 1636.

[238] U. Eberle, R. von Helmolt, Sustainable transportation based on electric vehicle concepts: a brief overview. *Energy Environ. Sci.* **2010**, *6*, 689.

[239] F. T. Wagner, B. Lakshmanan, M. F. Mathias, Electrochemistry and the Future of the Automobile. *J. Phys. Chem. Lett.* **2010**, *14*, 2204.

[240] A. Rabis, P. Rodriguez, T. J. Schmidt, Electrocatalysis for Polymer Electrolyte Fuel Cells: Recent Achievements and Future Challenges. *ACS Catal.* **2012**, *5*, 864.

[241] X. Wang, Z. Li, Y. Qu, T. Yuan, W. Wang, Y. Wu, Y. Li, Review of Metal Catalysts for Oxygen Reduction Reaction: From Nanoscale Engineering to Atomic Design. *Chem* **2019**, *6*, 1486.

[242] U. G. Vej-Hansen, J. Rossmeisl, I. E. L. Stephens, J. Schiøtz, Correlation between diffusion barriers and alloying energy in binary alloys. *Phys. Chem. Chem. Phys.* **2016**, *4*, 3302.

[243] B. Garlyyev, M. D. Pohl, V. Čolić, Y. Liang, F. K. Butt, A. Holleitner, A. S. Bandarenka, High oxygen reduction reaction activity of Pt_5Pr electrodes in acidic media. *Electrochem. Commun.* **2018**, *88*, 10.

[244] Y. Luo, A. Habrioux, L. Calvillo, G. Granozzi, N. Alonso-Vante, Thermally Induced Strains on the Catalytic Activity and Stability of Pt-M_2O_3/C (M=Y or Gd) Catalysts towards Oxygen Reduction Reaction. *ChemCatChem* **2015**, *10*, 1573.

[245] A. Velázquez-Palenzuela, F. Masini, A. F. Pedersen, M. Escudero-Escribano, D. Deiana, P. Malacrida, T. W. Hansen et al., The enhanced activity of mass-selected Pt Gd nanoparticles for oxygen electroreduction. *J. Catal.* **2015**, *328*, 297.

[246] E. Zamburlini, K. D. Jensen, I. E. Stephens, I. Chorkendorff, M. Escudero-Escribano, Benchmarking Pt and Pt-lanthanide sputtered thin films for oxygen electroreduction: fabrication and rotating disk electrode measurements. *Electrochim. Acta* **2017**, *247*, 708.

[247] R. Srivastava, P. Mani, P. Strasser, In situ voltammetric de-alloying of fuel cell catalyst electrode layer: A combined scanning electron microscope/electron probe micro-analysis study. *J. Power Sources* **2009**, *1*, 40.

[248] S. Chen, H. A. Gasteiger, K. Hayakawa, T. Tada, Y. Shao-Horn, Platinum-Alloy Cathode Catalyst Degradation in Proton Exchange Membrane Fuel Cells: Nanometer-Scale Compositional and Morphological Changes. *J. Electrochem. Soc.* **2010**, *1*, A82.

[249] H. L. Xin, J. A. Mundy, Z. Liu, R. Cabezas, R. Hovden, L. F. Kourkoutis, J. Zhang et al., Atomic-resolution spectroscopic imaging of ensembles of nanocatalyst particles across the life of a fuel cell. *Nano Lett.* **2012**, *1*, 490.

[250] S. J. Yoo, Y.-E. Sung, Nanosized Pt–La alloy electrocatalysts with high activity and stability for the oxygen reduction reaction. *Surf. Sci.* **2015**, *631*, 272.

[251] R. M. Kluge, E. Psaltis, R. W. Haid, S. Hou, T. O. Schmidt, O. Schneider, B. Garlyyev, A. S. Bandarenka, Revealing the Nature of Active Sites on Pt-Gd and Pt-Pr Alloys during the Oxygen Reduction Reaction, *in preparation*.

[252] Eleftherios Psaltis, In-Situ Identification of Active Electro-catalytic Sites for the Oxygen Reduction Reaction on Platinum Alloy Surfaces: Master Thesis (TUM) **2020**.

[253] K. D. Jensen, J. Tymoczko, J. Rossmeisl, A. S. Bandarenka, I. Chorkendorff, M. Escudero-Escribano, I. E. L. Stephens, Elucidation of the Oxygen Reduction Volcano in Alkaline Media using a Copper-Platinum(111) Alloy. *Angew. Chem. Int. Ed.* **2018**, *11*, 2800.

[254] V. Briega-Martos, E. Herrero, J. M. Feliu, Effect of pH and Water Structure on the Oxygen Reduction Reaction on platinum electrodes. *Electrochim. Acta* **2017**, *241*, 497.

[255] J. Staszak-Jirkovský, R. Subbaraman, D. Strmcnik, K. L. Harrison, C. E. Diesendruck, R. Assary, O. Frank et al., Water as a Promoter and Catalyst for Dioxygen Electrochemistry in Aqueous and Organic Media. *ACS Catal.* **2015**, *11*, 6600.

[256] B. S. Mun, M. Watanabe, M. ROSSI, V. R. Stamenkovic, N. M. Marković, P. N. Ross, The study of surface segregation, structure, and valence band density of states of Pt_3Ni(100), (110), and (111) crystals. *Surf. Rev. Lett.* **2006**, *05*, 697.

[257] R. M. Kluge, R. W. Haid, A. Riss, Y. Bao, K. Seufert, K. Eberle, J. V. Barth, F. Allegretti, W. Auwärter, F. Calle-Vallejo, A. S. Bandarenka, *In-Situ* Identification of Active Sites on Pt_3Ni(111) for the Electroreduction of Oxygen, *in preparation*.

[258] J. Zhang, H. Yang, J. Fang, S. Zou, Synthesis and oxygen reduction activity of shape-controlled Pt(3)Ni nanopolyhedra. *Nano Lett.* **2010**, *2*, 638.

[259] Q. Jia, Z. Zhao, L. Cao, J. Li, S. Ghoshal, V. Davies, E. Stavitski et al., Roles of Mo Surface Dopants in Enhancing the ORR Performance of Octahedral PtNi Nanoparticles. *Nano Lett.* **2018**, *2*, 798.

[260] J. Lim, H. Shin, M. Kim, H. Lee, K.-S. Lee, Y. Kwon, D. Song et al., Ga-Doped Pt-Ni Octahedral Nanoparticles as a Highly Active and Durable Electrocatalyst for Oxygen Reduction Reaction. *Nano Lett.* **2018**, *4*, 2450.

[261] V. Beermann, M. Gocyla, E. Willinger, S. Rudi, M. Heggen, R. E. Dunin-Borkowski, M.-G. Willinger et al., Rh-Doped Pt-Ni Octahedral Nanoparticles: Understanding the

Correlation between Elemental Distribution, Oxygen Reduction Reaction, and Shape Stability. *Nano Lett.* **2016**, *3*, 1719.

[262] T. Reier, M. Oezaslan, P. Strasser, Electrocatalytic Oxygen Evolution Reaction (OER) on Ru, Ir, and Pt Catalysts: A Comparative Study of Nanoparticles and Bulk Materials. *ACS Catal.* **2012**, *8*, 1765.

[263] J. Prakash, H. Joachin, Electrocatalytic activity of ruthenium for oxygen reduction in alkaline solution. *Electrochim. Acta* **2000**, *14*, 2289.

[264] D. A. C. Brownson, D. K. Kampouris, C. E. Banks, Graphene electrochemistry: fundamental concepts through to prominent applications. *Chem. Soc. Rev.* **2012**, *21*, 6944.

[265] A. Ambrosi, C. K. Chua, N. M. Latiff, A. H. Loo, C. H. an Wong, A. Y. S. Eng, A. Bonanni et al., Graphene and its electrochemistry - an update. *Chem. Soc. Rev.* **2016**, *9*, 2458.

[266] B. Garlyyev, S. Watzele, J. Fichtner, J. Michalička, A. Schökel, A. Senyshyn, A. Perego et al., Electrochemical top-down synthesis of C-supported Pt nano-particles with controllable shape and size: Mechanistic insights and application. *Nano Res.* **2020**.

[267] S. Sui, X. Wang, X. Zhou, Y. Su, S. Riffat, C. Liu, A comprehensive review of Pt electrocatalysts for the oxygen reduction reaction: Nanostructure, activity, mechanism and carbon support in PEM fuel cells. *J. Mater. Chem. A* **2017**, *5*, 1808.

[268] F. Lima, J. de Castro, L. Santos, E. A. Ticianelli, Electrocatalysis of oxygen reduction on carbon-supported Pt–Co nanoparticles with low Pt content. *J. Power Sources* **2009**, *2*, 293.

[269] M. Bernt, A. Siebel, H. A. Gasteiger, Analysis of Voltage Losses in PEM Water Electrolyzers with Low Platinum Group Metal Loadings. *J. Electrochem. Soc.* **2018**, *5*, F305-F314.

[270] J. Duan, S. Chen, M. Jaroniec, S. Z. Qiao, Heteroatom-Doped Graphene-Based Materials for Energy-Relevant Electrocatalytic Processes. *ACS Catal.* **2015**, *9*, 5207.

[271] Z. Sun, J. Masa, P. Weide, S. M. Fairclough, A. W. Robertson, P. Ebbinghaus, J. H. Warner et al., High-quality functionalized few-layer graphene: facile fabrication and doping with nitrogen as a metal-free catalyst for the oxygen reduction reaction. *J. Mater. Chem. A* **2015**, *30*, 15444.

[272] K. Qu, Y. Zheng, S. Dai, S. Z. Qiao, Graphene oxide-polydopamine derived N, S-codoped carbon nanosheets as superior bifunctional electrocatalysts for oxygen reduction and evolution. *Nano Energy* **2016**, *19*, 373.

[273] G.-L. Tian, M.-Q. Zhao, D. Yu, X.-Y. Kong, J.-Q. Huang, Q. Zhang, F. Wei, Nitrogen-doped graphene/carbon nanotube hybrids: in situ formation on bifunctional catalysts and their superior electrocatalytic activity for oxygen evolution/reduction reaction. *Small* **2014**, *11*, 2251.

[274] J. Maruyama, S. Maruyama, T. Fukuhara, H. Mizuhata, S. Takenaka, A. Yoshida, K. Miyazaki, Bifunctional Oxygen Electrodes with Highly Step-Enriched Surface of Fe–N_x Containing Carbonaceous Thin Film. *J. Electrochem. Soc.* **2020**, *6*, 60504.

[275] Y. Jia, L. Zhang, A. Du, G. Gao, J. Chen, X. Yan, C. L. Brown et al., Defect Graphene as a Trifunctional Catalyst for Electrochemical Reactions. *Adv. Mater.* **2016**, *43*, 9532.

[276] J.-C. Li, P.-X. Hou, S.-Y. Zhao, C. Liu, D.-M. Tang, M. Cheng, F. Zhang et al., A 3D bi-functional porous N-doped carbon microtube sponge electrocatalyst for oxygen reduction and oxygen evolution reactions. *Energy Environ. Sci.* **2016**, *10*, 3079.

[277] R. W. Haid, R. M. Kluge, T. O. Schmidt, A. S. Bandarenka, In-situ Detection of Active Sites for Carbon-Based Bifunctional Oxygen Reduction and Evolution Catalysis. *Electrochim. Acta* **2021**, *382*, 138285.

[278] S. Trasatti, Electrocatalysis in the anodic evolution of oxygen and chlorine. *Electrochim. Acta* **1984**, *11*, 1503.

[279] C. Spöri, J. T. H. Kwan, A. Bonakdarpour, D. P. Wilkinson, P. Strasser, The Stability Challenges of Oxygen Evolving Catalysts: Towards a Common Fundamental Understanding and Mitigation of Catalyst Degradation. *Angew. Chem. Int. Ed.* **2017**, *22*, 5994.

[280] C. C. L. McCrory, S. Jung, J. C. Peters, T. F. Jaramillo, Benchmarking heterogeneous electrocatalysts for the oxygen evolution reaction. *J. Am. Chem. Soc.* **2013**, *45*, 16977.

[281] A. Izgorodin, O. Winther-Jensen, D. R. MacFarlane, On the Stability of Water Oxidation Catalysts: Challenges and Prospects. *Aust. J. Chem.* **2012**, *6*, 638.

[282] A. Shen, Y. Zou, Q. Wang, R. A. W. Dryfe, X. Huang, S. Dou, L. Dai et al., Oxygen Reduction Reaction in a Droplet on Graphite: Direct Evidence that the Edge Is More Active than the Basal Plane. *Angew. Chem. Int. Ed.* **2014**, *40*, 10980.

[283] C. Tang, Q. Zhang, Nanocarbon for Oxygen Reduction Electrocatalysis: Dopants, Edges, and Defects. *Adv. Mater.* **2017**, *13*, 1604103.

[284] L. Zhang, Q. Xu, J. Niu, Z. Xia, Role of lattice defects in catalytic activities of graphene clusters for fuel cells. *Phys. Chem. Chem. Phys.* **2015**, *26*, 16733.

[285] Li Tao, Q. Wang, S. Dou, Z. Ma, J. Huo, S. Wang, L. Dai, Edge-rich and dopant-free graphene as a highly efficient metal-free electrocatalyst for the oxygen reduction reaction. *Chem. Commun.* **2016**, *13*, 2764.

[286] Y. Jiang, L. Yang, T. Sun, J. Zhao, Z. Lyu, O. Zhuo, X. Wang et al., Significant Contribution of Intrinsic Carbon Defects to Oxygen Reduction Activity. *ACS Catal.* **2015**, *11*, 6707.

[287] Z. Yang, Z. Yao, G. Li, G. Fang, H. Nie, Z. Liu, X. Zhou et al., Sulfur-doped graphene as an efficient metal-free cathode catalyst for oxygen reduction. *ACS nano* **2012**, *1*, 205.

[288] Y. Lin, Q. Lu, F. Song, L. Yu, A. K. Mechler, R. Schlögl, S. Heumann, Oxygen Evolution Reaction at Carbon Edge Sites: Investigation of Activity Evolution and Structure-

Function Relationships with Polycyclic Aromatic Hydrocarbons. *Angew. Chem. Int. Ed.* **2019**, *26*, 8917.

[289] W. Yu, M. D. Porosoff, J. G. Chen, Review of Pt-based bimetallic catalysis: from model surfaces to supported catalysts. *Chem. Rev.* **2012**, *11*, 5780.

[290] K. Sasaki, H. Naohara, Y. Choi, Y. Cai, W.-F. Chen, P. Liu, R. R. Adzic, Highly stable Pt monolayer on PdAu nanoparticle electrocatalysts for the oxygen reduction reaction. *Nat. Comm.* **2012**, *3*, 1115.